Mechanisms of Microwave Loss Tangent in High Performance Dielectric Materials

by

Lingtao Liu

A Dissertation Presented in Partial Fulfillment
of the Requirements for the Degree
Doctor of Philosophy

Approved December 2012 by the
Graduate Supervisory Committee:

Nathan Newman, Chair
Robert Marzke
Ralph Chamberlin

ARIZONA STATE UNIVERSITY

May 2013

ABSTRACT

The mechanism of loss in high performance microwave dielectrics with complex perovskite structure, including $Ba(Zn_{1/3}Ta_{2/3})O_3$, $Ba(Cd_{1/3}Ta_{2/3})O_3$, $ZrTiO_4$–$ZnNb_2O_6$, $Ba(Zn_{1/3}Nb_{2/3})O_3$, and $BaTi_4O_9$-$BaZn_2Ti_4O_{11}$, has been investigated. We studied materials synthesized in our own lab and from commercial vendors. Then the measured loss tangent was correlated to the optical, structural, and electrical properties of the material.

To accurately and quantitatively determine the microwave loss and Electron Paramagnetic Resonance (EPR) spectra as a function of temperature and magnetic field, we developed parallel plate resonator (PPR) and dielectric resonator (DR) techniques. Our studies found a marked increase in the loss at low temperatures is found in materials containing transition metal with unpaired d-electrons as a result of resonant spin excitations in isolated atoms (light doping) or exchange coupled clusters (moderate to high doping) ; a mechanism that differs from the usual suspects. The loss tangent can be drastically reduced by applying static magnetic fields. Our measurements also show that this mechanism significantly contributes to room temperature loss, but does not dominate.

In order to study the electronic structure of these materials, we grew single crystal thin film dielectrics for spectroscopic studies, including angular resolved photoemission spectroscopy (ARPES) experiment. We have synthesized stoichiometric $Ba(Cd_{1/3}Ta_{2/3})O_3$ [BCT] (100) dielectric thin films on MgO (100) substrates using Pulsed Laser Deposition. Over 99% of the BCT film was found to be epitaxial when grown with an elevated substrate temperature of 635 °C, an

enhanced oxygen pressures of 53 Pa and a Cd-enriched BCT target with a 1 mol BCT: 1.5 mol CdO composition. Analysis of ultra violet optical absorption results indicate that BCT has a bandgap of 4.9 eV.

DEDICATION

Dedicated to My Wife, Wei Shi and My Parents

ACKNOWLEDGMENTS

First and foremost I would like to express my indebtedness and gratitude to Professor Nathan Newman for his valuable guidance and encouragement throughout my Ph.D research. It has been my good fortune to be associated with such an excellent advisor during my study at Arizona State University. I would also like to thank Dr. Marco Flores in the chemistry department and Mr. David Cronin for their very valuable guidance and advice through the course of my research work. Mr. Cronin's assistance in helping me learn how to produce high quality material was extremely valuable. Dr. Flores's assistance with the experiments using the conventional Bruker EPR experiment was extremely important to this work and played a crucial part in identifying the loss mechanism at 4.2 K. I would also like to thank Professors Robert Marzke and Ralph Chamberlin for helping me as my dissertation committee. I am thankful for their valuable.

I feel grateful for all current and former students who belong to the Professor Newman Research Group: Dr. Rakesh Singh, Dr. Zhizhong Tang, Dr. Lei Yu, Dr. Subhasish Bandyopadhyay, Dr. Yi Shen, Dr. Brett Strawbridge, Mr. Lei Zhang, Mr. Mengchu Huang, Mr. Cameron Kopas, Ms Tiantian Zhang, Mr. You Li, Ms Alena Matusevich, Mr. Makram Abd El Qader, Mr. Mahmoud Vahidi, Mr. Shenke Zhang, and Mr. Dexuan Wang. Thanks to you all for creating a compassionate and friendly atmosphere around me. Dr. Bandyopadhyay helped to measure the temperature dependent I-V curves for commercial ceramic samples. I

would also like to thank Mr. Richard Hanley for his valuable advice and great support in developing and repairing electronic systems.

I acknowledge the help of the use of facility in Center of Solid State Science (CSSS) at ASU. I will especially thank Mr. David Wright for his great technical support when I used their equipment. I would also like to thank Dr. Craig Birtcher for his help in constructing the RF coax cable and connectors for our experiment.

Last but not least, I would like to thank my family for their continuous support during my studies. I am indebted to my wonderful wife, Wei Shi. She supports me for my everyday life very thoughtfully. We share not only happy time, but also hard time together. Thank my parents who also support me in my faraway home country.

TABLE OF CONTENTS

Page

CHAPTER Page

LIST OF TABLES

LIST OF FIGURES

Figure Page

Figure Page

Chapter 1

MOTIVATION AND BACKGROUND

1.1 Research background

Microwave dielectric materials are widely used in cellar communication base stations and hand set devices [1]. Within a base station, the signal received from the antenna tower is processed using microwave filters. Dielectric resonators are often used in these filters.

High quality materials are needed to build microwave devices with smaller sizes, temperature stability, and higher frequency selectivity. There are three main material properties involved in the material selection for these devices: dielectric constant (ε_r), temperature coefficient of resonant frequency (τ_f), and loss tangent (tan δ). High dielectric constant enable size reductions. The device size L is inversely proportional to square root of dielectric constant, $L \propto (\varepsilon_r)^{-1/2}$. Increasing the permittivity is typically achieved by the substitution of a cation with large ionic polarizability or one which results in a smaller unit cell volume. Low loss helps to use radio spectrum resources more efficiently, reduce the signal interference, and maximize the frequency selectivity for filters. Near zero τ_f gives temperature-stabilized resonant frequency and band position.

The history of microwave dielectric materials is shown in fig.1.1 as a roadmap [1]. In the early days, the metal cavities were predominantly used for resonators in filters and hand sets, but they were large in size. From 1970s, the first generation

of dielectric resonators based on $(Mg,Ca)TiO_3$, $ZrTiO_4$, and $BaTi_4O_9$ were introduced and replace the metal cavity resonators [1].

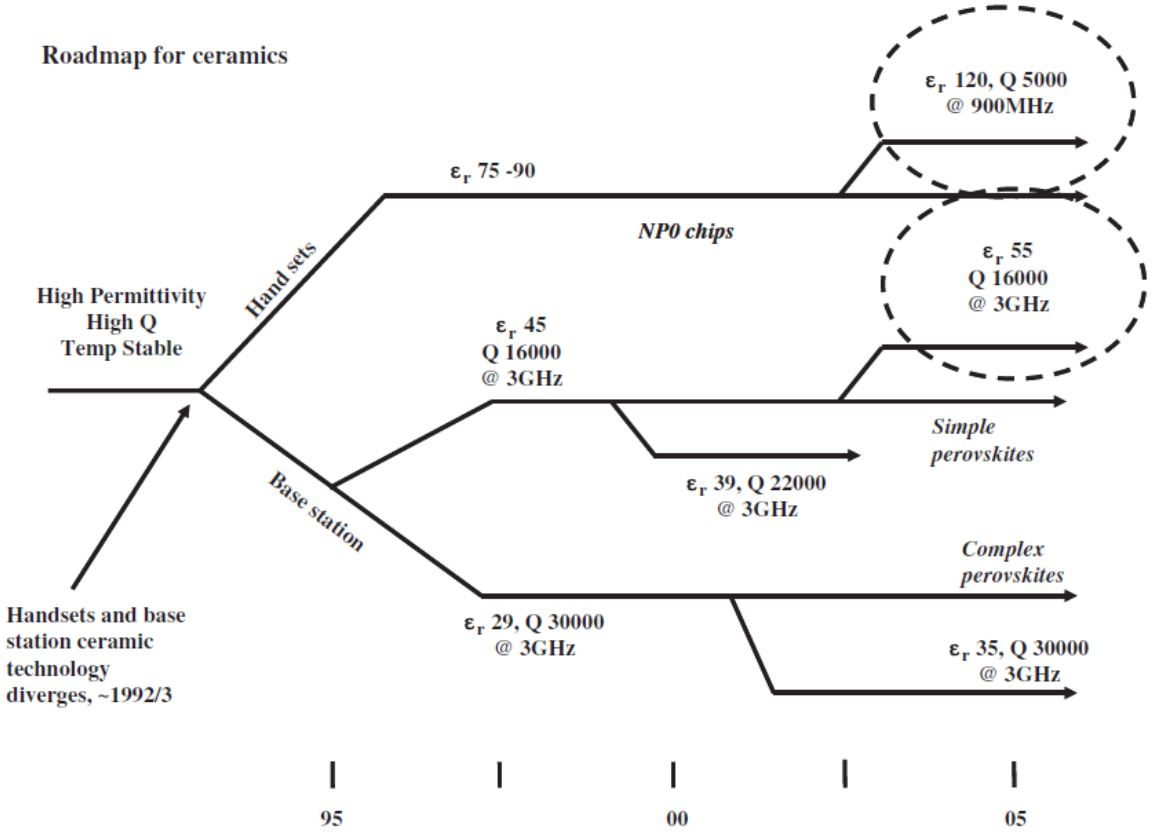

Figure 1.1 Roadmap for the microwave dielectric materials [1]

Table 1.1 lists the current commercial materials in this areas. Among them, materials with complex perovskite structure $A(B'_{1/3}B''_{2/3})O_3$ (A = Ba^{2+}, B' = Mg^{2+}, Zn^{2+}, Ni^{2+} or Cd^{2+} and B'' = Ta^{5+} or Nb^{5+}) have attractive microwave properties, high permittivity (~30), low dielectric loss (<2 x 10^{-5} scaled to 2GHz) and almost near zero temperature coefficient of resonance frequency. Among these compound, $Ba(B'_{1/3}Ta_{2/3})O_3$, where B' = Zn or Mg exhibit the highest Q values. Usually there are two kinds of crystal structure for them, ordered

hexagonal structure and disordered pseudocubic structure (Fig.1.2). The BZT hexagonal structure has a Zn^{2+} - Ta^{5+} - Ta^{5+} repeat planes sequence along the < 111 > direction of the parent cubic perovskite cell.

Table 1.1 Current commercial microwave dielectric materials with near zero temperature coefficient [1]

Material	Abbreviation	ε_r	$Q \times f_0$ (GHz)	Structure
$BaMg_{1/3}Ta_{2/3}O_3$	(BMT)	24	250 000	Comp. Per.
$BaZn_{1/3}Ta_{2/3}O_3$	(BZT)	29	150 000	Comp. Per.
$Ba(Co,Zn)_{1/3}Nb_{2/3}O_3$	(BCZN)	34	90 000	Comp. Per.
$SrTiO_3$–$LaAlO_3$	(STLA)	39	60 000	Simp. Per
$CaTiO_3$–$NdAlO_3$	(CTNA)	45	48 000	Simp. Per
$ZrTiO_4$–$ZnNb_2O_6$	(ZTZN)	44	48 000	α pbO_2
$Ba_4Nd_{9.333}Tu_{18}O_{54}$	(BNT)	80	10 000	Per/TTB

Comp., complex; Per, perovskite; Simp., simple; TTB, tetragonal tungsten bronze; MW, microwave.

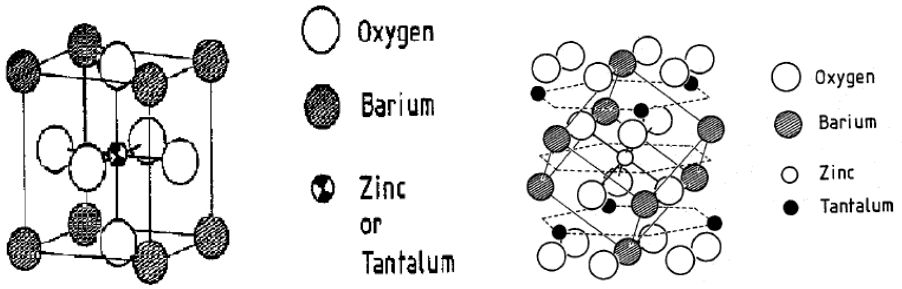

Figure 1.2 Ordered and disordered structures of BZT lattices. [2]

1.2 Thesis organization

This thesis contains six chapters. In chapter 1, the research background for microwave dielectric ceramics is briefly reviewed.

In chapter 2, the methods of synthesis of microwave dielectric materials are described. The conventional powder processing technique was used to make microwave dielectric ceramics. Pulsed Laser Deposition (PLD) was used to make high quality epitaxial dielectric thin films. An example of $Ba(Cd_{1/3}Ta_{2/3})O_3$ (BCT) epitaxial thin film growth is demonstrated. BCT thin films were deposited on MgO (100) substrates. The use of enhanced oxygen pressures (400 mT), Cd-enriched targets (1:1.5 mol BCT:CdO) and elevated substrate temperatures (635 °C) were needed to attain these results. The RMS roughness of the surface is 4.8 nm and the mean grain size is 110 nm, as determined by atomic force microscopy (AFM). A room temperature dielectric constant of 32 was determined using capacitance measurements of a planar inter-digital metallic pattern at frequencies up to 500 kHz. A refractive index of 2.1 was inferred from optical transmission measurements in the visible range. A bandgap of 4.9 eV has been determined using optical absorption experiments. Temperature-dependent electrical measurements have determined a room temperature conductivity of $3x10^{-12}$ $(\Omega\text{-cm})^{-1}$ with a thermal activation energy of 0.7 eV.

In chapter 3, we introduce the measurement techniques for accurately measuring microwave loss. We designed a new method which can be used in conjunction with a microwave dipping probe or a commercial cryostat to quantitatively measure the loss tangent of small samples as a function of

temperature and magnetic field. It is a unique technique which allowed us to investigate the mechanism of microwave loss at cryogenic temperatures in small dielectric samples.

Using the methods discussed above, in chapter 4, we investigate the mechanism of microwave loss at cryogenic temperatures for the high performance microwave dielectric $Ba(Zn_{1/3}Ta_{2/3})O_3$ containing commonly-used dopants. We quantitatively measured the loss tangent of BZT as a function of temperature and magnetic field. This, combined with conventional and pulsed EPR measurements, shows conclusively that the dominant loss process results from non-resonant spin excitations of exchange coupled clusters of unpaired transition metal d-electrons. We also study other commonly used commercial materials including $ZrTiO_4$–$ZnNb_2O_6$, $Ba(Zn_{1/3}Nb_{2/3})O_3$, and $BaTi_4O_9$-$BaZn_2Ti_4O_{11}$ ceramics produced in a commercial product line. The same mechanism was found to apply for all of the materials. The loss tangent can be drastically reduced by applying static magnetic fields at cryogenic temperature. Our measurements also show that this mechanism significantly contributes to room temperature loss, but does not dominate.

In chapter 5, we study the dominant mechanism(s) of microwave loss at room temperature. The presence of point defects are found to significantly influence the loss. We then made electrical, Far-Infrared and Raman characterizations to try to correlate the loss with nature and concentration of the defects.

In chapter 6, a brief summary of the thesis work was given and a recommendation for future work is provided.

Chapter 2

MICROWAVE DIELECTRIC MATERIAL SYNTHESIS

2.1 Ceramic synthesis method and results

The ceramics were produced using traditional powder processing technique. Firstly, the reagent-grade (>99.99%) powder of Ta_2O_5, $BaCO_3$, ZnO, NiO or other powder were weighed and mixed according to the mass ratio. Then, the powder was put into a high density Polyethylene baffled (HDPE) jar (Cole-Parmer, Vernon Hills, IL) with addition of the ZrO_2 grinding balls (1cm diameter). The mass ratio between grinding balls and powder is 4:1. Deionized (DI) water was then added with powder in a mass ratio of 1:1. Then, the jar was put in a ball mill machine with a rotation speed of 100 rpm and run for 8 hours. The slurry was dried and fired in a high temperature furnace (Model 1706 GS FL (c), CM furnaces company inc., Bloomfield, NJ) at 1300°C for 6 hours. After this, the powder was put into an Alumina grinding jar and ground for 4 additional hours. During this process, the mass ratio of milling balls to powder and water to powder are still 4:1 and 1:1, respectively. 0.5 wt% of Ammonium Polyacrylate dispersant (Darvan 821A, R.T. Vanderbilt Company, Inc.) was added to keep the slurry with a high solid content and the ground powder closely packed and very fine (mean grain size is about 1 μm). For making Ni doped BZT samples, BNT and BZT powder were mixed according to the desired mass ratio. They were then put into an HDPE jar and ball milled for 0.5 hour. The mixed powder was dried and added with 5 wt% of Poly vinyl alcohol (PVA) / Polyethylene glycol (PEG) binder (85

wt% DI water, 9 wt% PVA and 6 wt% PEG) and dried again. Then it was pressed into pellet and sintered in high temperature furnace in air (CM furnaces) from 1400°C to 1600°C, depending on the type of material being processed, for a couple of hours.

The ceramic samples were then machined to remove lower quality and possibly multi-phase material near the surface, then cleaned and dried. The relative density was then measured using the pycnometry method. All of the samples made with these methods achieved larger than 95% relative density. The microwave loss and structural measurements were then performed on these samples. The following table shows the results of microwave measurements using conventional TE01δ cavity method. [3]

Table 2.1 Microwave measurement of synthesized BZT ceramics samples. f_0 denotes the resonant frequency and Q_0 is the unloaded Q factor.

Sample	f_0 (GHz)	Q_0	Q_0 scaled to 2GHz
012411 Undoped BZT	2.675	11179	14952
040911_1 Ga1%BZT	2.640	18029	23798
040911_2 Sn1%BZT	2.644	9646	12752
042011 3%Ni BZT	2.624	14949	19613
042211_1 Undoped	2.631	15763	20736
042211_2 5%Ni doped	2.667	21807	29080
042211_3 1% Nidoped	2.620	18701	24498

050911 12%BNT 88%BZT	2.706	15437	20886
051811_1 0.5% Mn BZT	2.564	13965	17903
051811_2 2% Mn BZT	2.561	7773	9950
051811_3 4% Mn BZT	2.511	3756	4716
052711_1 0.25% Mn BZT	2.794	9931	13874
042711 5%BCT-95%BZT	2.514	25884	32536
042911_2 5%BMT-95%BZT	2.543	14419	18334
052711_2 1% Mn BZT	2.577	5531	7127
062411 Undope BZT	2.508	19248	24137
072211 5%Zr doping	2.552	34224	43670
101311 8%Ni doped	2.625	24332	31936
121111 BNiT	2.747	9029	12401
011212_1_10%Zr_BZT	2.558	25372	33090
011212_2 10%BCT_BZT	2.578	2847	3670
030812 1% Co BZT	2.724	16092	21917
041412_1 40% BNT BZT	2.828	14883	21045
041412_1 60% BNT BZT	2.837	9783	13877
041412_1 80% BNT BZT	2.947	7756	11430
102212 BZT	2.8362	18102	25670

The structural properties are characterized by X-ray diffraction (XRD) and Scanning electron microscopy (SEM). Fig.2.1 show the 2θ coupled scan of Ni doped BZT ceramic samples. It shows a single phase BZT BNT miscible solid solution. No secondary phases were observed in the XRD data.

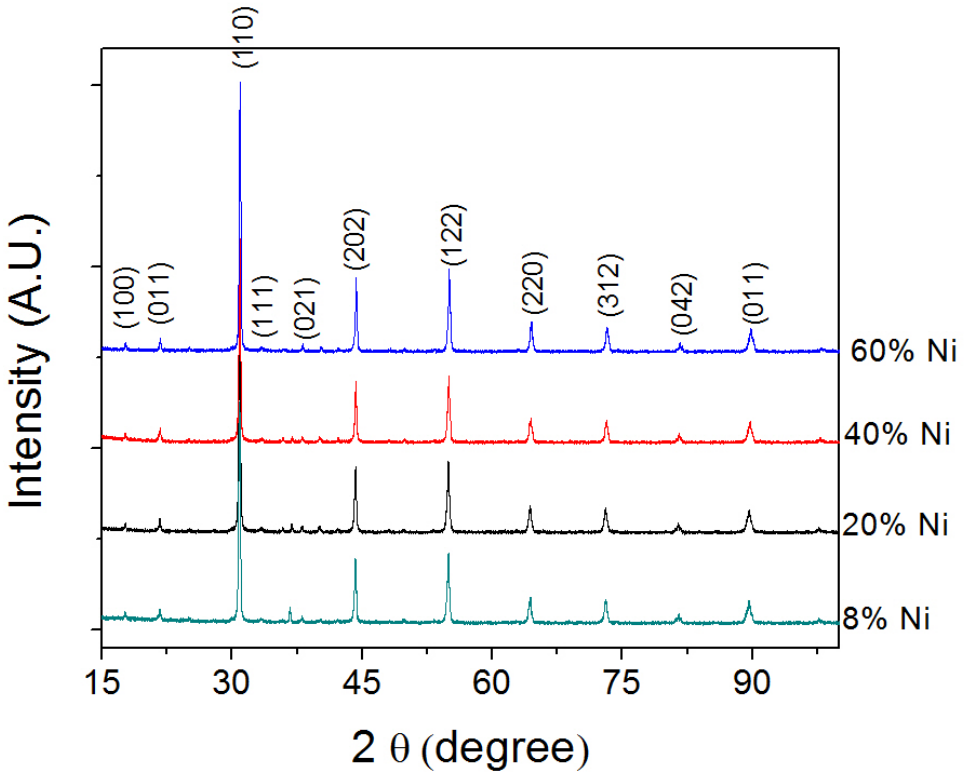

Figure 2.1 XRD 2θ scan of Ni doped BZT ceramic samples with Ni doping from 8 mol% to 60 mol%.

SEM data were taken with FEI XL30 SEM system. The images were scanned using secondary electron mode with electron energy of 20keV. The images shown below illustrate the surface morphology and grain shape of the ceramics. Zr doped BZT show an average grain size of 5 to 10 μm which is bigger than those of Ni

doped or undoped BZT of 2 to 5 μm. These pictures indicate that Zr doping may be responsible for improving grain growth, resulting in a more uniform grain size distribution.

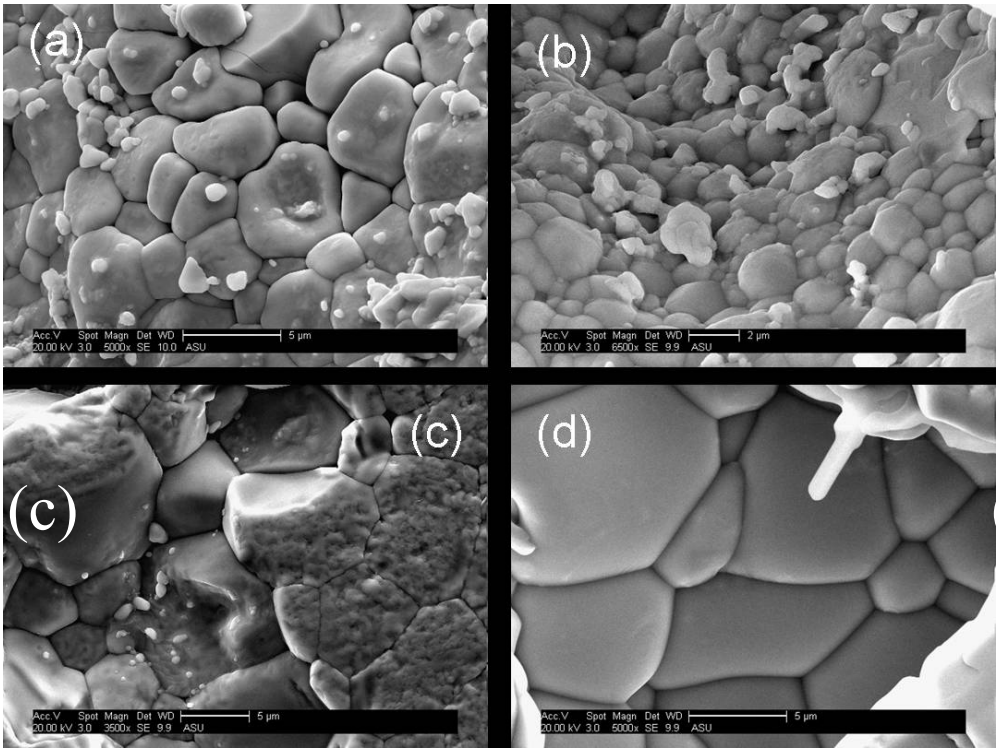

Figure 2.2 SEM image of sintered BZT ceramics. (a) Undoped BZT; (b) 8% Ni doped BZT; (c) 5% Zr doped BZT and (d) commercial BZT doped with Ni and Zr atoms (D8733 from Trans Tech inc.).

2.2 Microwave dielectric thin film growth method and results (focus on epitaxial $Ba(Cd_{1/3}Ta_{2/3})O_3$ thin films)

Perovskite $Ba(B'_{1/3}B''_{2/3})O_3$ dielectrics (where B' = Mg, Zn Cd, with valence II and B'' = Ta, Nb with valence V) are routinely used in high-Q resonators and filters for wireless communications [4,5]. $Ba(Zn_{1/3}Ta_{2/3})O_3$ (BZT) is one of the most important members in this group, because of its relatively high dielectric constant (ε_r =30), ultra-low loss tangent (tan $\delta<2\times10^{-5}$ at 2 GHz) and ability to achieve near-zero temperature coefficient of resonant frequency (τ_f=0) with Ni-doping [6]. Recent theoretical calculations indicate that the covalent nature of the directional d-electron bonding in the $Ba(B'_{1/3}B''_{2/3})O_3$ oxides, a property absent in classical ionic compounds, plays an important role in producing a more rigid lattice and strengthening the soft anharmonic lattice modes [7]. This could potentially be the most important factor responsible for the low intrinsic microwave loss exhibited by these high dielectric constant $Ba(B'_{1/3}B''_{2/3})O_3$ material systems.

$Ba(Cd_{1/3}Ta_{2/3})O_3$ (BCT) is another compound in this perovskite family and its electronic structure has some similarities to that of BZT [7,8]. For example, both BZT and BCT have a conduction band maximum (CBM) that is comprised of almost entirely Ta-5d character.[7] However, analysis of BCT properties suggests that this compound could potentially exhibit lower loss than BZT due to its enhanced degree of d-electron bonding [7] and higher tendency for cation ordering [9,10]. The greater extent of d-electron bonding in BCT results from the valence band maximum (VBM) being almost exclusively Cd-4d character, while BZT's is an admixture of Zn-3d and O-2p levels. The tendency for cation

ordering in BCT results from the disparity in the ionic size of Cd to Ta, when compared to that of Zn to Ta.

The exceptional microwave properties, as well as the chemical compatibility and similar lattice constant with some oxides such as MgO (4.21 Å), and other commonly used perovskites, including $YBa_2Cu_3O_{7-\delta}$ (YBCO) (a 3.82, b 3.89 Å [11]), $LaAlO_3$ (3.81 Å) and $SrTiO_3$ (3.90 Å), make BZT (4.09 Å [12]) and BCT (4.17 Å) appealing candidates for integration into oxide thin-film microelectronic devices. Thus, it is desirable to develop methods to produce high-quality thin films and to have their physical properties characterized.

Our previous paper reported the growth of epitaxial and stoichiometric BZT (100) films on MgO (100) substrates and the results of structural, chemical, optical and electrical characterization [12]. There has also been some more recent work reporting on the growth and properties of BZT thin films [14]. To date, there have not been any reported studies of the synthesis of BCT epitaxial thin films.

A challenge in growing BCT and BZT films is to simultaneously be able to use the high substrate temperatures (typically 600°C to 700°C) needed to overcome the kinetic barriers required to achieve epitaxy and still attain stoichiometric compounds [15,16,17]. This challenge results from factors including the high volatility of elemental Cd and Zn, the limited sticking coefficient of the Cd and Zn elements on the growth surface, and the thermal decomposition of BCT and BZT.

The use of relatively high oxygen pressure and enhanced Zn elements in the target (Zn-enriched targets) are found to be critical to obtaining high-quality and

epitaxial BZT thin films [12]. Firstly, the use of Zn-enriched targets can help to compensate the loss of the volatile elements during the thin film deposition. Secondly, the relatively high oxygen pressure of 27 Pa enhances the fraction of Zn-O bonded chemical components on the growth that are much less volatile.[12] These conditions can also reduce re-sputtering at the growth surface by reducing the kinetic energy of the plasma plume.[12]

For BCT growth, the problems associated with achieving stoichiometric films at elevated temperatures is even more serious than that in BZT because Cd is more volatile than Zn. Nevertheless, in this manuscript we show that the same approach used for BZT is also applicable for growth of BCT epitaxial films. In this manuscript, we develop methods to optimize the growth of highly-oriented and stoichiometric BCT films on MgO(100) substrates using enhanced oxygen pressures, Cd-enriched targets and elevated substrate temperatures. The results of optical, structural, electrical and dielectric characterization are also described.

2.2.1 Introduction to Pulsed Laser deposition

The Pulsed Laser Deposition (PLD) system is used in this study to grow dielectric thin film material. PLD is a thin film deposition technology that uses a high power density pulsed laser beam focused on a target. The target material is firstly ablated by the laser into a plasma, which is transported and deposited on the substrate. PLD is a kind of Physical Vapor Deposition technique. The equipment system include ultra high vacuum chamber, vacuum pumps and ultra violet (UV) gas laser source. It's working in a gas atmosphere like Argon, Neon or

Oxygen. The process of PLD growth contains four steps. First, the pulsed laser ablate the target material and create the plasma. Then, the plasma plume transport species between target and substrates. Thirdly, the material incorporate onto the substrate and last it nucleates and grows on the substrate surface. The PLD system in our lab is shown in Fig.2.3.

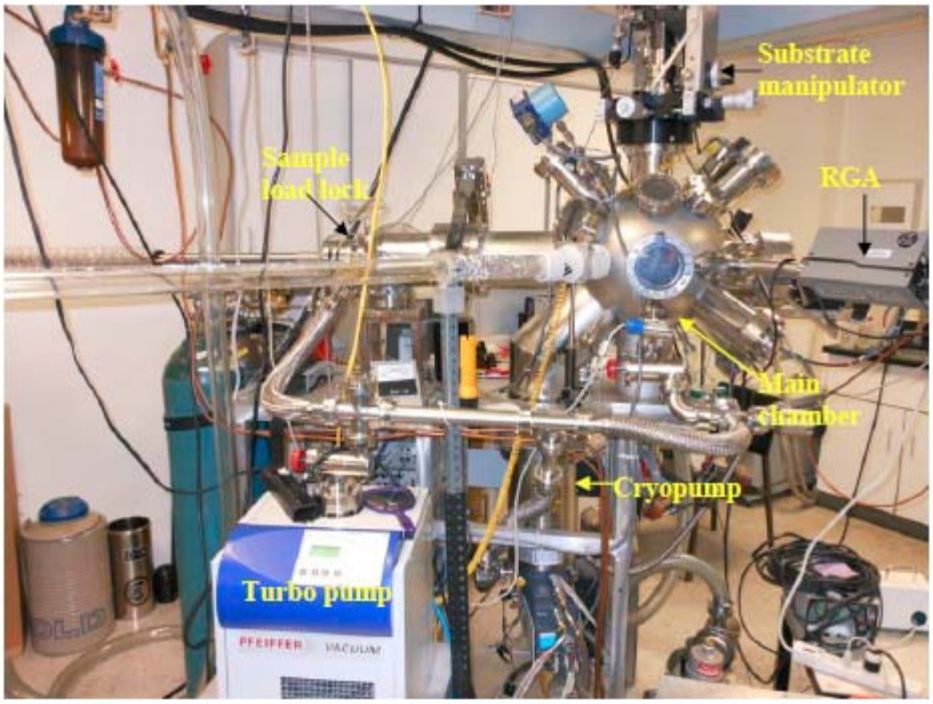

Figure 2.3 Pulsed Laser Deposition system in our lab.

2.2.2 Experimental method

An ultra-high vacuum pulsed laser deposition (PLD) system has been used to deposit $Ba(Cd_{1/3}Ta_{2/3})O_3$ thin films on single crystal 1 cm^2 MgO (100) substrates (MTI Inc., Richmond, CA). The PLD system is equipped with a KrF excimer

laser (Lambda Physik, λ= 248 nm) operated at an energy density of 5 Jcm^{-2} and a repetition rate of 2 Hz. The base pressure of the vacuum chamber is ~7 x 10^{-5} Pa. The substrate–target distance is ~5 cm. The growth rate typically was 7.5±2.5 nm per minute. To attain the highest accuracy for the Rutherford Backscattering Spectroscopy (RBS) stoichiometry determinations, films were produced with thicknesses between 50 and 100 nm. This results in separate, narrow Ba, Cd, and Ta peaks in the RBS spectra, so the data can be unambiguously and precisely fit. For all other measurements, film thicknesses in the range of 400±50 nm were used.

The preparation of a Cd-enriched BCT target is quite different from that of a Zn-enriched BZT target. A Zn enriched BZT target is prepared by a conventional solid state powder sintering process [12]. The ZnO and BZT powder are mixed according to the mass ratio, pressed into pellets and sintered at 1400 to 1600 °C. However, this method doesn't work for the Cd-enriched BCT target because CdO-containing powder begins to melt at temperatures of 900°C to 1000°C [18], which is significantly lower than that of ZnO powder (1974°C [19]). When molten material is present at the sinter temperature (1400°C to 1600°C), the target can deform and crack. Simply mixing BCT and CdO powder together and pressing doesn't work either because it results in a very low density target (50 to 60% relative density) which leads to very rough thin films whose top surfaces are decorated with numerous powder particles. Therefore, in this work, a different process was used for making Cd enriched BCT targets. In this method, the BCT and CdO powder were lightly sintered into hard and coarsened particles

separately and without pressing before being mixed. The BCT powder was fired at 1350°C for 2 hours and the CdO powder was fired at 880°C for 1 hour in a box furnace in air atmosphere. Then, these particles were ground using mortar and pestle, screened with 28-mesh, mixed uniformly according to the mass ratio needed, and pressed into targets. These targets have relatively high density (about 80%) and the films grown with them have a smooth surface. The addition of a small amount of B_2O_3 powder (0.15 wt% for BCT and 0.5 wt% for CdO) as a liquid sintering aid was found to be essential to bond and condense the fine loose powders.

The film's composition and thickness was determined by Rutherford backscattering spectroscopy (RBS) with a 3.05 MeV He+ incident beam. RBS analysis was performed using the RUMP software package (Rutherford Backscattering Spectroscopy Analysis Package, Genplot, Cortland,OH).

An X-ray diffractometer (XRD) (Rigaku D/MAX-IIB,Japan) with a high flux hybrid monochromator (4-crystal Ge(220)/(440)) and Cu–Kα radiation (λ=1.5405 Å) operated at 45 kV and 40 mA was used to characterize the structural properties of the thin-films. Note that BCT and BZT have both pseudo-cubic disordered cation lattices and hexagonal ordered cation lattices which results from a slight elongation in the direction of the (111) cube axis. Although the symmetry changes, the actual atomic displacements represent less than a 0.05% change in bond length[13]. For simplicity, we will use the BCT and BZT pseudo-cubic lattice parameters in this work.

The roughness and grain size was measured using an atomic force microscope (AFM) (Digital Instrument, Dimension 3000). The optical properties were characterized with a double channel spectrometer (Model DS200, Ocean Optics Inc., Dunedin, FL). The absorption coefficient was inferred from the measured absorbance and sample thickness. The electrical Current-Voltage (I-V) and Capacitance-Voltage (C-V) properties are measured in a planar interdigital pattern configuration using a picoammeter (QuadTech 1865 Megohmmeter/IR tester, Maynard, MD) and a capacitance meter (QuadTech 7400 Precision RLC meter). The interdigital pattern is shown is Fig.2.4. 40 fingers of 2mm long, 20 μm wide are patterned on the BCT thin films by metal lift-off. Negative photo resist AZ1512 was used for photo lithography. After UV light exposure, the films was developed in a solution about 1 minute. Thermal evaporation was utilized to deposit metal layer on top of the BCT thin films. Ti-Au bilayer was deposited. The Ti layer act as a sticking layer because the Au doesn't stick strongly directly on the BCT thin film, but stick well on top of Ti layer. The thickness of Ti layer was about 100 nm and that of Au layer was about 500 to 1000nm.

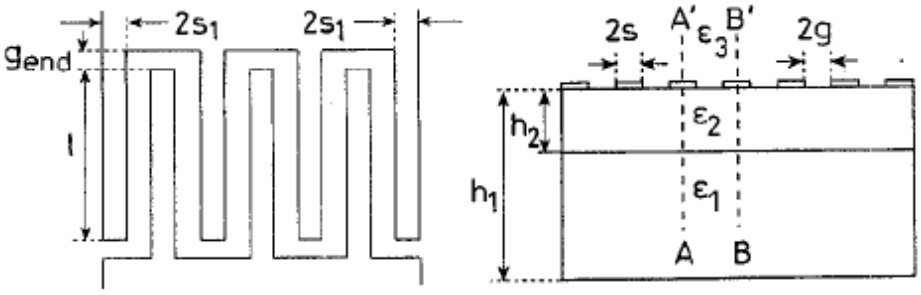

Figure 2.4. Interdigit pattern configuration on BCT thin films [29]

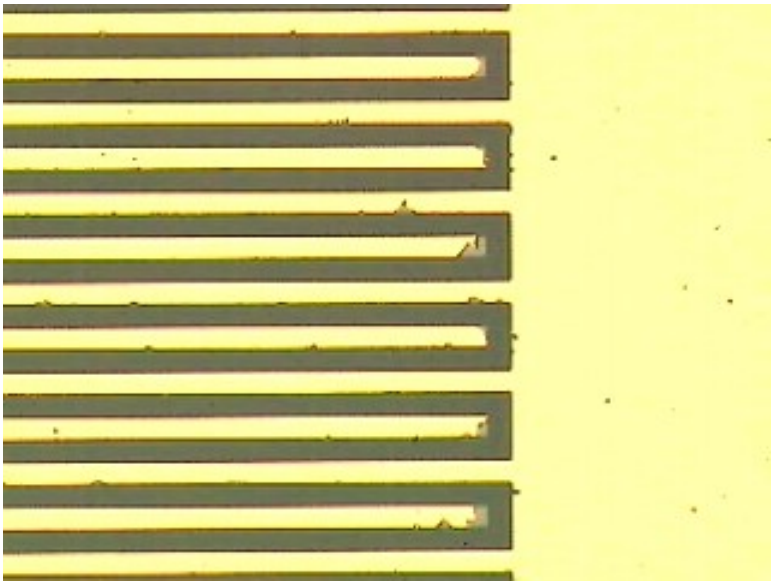

Figure 2.5 Au-Ti bi-layer by metal lift-off on BCT thin films

2.2.3 Experimental results and analysis

In stoichiometric BCT, the ratio of the Ta to Cd atoms (Ta:Cd) is 2, and that of Ta:Ba is $^{2}/_{3}$. Cd-enriched BCT targets with a 50% Cd-enriched target (i.e. 1 mol BCT: 0.5 mol CdO), 75% Cd-enriched target (i.e. 1 mol BCT: 0.75 mol CdO) and 150% Cd-enriched target (i.e. 1 mol BCT: 1.5 mol CdO) were used to deposit thin films at a series of growth temperatures. In all of these experiments, the Ta:Ba ratio is measured to be $^{2}/_{3}$, the same value as the target. This is as expected due to the non-volatile nature of elemental Ta and Ba and their oxides. The Ta:Cd ratio, as inferred from RBS analysis, systematically vary with target composition and substrate temperature. These results are summarized in Fig.2.6. The Ta:Zn ratio of BZT thin film [12] are also presented as hollowed star symbols in the figure.

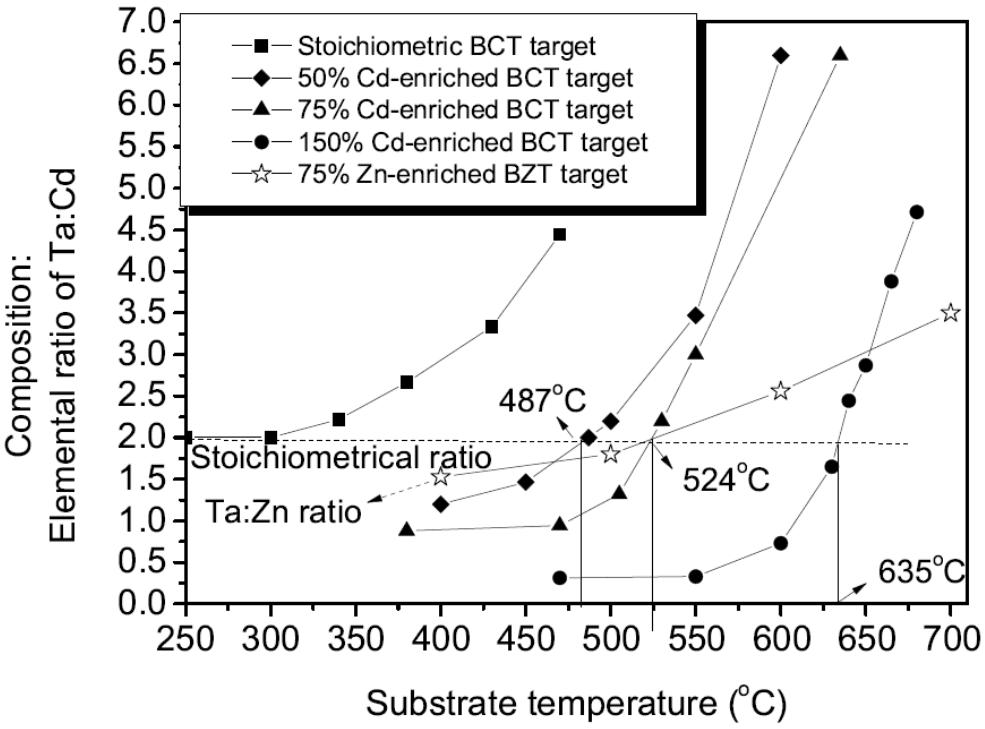

Figure 2.6. Ratios of elemental composition in as-grown films fabricated using BCT targets with varying levels of Cd enrichment. Film thicknesses used for this measurement ranged from 50-100 nm.

For the pure stocichiometric BCT target deposited at temperatures between 250°C and 475°C, the Ta:Cd curve is maintained at 2 until a substrate temperature of 300°C. Above this temperature, it dramatically increases due to Cd loss. A similar increase is found for growths with a 50% Cd-enriched target, although the highest temperature (T_m) at which Ta:Cd is ~2 shifts from 300°C to 487°C. When other more highly Cd-enriched targets are used, the T_m shifts to 524°C and finally 635°C. Similar trends were also found for Zn-enriched BZT targets, but T_m is

consistently lower and the loss with temperature is much more gradual as a result of the lower volatility of Zn than Cd.

In general, a high growth temperature is needed to overcome the kinetic barriers required to achieve epitaxial growth of oxide thin films. The results of XRD θ–2θ measurement are shown in Fig.2.7 for stoichiometric films grown with different targets. We grew 400±50 nm thick films for structural analysis. The measured spectra were aligned to the bulk substrate MgO (200) peaks in order to compensate for small misalignments between the sample and the XRD stage.

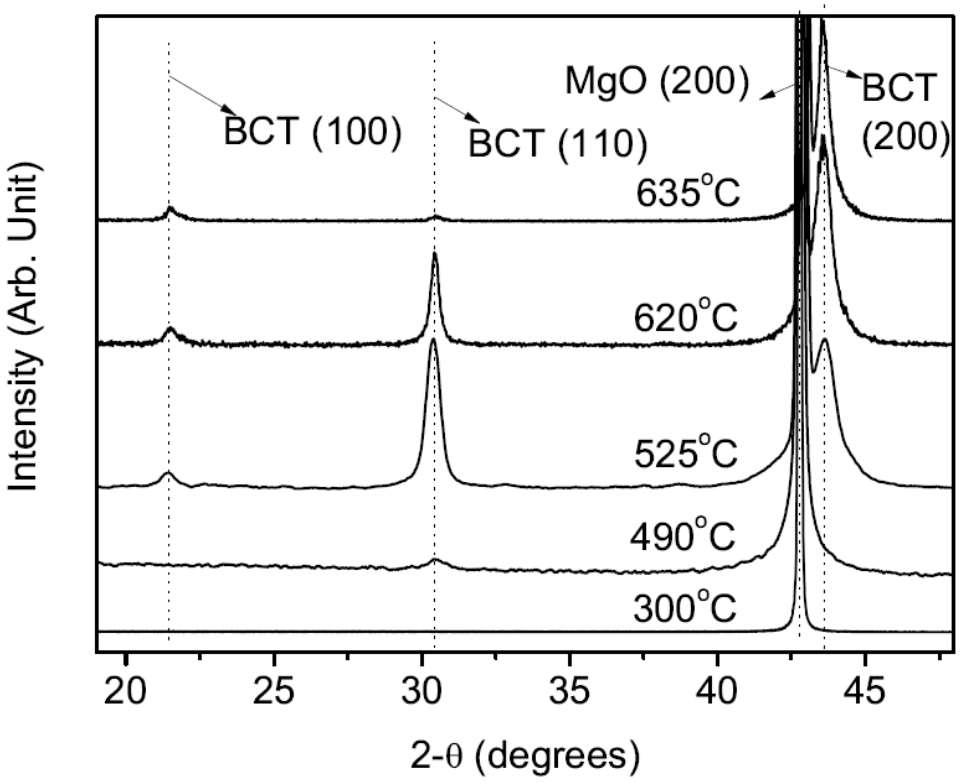

Figure 2.7 XRD θ –2θ coupled scan of stoichiometric BCT thin films grown at different substrate temperatures (A linear scale is used for intensity). Film thicknesses are measured by RBS to be in the range of 400±50 nm.

The absence of a crystalline peak in the X-ray diffraction data for the film grown at 300°C with a stoichiometric target suggests that the film is amorphous. A small crystalline BCT (110) peak is observed in the film grown at 490°C with the 50% Cd-enriched target. XRD data for the 525°C film grown with the 75% Cd-enriched target exhibits a large BCT (110) peaks, a smaller (200) Bragg reflection peak and a much smaller (100) peak- representing clear evidence for the presence of crystallinity. This is similar to the pattern found for polycrystalline BCT bulk ceramics. For growths at higher substrate temperatures, the intensity of the Bragg BCT (110) peak decreases relative to that of (100) and (200) peaks. This indicates the formation of a texturing of the film with a preferential (100) orientation. For the film grown at 620°C with the 150% Cd-enriched target, the intensity of the (110) peak becomes weaker than the (200) peak, but still stronger than the (100) peak.

In the film grown at 635°C with the same target, the (110) peak is weaker than both the (100) and (200) peaks. This represents the best film that we produced since it shows evidence for being both stoichiometric and highly oriented, although there is evidence of a small fraction of BCT (110) misoriented grains. Fig. 2.9 shows the XRD in-plane Φ scan of the 635°C film. The presence of sharp diffraction peaks every 90^{o} indicates that the film is aligned in-plane, indicating that the BCT (100) oriented grains do not contain large-angle grain boundaries. The ratio of the peak area of the (200) to (110) Bragg peaks in the Θ-2Θ coupled scan is greater than 105. When the X-ray structure factors are also taken into account, this indicated that over 99% of the film's crystallites are oriented

epitaxially with BCT (100) || MgO (100) and BCT (010) || MgO (010). The rocking curves for the BCT (200) peaks are shown in Fig.2.8 for the films deposited at 525°C and 635°C (for the same films as in Fig. 2.7). The Full Width at Half Maximum (FWHM) of the film deposited at 635°C is 1.24°. The FWHM of the film deposited at 525°C is 1.88°, which indicates a lower degree of crystallinity.

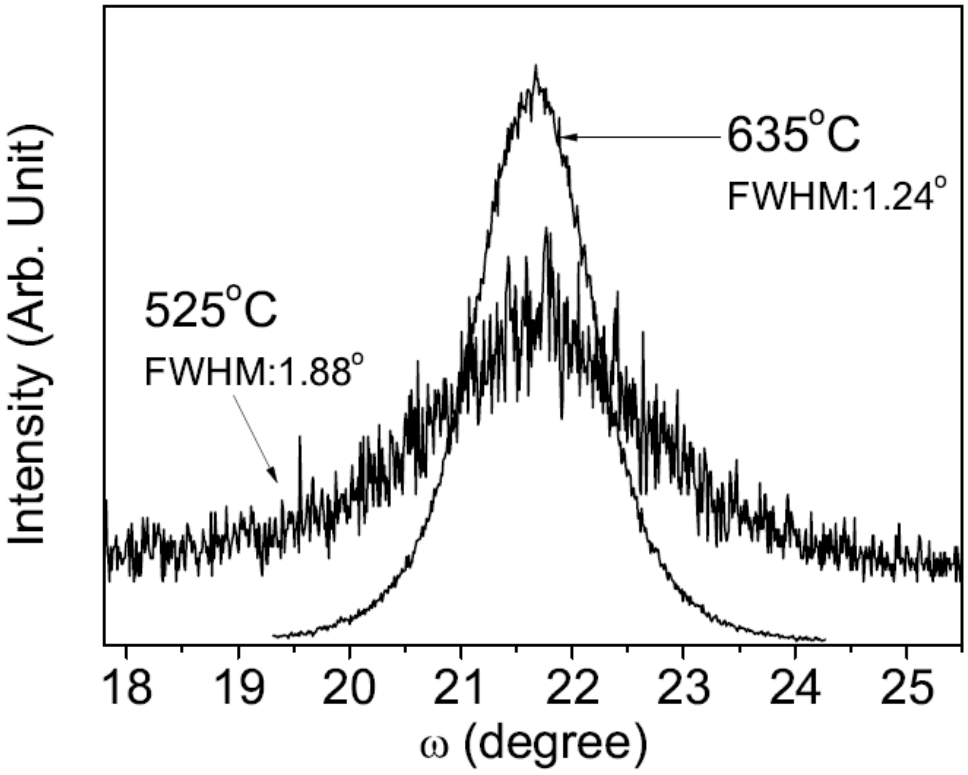

Figure 2.8 XRD rocking curve ω scan of (200) reflection of BCT films grown at 525°C with 75% Cd-enriched target (1 mol BCT : 0.75 CdO), and at 635°C with the 150% Cd-enriched target (1 mol BCT: 1.5 mol CdO). Film thicknesses are 350 nm and 440 nm, respectively.

The lattice constant of films can be accurately determined when the bulk substrate MgO (200) peak position is used as a reference alignment standard. The lattice constants for growths at 525°C, 620°C and 635°C are inferred to be 4.138 Å, 4.149 Å and 4.169 Å. Small shifts are observed that can be attributed to strain in the film.

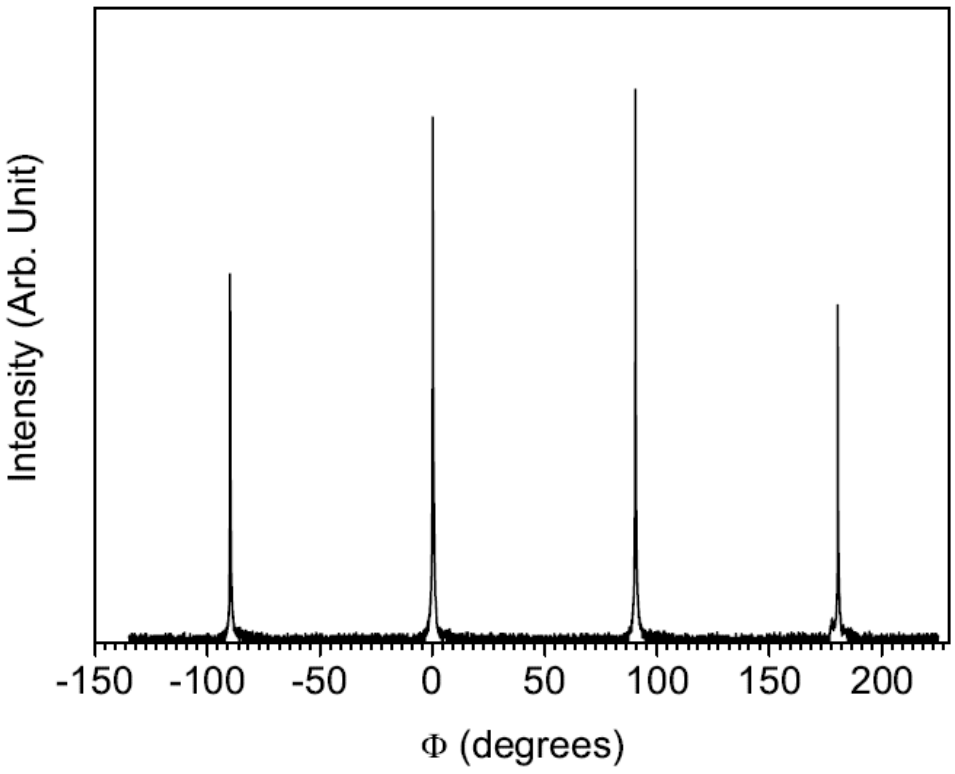

Figure 2.9 XRD Φ scan of asymmetric (202) reflection of BCT films grown at 635°C with the 150% Cd-enriched target (1 mol BCT: 1.5 mol CdO). Film thickness is 440 nm.

Atomic force microscope (AFM) images illustrated in Fig.2.10 give valuable information on the roughness and particle size of the films. We ask the reader to focus on the areas between the large “boulders” (as they are called by the laser

ablation community) and other particles expelled in the PLD process makes such a comparison difficult. The root mean square (RMS) roughness of this portion of the films grown at 525°C and 635°C are in the range of 5 to 6 nm, while the mean particle sizes are about 100 nm. Using the Scherrer formula [20], the lower limit for the mean size of the thin film single crystal "crystallites" is calculated using the software package, X'pert Data Viewer 1.2c (PANalytical B.V. Almelo, the Netherlands) to be 27 nm, 38 nm and 40 nm, for growths at 525°C, 620°C and 635°C, respectively. This indicates that the dominant contribution of the peak broadening in XRD comes from strains induced from the lattice mismatch between the film and substrate.

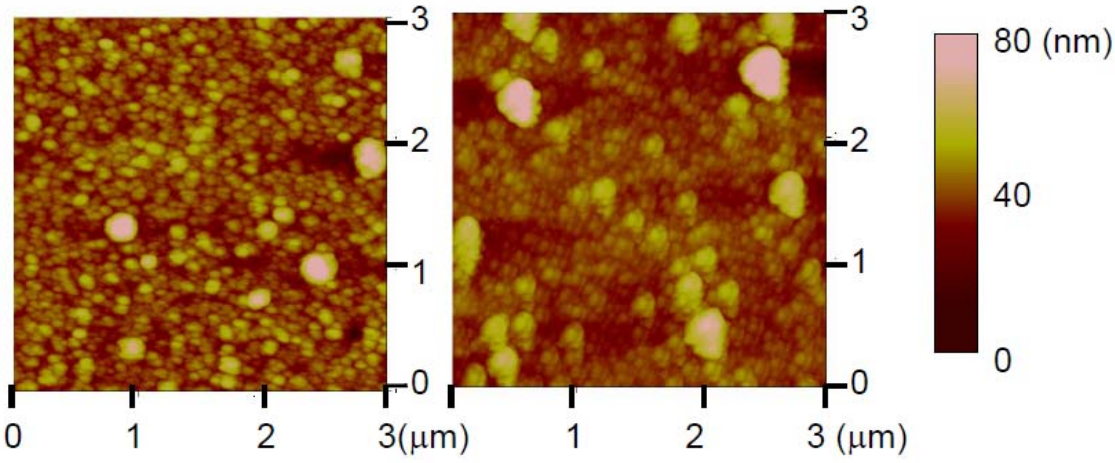

Figure 2.10 AFM images of stoichiometric BCT thin films grown at 525°C with the 75% Cd-enriched target (1 mol BCT : 0.75 CdO) (left) and at 635 °C with the 150% Cd-enriched target (1 mol BCT: 1.5 mol CdO) (right). The films are the same as those used in Fig.2.7

The bandgap is one of the most important intrinsic properties of semiconductors and insulators and can be characterized using optical absorption measurements. For parabolic bands near the band extrema, the relationship between the optical bandgap energy E_g and films absorption coefficient can be determined using the Tauc plot [21]. However, recent local density approximation (LDA) calculations indicate that $Ba(Cd_{1/3}Ta_{2/3})O_3$ is an indirect bandgap material with Ta 5d level in the conduction band minimum and a combination of the Cd 4d and O 2p level at the valence band maximum [7]. It is clear that (a) more than one band extremum will contribute to the near band edge absorption, (b) these bands are not parabolic with energy in this region and (c) both direct and indirect transitions occur within a few 10s of meV within the bandgap; so it is not appropriate to use a Tauc plot to determine the bandgap. Nevertheless, an extrapolation of the linear region of the Tauc plot $\beta(h\nu - E_g) = (\alpha h\nu)^2$ to the energy axis, as is shown in Fig.2.11, would be expected to give a reasonable estimate of the lowest direct transition. This value is expected to fall well within 0.05 eV from the value for the indirect bandgap. Thus, our results, combined with guidance from theory, suggest that the bandgap of BCT, which is indirect, falls at 4.85-4.9 eV. We note that absorption below 4.85 eV varies considerably from sample to sample, depending on the crystal quality, and arises presumably from the presence of shallow level local point defects. Photoconductivity experiment can be used to provide a more accurate value of the bandgap by distinguishing the absorption from the itinerant bands from those of localized defect states.

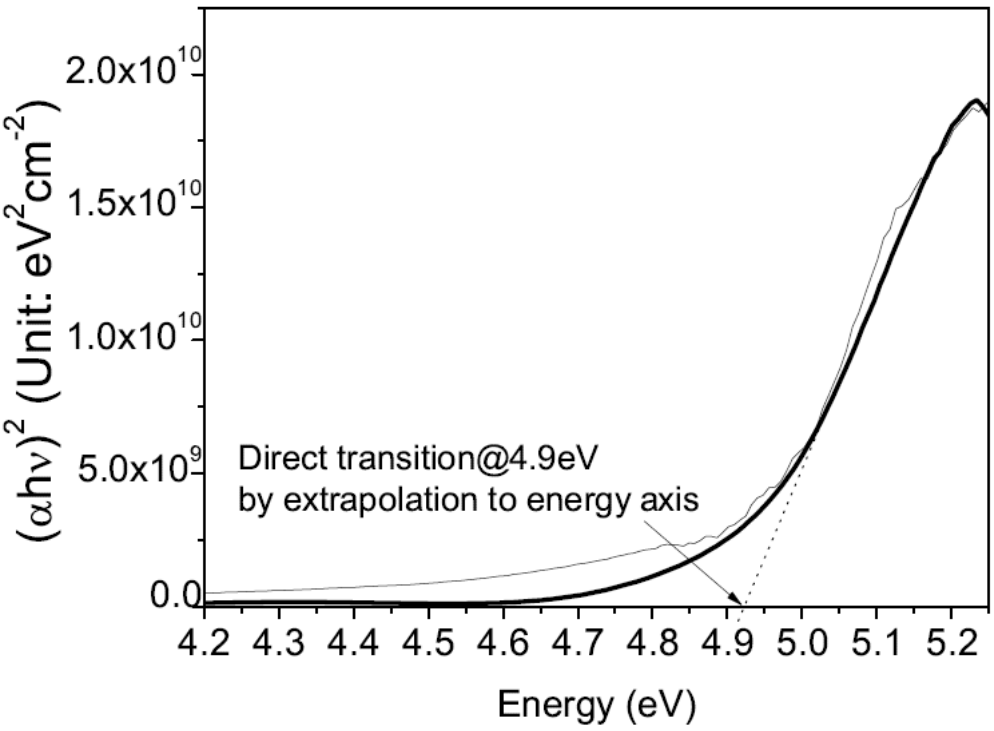

Figure 2.11 Tauc plots for the BCT thin films. Thick solid line is for the film (440 nm thick) grown at 635°C with the 150% Cd-enriched target (1 mol BCT: 1.5 mol CdO), and thin solid line is for the film (390 nm thick) grown at 490°C with the 50% Cd-enriched target (1 mol BCT: 0.5 mol CdO). The light straight dashed lines pointing at ~4.9eV are extrapolation of Tauc plots to the energy axis, which shows the position of the direct optical transition.

The determination of the BCT bandgap energy can shed some insight into the magnitude of the BZT bandgap. An experimental value of 5.3-5.5eV for undoped BZT was reported by reference [14]. It was theoretically calculated using the LDA to be 0.6 eV higher than that of BCT [7]. Since band extrema determined by LDA calculations are typically systematically off in similar compounds because

of errors in the correlation energy, we suggest that 5.3-5.5eV is most likely an accurate value for the intrinsic BZT bandgap. In an earlier paper, the bandgap of Zr and Ni "doped" BZT was reported to be ~ 3.0eV [12]. This value could be in error given the large discrepancy from the value reported for undoped BZT and the expectation that the BZT bandgap is higher than that of BCT (which we report here to be 4.85-4.9 eV). Absorption from Ni internal d-transitions and/or a Ni and Zr deep level band (given the few percent level of doping) could possibly have led to a value smaller than that found for undoped BZT. More work is thus needed to confidently establish the value for the BZT bandgap for undoped and Ni/Zr doped materials.

The refractive index of thin film materials can be determined by fitting the extrema of the interference oscillations in the transmittance spectrum (dashed line in Fig. 2.12) that arises from reflections at the film-substrate interface and film surface. This method was introduced by A.M. Goodman [22] in 1978, and has been used in some other articles to obtain optical constants [12,14,23]. The refractive index is inferred to be 2.1 in the visible range for the BCT film. It is larger than the value of 1.9 found for the BZT film [12]. This is consistent with the Moss relation [24] which predicts that the material with larger bandgap has smaller refractive index.

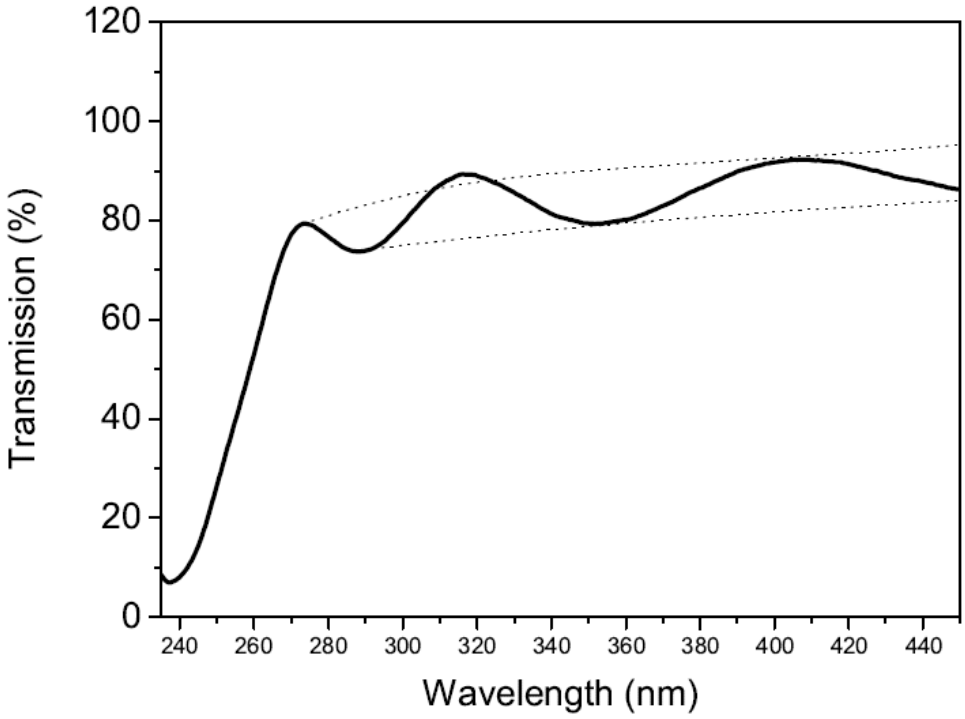

Figure 2.12 Transmission spectrum of the BCT thin film (440nm thick) grown at 635°C with the 150% Cd-enriched target (1 mol BCT: 1.5 mol CdO)

The electrical properties of thin films have been characterized using an interdigital pattern [12,25,26,27,28]. A standard lift-off technique was used to lithographically pattern Ti/Au interdigital electrodes on the 635°C BCT film (440nm thick). The interdigital structure consisted of 40 fingers that were 2-mm long and 20-um wide and were separated by their symmetric partner by 20 μm. A Quadtech 7400 LRC impedance meter was used to measure the capacitance of this interdigital device. The dielectric constant of BCT films could be derived by the Farnell conformal mapping method [12,27,28]. Fig. 2.13 shows the capacitance of the device and the dielectric constant calculated from the formula.

A low frequency dielectric constant of ~32 at frequencies from 1 to 500 kHz is inferred from our measurements. This value is consistent with the ~32-33 value found for bulk ceramics at microwave frequencies [7]. The I–V measurement of BCT films in the interdigital configuration shows the linear relationship which indicates ohmic conduction. Fig. 2.14 plots the log(I)–1/T Arrhenius relationship $I=I_0*exp(-E_a/kT)$ for the ohmic transport currents at 100 kV/cm field. A thermal activation energy, E_a, of ~0.7 eV was inferred from the analysis. The conductivity of this 440nm-thick film is inferred to be 3×10^{-12} Ω-cm at room temperature.

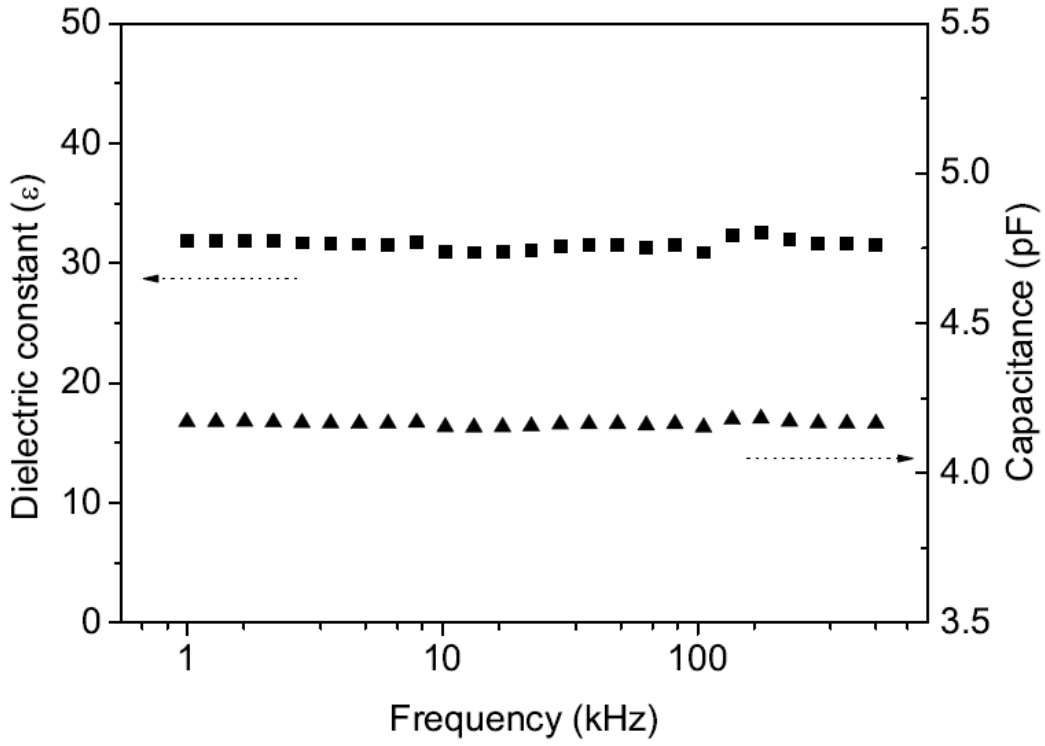

Figure 2.13 Room-temperature dielectric constant of the BCT thin film (440nm thick) grown at 635°C with the 150% Cd-enriched target (1 mol BCT: 1.5 mol CdO), inferred from capacitance measurements of the interdigital structure

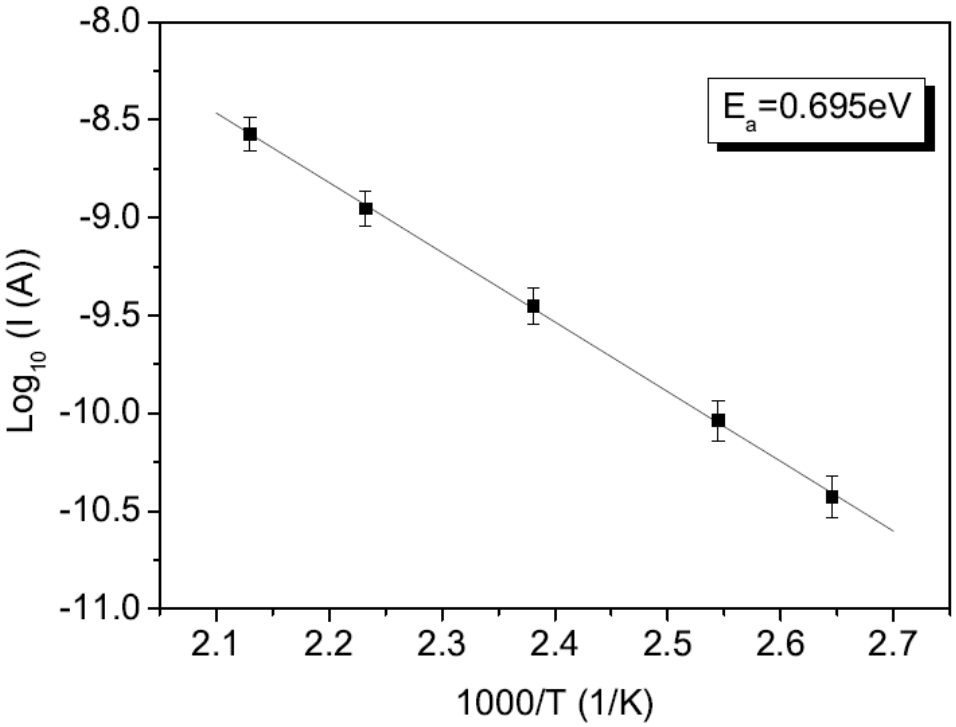

Figure 2.14 Arrhenius plot of current at a field of 100 kV/cm in the BCT thin film (440nm thick) grown at 635°C with the 150% Cd-enriched target (1 mol BCT: 1.5 CdO)

2.2.4 Conclusion

$Ba(Cd_{1/3}Ta_{2/3})O_3$ (BCT) dielectric thin films were grown on MgO (100) single crystal substrates by PLD. The use of enhanced oxygen pressures (53 Pa), Cd-enriched targets (1 mol BCT: 1.5 mol CdO) and elevated substrate temperatures (635 °C) are needed to synthesize stoichiometric films with over 99% of the film growing epitallially [BCT (100) || MgO (100) and BCT (010) || MgO (010)]. We observed that the higher the Cd enrichment in the target, the higher the substrate temperature at which stoichiometric films could be made and the better the

epitaxy. The refractive index of BCT was measured to be 2.1 in the visible range. The dielectric constant of the BCT thin film is 32 at room temperature and low frequency. BCT has a bandgap of ~4.9 eV, as determined by optical absorption methods. Temperature-dependent electrical measurements have determined a room temperature conductivity of 3×10^{-12} $\Omega^{-1}cm^{-1}$ with a thermal activation energy of ~0.7 eV. The mean particle size is ~100 nm and root mean square (RMS) surface roughness is ~ 5 to 6 nm according to atomic force microscopy (AFM) measurements. The excellent structural, optical and electrical properties of the BCT thin films make this system a promising candidate for use in a number of microelectronic and microwave communication applications.

Chapter 3

RESONANCE TECHNIQUES TO ACCURATELY MEASURE THE LOSS TANGENT AND EPR SPECTRUM OF SMALL DIELECTRIC SAMPLES

3.1 Dielectric resonator (DR) method

Dielectric resonator techniques are used to measure the dielectric properties of the ceramic materials. Because the microwave energy is mainly contained within the material, they are less susceptible to influence from external losses.

The sample is loaded inside a gold-plated oxygen free copper cavity, as shown in Fig. 3.1. Reflection (S11) or transmission (S12 or S21) S-parameter measurements are made using the HP 8510C vector network analyzer (VNA) (Fig. 3.2). The position of the extrema in the measurements indicates the resonant frequency.

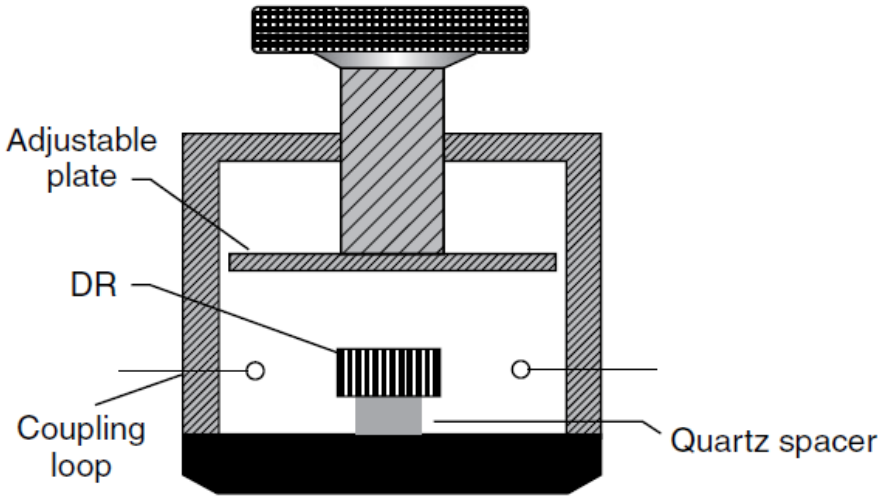

Figure 3.1 Metal cavity loaded dielectric resonator [44]

The position of the sample should be close to the center of the cavity, and supported by a material with low dielectric constant and low loss, e.g. Teflon or quartz, so that it does not interfere with the measurement. The size of the cavity is designed to be about 3 times larger than that of the ceramic material to reduce the near-field conduction losses in the metal walls [44]. Coupling to the transverse dielectric resonator modes are made using a magnetic loop or electric dipole fabricated from the center wire and ground of the coaxial line. The Q is usually measured from the $TE_{01\delta}$ mode. This mode is used because it is a fundamental mode, the field is symmetric with the geometry of the resonator and the cavity resulting in a reduction of radiation at near field losses. The S-paramater characteristicss are shown in the screen of the VNA as fig. 3.2 shows. From this information, the resonant peak position (f_0) and 3 dB band width (Δf) can be readily determined. The Q factor can be estimated from $f_0/\Delta f$. In order to accurately measure the Q factor and thus the loss tangent of the materials, we have to calibrate the VNA and use a curve fitting technique to eliminate the influence of the coupling probe effects. The calibration is performed using the calibration kit (Agilent 85052D, 3.5mm Economy Calibration kit). Short, open and broad band load determinations were made at the end of the rf coaxial line. The VNA used this information to calibrate the VNA so that accurate vector measurements can be made. The curve fitting was completed by using the software QZERO [45]. This programs fits the Smith chart circle of a resonant peak and calculates the loaded Q, unloaded Q and coupling coefficient as shown in Fig. 3.3.

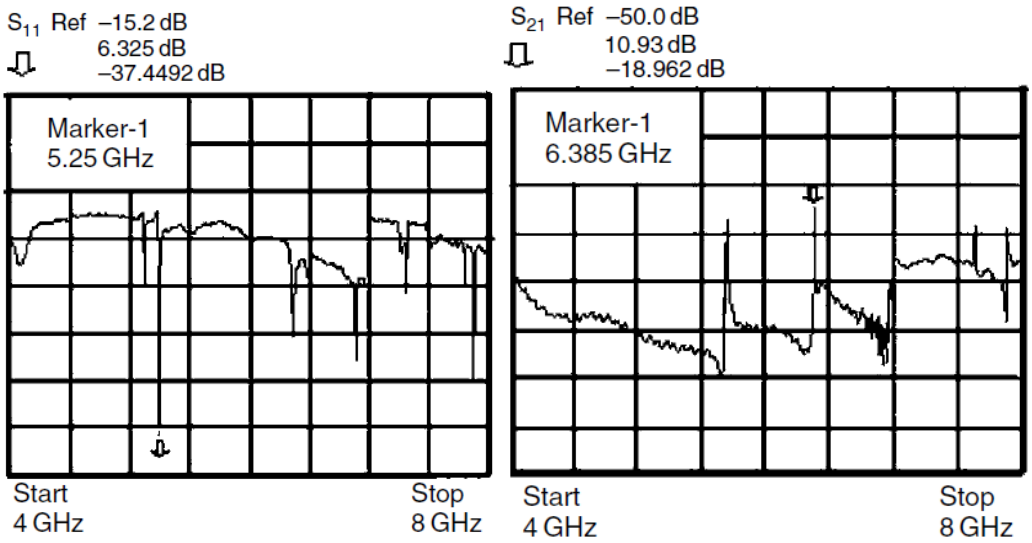

Figure 3.2 S11 and S21 response curve in HP8510C for dielectric resonators [44]

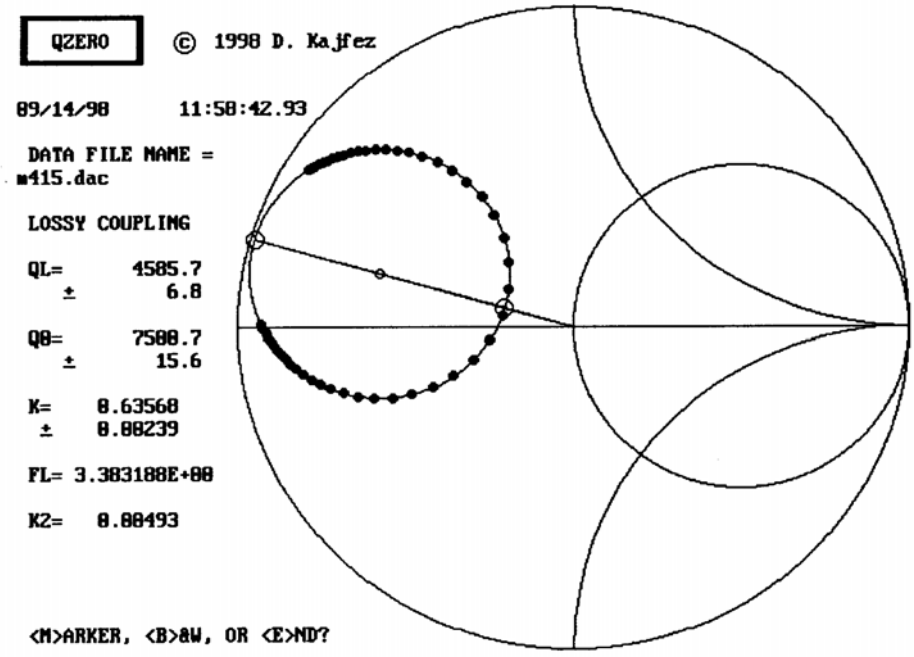

Figure 3.3 Smith chart curve fitting for calculating unloaded Q factors [45]

3.2 Superconducting parallel plate resonator (PPR) method

A superconducting parallel plate resonator (PPR) technique using very thin dielectric spacer material was used by R.C. Taber to measure the surface resistance of superconductor films [30]. Fig. 3.4 shows the schematic of the resonator structure. This method has been widely used for this purpose [31-35] because of its many advantages. First of all, it eliminates the need for patterning of the superconductor film or other sample preparation. Secondly, the high quality factors leads to a very sensitive measurement of the surface resistance. Thirdly, the use of well-defined principle and higher order resonances results in well-understood relatively-uniform electric and magnetic field distributions.

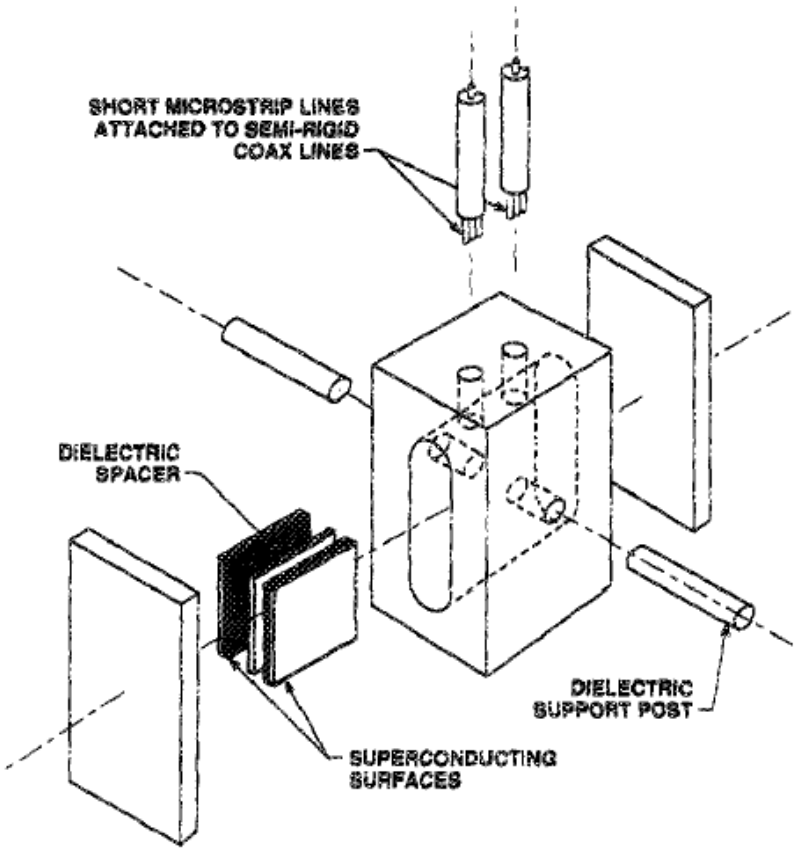

Figure 3.4 Superconducting parallel plate resonator schematic [30]

In this work, we show that this method also has advantages for measuring the loss tangent of dielectric samples over the commonly used $TE_{01\delta}$ cavity loaded dielectric resonator (DR) method [36-39]. Besides the high sensitivity, the sample volume of the interlayer dielectric used in the PPR is almost two orders smaller than that needed to make dielectric-resonator loss-tangent measurements in the same frequency range. Thus, the PPR method can minimize the volume of material needed. Also, since a single small high-loss defective region can skew the Q measurement of a conventional industry-standard $TE_{01\delta}$ dielectric resonator [36-39], this method can determine the material uniformity by measuring many samples from a single $TE_{01\delta}$ resonator.

The PPR technique uses small microwave surface resistance films of Nb (for measurements up to ~8 K) and $YBa_2Cu_3O_{7-\delta}$ (for measurements up to ~80 K) to determine the loss tangent as a function of temperature. We then use these results of these PPR measurements as a standard to determine the accuracy of the DR measurement technique. That work demonstrates that the DR is accurate and is thus able to be used over much wider temperature (2-400 K) and magnetic field (0-9 T) ranges.

3.3 Experimental setup

The loss tangent measurements are performed in a gold-plated copper RF cavity (2.03 cm x 0.61 cm x 1.52 cm) which is affixed to the end of a cryogenic

dipping probe. The details of the structure of the dipping probe are described in Taber and other researcher's work [30,35]. The fixtures we used to affix the microwave cavity and its surrounding isolation can to the stainless steel tube were modified to have less than a 2.5 cm cross-sectional diameter. This enables them to fit into a neck of a liquid helium dewar for 4 K measurements without a field or in a cryostat, Physical Properties Measurement System (PPMS) (Model 6000, Quantum Design, San Diego, CA), for temperatures scans from 2 to 400K and magnetic fields scans as high as 9 Tesla. A gas-tight seal for the probe is crucial to eliminate contamination from entering the cryogenic region (most importantly, icing), particularly in the case of the commercial PPMS system. As shown in Fig. 3.5, a coupler and Wilson-type O-ring compression seal is used to connect and make it gas tight for the stainless steel support tube (1.27 cm diameter and 0.8 mm thick). On the top part of the dipping probe, two small O ring (2.1mm inner diameter, 5.1mm outer diameter) compression seals clamped in a single structure are used to seal the holes for the 0.085'' microwave coax cables (silver plated copper inner conductor, stainless steel outer conductor, 50Ω, 4.8 dB/m attenuation, UT-085-SS, Micro Coax, Pottstown, PA) in the top metal support block, as is shown in the right part of Fig. 3.5.

Transmission measurements are made using an HP8510C microwave vector network analyzer (VNA) to excite fundamental electromagnetic and higher resonance modes and record the associated S_{21} vector values. These values are fit to a circle in the Smith chart [37] to infer the quality factor. The distance between coupling loops and sample is adjusted to be weakly coupled so that the unloaded

Q can be determined to better than a few percent. Because only the value of the quality factor is sufficient to infer the loss tangent, a calibrated measurement is not required.

For measurements in the commercial PPMS cryostat, the Labview (National Instruments, Austin, TX) program was made to (a) automatically set the magnetic field and temperature in the PPMS, (b) set the measurement range and initiate the measurement in the VNA and then (c) retrieve the resulting data from the VNA. A Matlab script for fitting a circle on the Smith chart to determine the unloaded Q [41] was inserted into the Labview computer module.

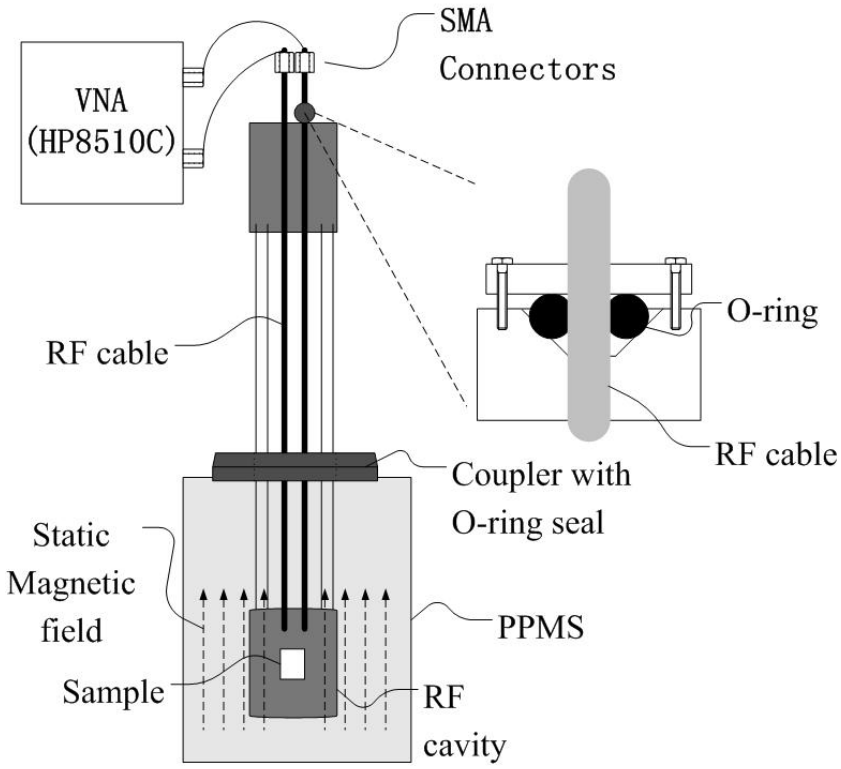

Figure 3.5 Experimental schematic for quantitatively measurement of the loss tangent and EPR spectrum of small dielectric samples over a range of temperatures and magnetic fields

3.4 Measurement techniques and results

3.4.1 Measurement of loss tangent at liquid helium temperature using Parallel plate Resonator (PPR) technique

3.4.1.1 Experiment and theoretical model

The resonator consists of two superconducting films and one dielectric spacer, and the spacer is placed between these two superconductor films to form a sandwich structure. The resonator is then placed inside a small cavity made of oxygen free high-conductivity copper (OFHC) which is gold (purity>99.9%) plated to minimize the radiation loss. The details of this device are well described in some references [30,34,35,42]. Here we use Nb films deposited on Yttrium stabilized Zirconia (YSZ) substrates by sputtering deposition in the MIT Lincoln lab. On the spacer part, we choose several different materials. These include 2-inch Silicon wafers (Virginia Semiconductor Inc., Fredericksburg, VA) of both undoped (25 μm thick ultrathin®, (100) orientation, resistivity >20 Ohm -cm) and lightly doped n-type (125 μm thick, resistivity >100 Ohm-cm) ones, Teflon® FEP films (Du Pont Electronics, Wilmington, DE, 12.5 μm thick), 2-side polished c-sapphire substrates (1cm×1cm×0.5mm, MTI Inc, Richmond, CA), and $Ba(Zn_{1/3}Ta_{2/3})O_3$ ceramics chips. The ceramic was sintered by traditional powder processing way and has a Q of 25,000 scaled to 2GHz at room temperature. The

undoped and lightly doped Silicon wafers in this work can freeze-out at 4.2K and shows a very low microwave loss tangent. Two 50-Ω semi-rigid coaxial cable probes can be moved close or away from the resonator to excite resonance modes. The whole sample was placed in a dipping probe which can be inserted in the liquid Helium Dewar. The other ends of the cable were connected to HP 8510C vector network analyzer, from which S12 or S21 network parameters can be collected. The input source power should be chosen neither too large in case of the nonlinear effect [35], nor too small in order to get a good signal to noise ratio of the S12 or S21 signal intensity. It should be kept above 10 to 15dB to measure an accurate 3-db bandwidth of the transmission coefficient. The distance between tips of coaxial probes and the resonator was adjusted to be within tenths of a millimeter to get a weak coupling, in which case the loaded Q and unloaded Q is approximately equal to each other. Usually, at the beginning of the experiment, the probes were moved barely touch the sample. During the experiment, the distance was increased to lower the coupling coefficient until the weak coupling needed reached. The sharp peaks in S21 or S12 diagram corresponds to the resonant modes. These modes can be distinguished from the cavity modes easily by observing the shift of resonate frequency [34,35,36] with the change of temperature, while the cavity modes don't shift obviously. This phenomenon is due to the variance of skin depth of superconducting films with temperature.

For the superconducting films, we use 1 cm^2 Nb films deposited on Yttrium stabilized Zirconia (YSZ) substrates fabricated with sputter deposition (MIT Lincoln lab) and $YBa_2Cu_3O_{7-\delta}$ films deposited on buffered sapphire substrate (STI

Inc.). The Nb films used in this work have slightly lower surface resistances (~12 μΩ/□ at 4.2 K, scaled to 6.5GHz) and give higher Q values. However, because of Nb's low critical temperature (T_c) of 9.2 K, it can only be used for measurements up to ~8 K before the loss from the superconductor begins to dominate. On the other hand, the $YBa_2Cu_3O_{7-\delta}$ films can be used to measure a relatively large temperature range (up to ~80K).

For the interlayer dielectric, we used a number of low loss materials with specifications as follows.

(a) Silicon (100)wafers , ε_r=11.7, Virginia Semiconductor Inc., Fredericksburg, VA

i. undoped, 25 μm thick, resistivity >20 Ω-cm

ii. lightly doped n-type, 125 μm thick, resistivity >100 Ω-cm

(b) Teflon® FEP films, ε_r=2.1, DuPont Electronics, Wilmington, DE, 12.5μm thick

(c) high-performance microwave dielectric $Ba(Zn_{1/3}Ta_{2/3})O_3$ ceramics, ε_r=29

i. commercially produced, Trans Tech, Adamstown, MD

ii. made in our lab using conventional powder processing methods.

The overall unloaded Q of the resonator can be modeled by the equation [30]

$$Q^{-1}=Q_d^{-1}+ Q_r^{-1} + Q_c^{-1}= \tan\delta+\alpha s+(\beta R_s/s). \qquad \text{Equation 3.1}$$

In this equation, the first term is the loss tangent of dielectric spacer (dielectric loss), the second term is from near-field energy radiation from the surrounding of

the resonator (radiation loss), and the third term is caused by surface resistance of superconductor films (conduction loss). The three have different dependence on the spacer thickness. Dielectric loss is independent of spacer thickness; the radiation loss is proportional to the spacer thickness, and the conduction loss is inversely proportional to it. α and β are the associated coefficients. $\beta=1/(\pi\mu_0)=3.9\times10^{-5}$m/$\Omega$ at 6.5GHz [30], and α is different from sample to sample.

To accurately measure dielectric loss using this technique, the dielectric loss, quantified by tan δ, must dominate over other two terms. For this, we need to determine the optimal thickness of the spacer, which corresponds to when the interlayer thickness is varied to maximize the Q. In Fig. 3.6, we illustrate our results of the Q measurements as a function of the Si thickness. Si was chosen because very thin, smooth and high purity samples are available. They can thus be easily stacked to obtain different interlayer distances between 12.5 μm and 500 μm. Clamping them together tightly can minimize the influence of the air gap between layers. The presence of an air gap can be detected and quantized by maintaining the sample at 4.2 K and measuring the frequency shift between cycling between liquid He and the gas environment. The presence of an airgap is characterized by a sudden shift in frequency as a result of the difference in the ε_r of liquid He (1.05) versus gaseous He (~1.00).

3.4.1.2 Results

Fig.3.6 shows the relation between unloaded Q factor of the PPR and the Si spacer thickness. The unloaded Q increases almost linearly at spacer thickness

less than 100μm, because the superconductor surface resistance loss dominates in this range. At thicknesses larger than 100μm, the unloaded Q decreases because the dielectric loss and near-field radiation loss become more important. At around 175 μm, the unloaded Q reaches its maximum of ~165,000 at 6.5 GHz. After fitting the curve, at 6.5 GHz, we surmise an R_s of ~12 μΩ/□ for the Nb films, tan δ of ~ 10^{-6} for silicon wafers, and α of 1.2×10^{-2} m^{-1}.

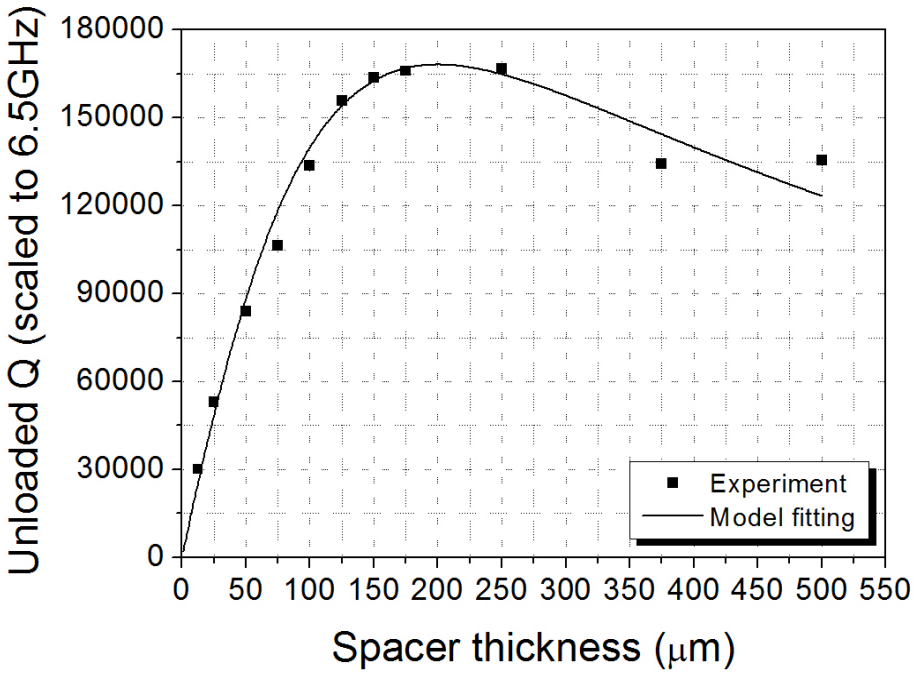

Figure 3.6 Unloaded Q versus dielectric spacer thickness of parallel plate resonator (PPR) at 4.2K. The first data point at a thickness 12.5μm was measured using Teflon. The data at thicknesses between 25 and 100μm were measured using the 25μm thick undoped silicon wafer(s), and those between 125 and 500μm were measured using the 125μm thick lightly doped n-type silicon wafers.

We find the sensitivity of the tan δ measurement for a material with a ε_r of 11 to be 5 x 10^{-7} at 6.5 GHz by determining the top of the range of loss tangent values that can be used to fit the results to within experimental error. Note that, α is inversely proportional to square root of ε_r, so the near-field radiation loss will be lower for higher dielectric constant material, such as BZT, and thus the sensitivity would be expected to be proportionately lower.

The results with Nb thin films at 4.2K and other dielectric materials, sapphire, BZT and Teflon, are also listed in Table 3.1. We also demonstrated results of other BZT samples doped with other dopants, such as Ga, Zr, Mg, Ni, Mn etc., in our recent paper [40]. Fig. 3.7 show the unloaded Q factor of PPR with C-sapphire and YBCO thin films. As is shown, at 4.2K the Q is larger than 90,000 at 6.5GHz, and with temperature goes up, the Q decrease. When T is beyond 70K, the Q drops sharply and finally the S21 resonant peak disappear as a result of increasing of the surface resistance of the superconductor films.

Table 3.1. Summary of the PPR measurement with different spacer materials at the temperature of 4.2K using Nb films

Spacer material	ε_r	t (μm)	Q_u	f_0 (GHz)	Q_u (6.5GHz)
Silicon	11.7	175	158,590	6.80	165,910
C-Sapphire	11.5	500	59,123	6.85	62,307
$Ba(Zn_{1/3}Ta_{2/3})O_3$	29.0	450	55,119	5.38	45,579
Teflon FEP	2.1	12.5	17,696	11.08	30,165

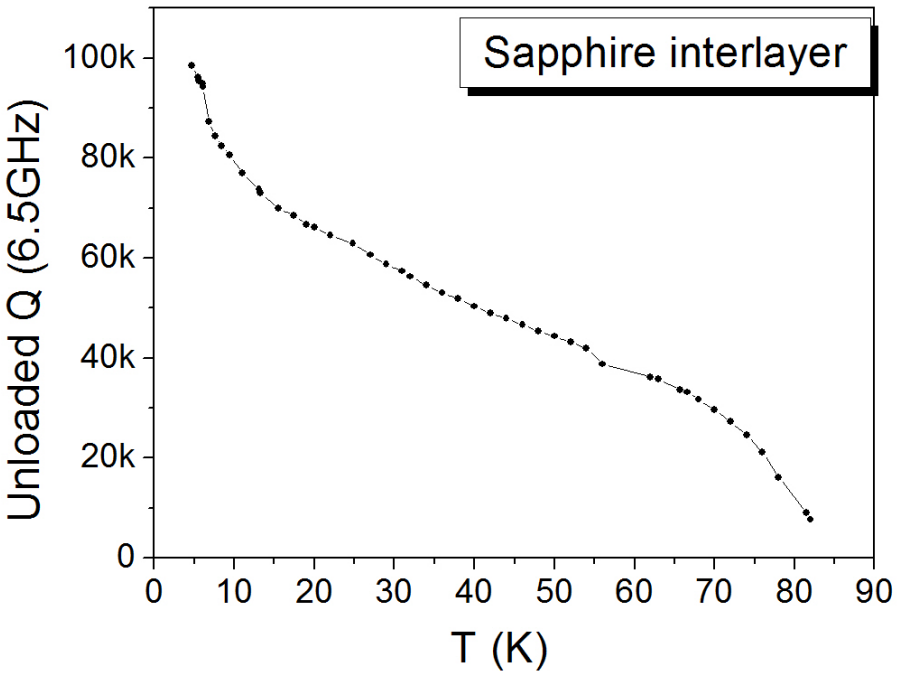

Figure 3.7 Unloaded Q as a function of temperature with YBCO thin film and C-sapphire as a interlayer insulator

3.4.2 Measurement of loss tangent dependence on temperature

The temperature dependence of loss tangent for BZT samples is shown in Fig.3.8. In Fig. 3.8, the gray circular dots show the Q values of PPR with $0.05BaZrO_3$-0.95BZT (5%Zr doped BZT) interlayer dielectrics and $YBa_2Cu_3O_{7-\delta}$ films. The Q x f value is more than 400 THz at 4K. However, the surface resistance R_s of $YBa_2Cu_3O_{7-\delta}$ films increases with increasing temperature [31,32], especially near T_c. The R_s at 77K is at least one order larger than that at 4.2K [31,32], which causes the sharp drop of Q and a reduction in the sensitivity of this method at those temperatures. By using the R_s values in ref. [31,32] as an estimate,

we can deduct the effect of surface resistance, and the results are shown in Fig. 3.8 as the hollow circular data point. The corrected data matches the value measured by the dielectric technique to a reasonable extent over temperatures from 4.2K to 80K.

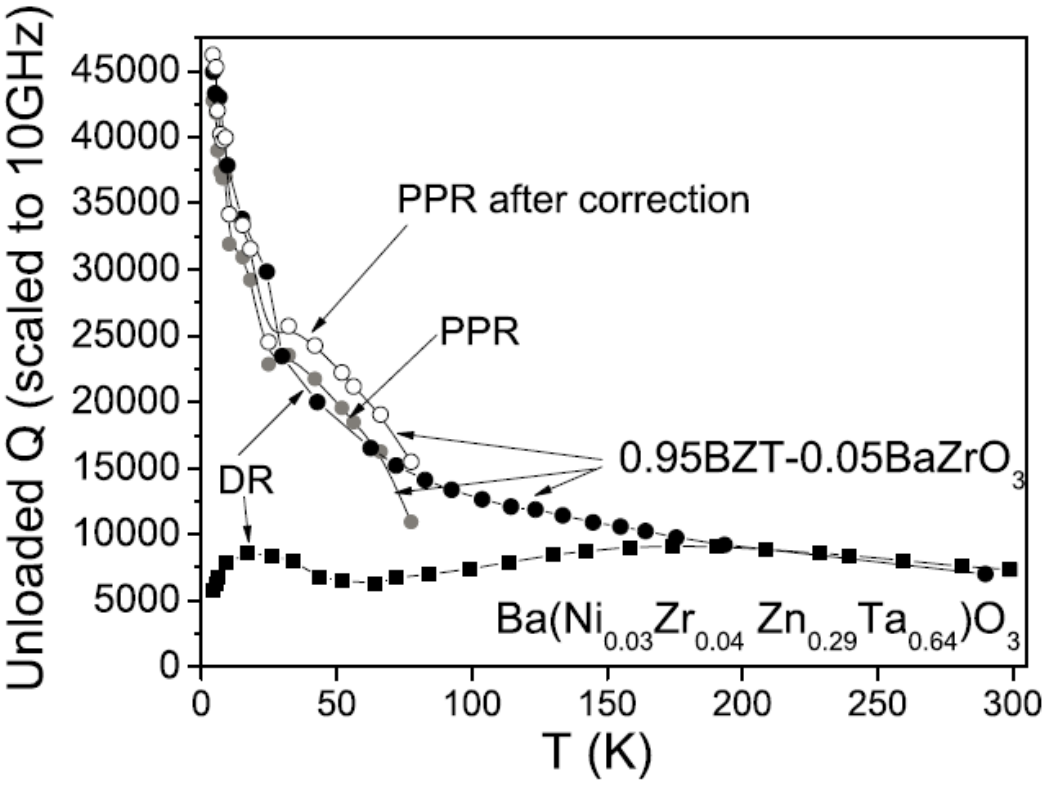

Figure 3.8 Temperature dependence of Unloaded Q of BZT samples. The black solid cube data points are for Ni and Zr doped commercial BZT (D2900, Trans Tech, $Ba(Ni_{0.03}Zr_{0.04}\ Zn_{0.29}Ta_{0.64})O_3$). The circular data points are for 0.95BZT-0.05$BaZrO_3$ made in our lab. The black solid circular data points are measured using DR method, the gray circular data points are measured using PPR method, and the hollow circular data points are inferences of the corrected Q values after

the conduction loss (Q_c^{-1}) term of $YBa_2Cu_3O_{7-\delta}$ films in equation 1 is deducted from the measured loss (Q^{-1}).

To extend the temperature range and facilitate measurements in large magnetic fields, the DR method was introduced. This technique does not use superconductor materials in the measurements, so does not have the same restrictions in temperature or magnetic field that the PPR method does.

For the DR measurement, the BZT sample was cut into a small rectangle (8.5mm x 6.5mm x 2mm) and inserted into the center of the gold-plated copper cavity. The S_{21} parameter was measured for the fundamental resonator mode at ~10 GHz. The unloaded Q factor was then determined.

In fig. 3.8, the black solid data points show the results measured with DR method. The Q values of 5% Zr doped BZT samples are represented by black circular solid data points. As is shown at very low temperature, PPR gives slightly higher Q values. As the temperature increases, the Q measured using PPR drops sharply and become lower than that measured using DR at around 80K. On the other hand, DR gives reasonably good results over the entire temperature range of 4 K to room temperature.

The Q of 5%Zr doped sample shows a monotonic increase as the temperature drops. The commercial BZT (D2900, $Ba(Ni_{0.03}Zr_{0.04}Zn_{0.29}Ta_{0.64})O_3$, Trans Tech, Adamstown, MD) sample includes 3 mol% Ni and 4 mol% Zr doping, and it shows a totally different temperature dependence. The trend from 200 to 300K follows as the other one, but when the temperature drops below 20K, the Q shows a fast drop down to 4K. The mechanism for this difference was identified as the

electron paramagnetic loss from Ni clusters coupled by the exchange energy in this moderate doping concentration in the BZT sample in our recent work. [40]

3.4.3 Measurement of loss tangent dependence on magnetic field

In order to quantitatively investigate the influence of magnetic field on the loss tangent, we carried out DR measurements that will be described in this section. The superconductor properties are strongly affected from the presence of the magnetic field, so the PPR technique is precluded from such studies.

The use of the DR technique as a function of magnetic field allows the exploration of the effect of spin excitations, including EPR processes, on the loss tangent. In our work, the measurement is realized with magnetic field up to 9 Tesla using the superconducting magnet in the PPMS system. In fig. 3.9, the magnetic dependence of the Ni and Zr doped commercial BZT sample is shown from zero field to 8 Tesla. As the magnetic field is increasing, the Q factor shows a strong dependence, a broad increasing background from zero magnetic field to 8 T and a sharp dip around 3500 Gauss. The feature at ~3500 G with a g factor of 1.98 is due to the free carrier EPR absorption. The Q factor saturates at about 6 T to 35,000 scaled to 10 GHz, which is 8 times larger than that without magnetic field.. This measurement clearly shows that the loss tangent at cryogenic temperature is dominated by loss from spin processes.[40]

We also measured Mn and Co doped BZT samples. Fig. 10 shows the result of 0.25 mol% Mn doped BZT measured at room temperature. It shows strong

magnetic dependence where EPR occurs for the unpaired d-electrons of the Mn^{4+} ion.

In the inset of Fig. 3.10, we include a finer resolution scan of EPR feature with a step resolution of 1 Gauss around the center of the peak and 5 Gauss away from the peak. Note that the center part clearly shows 6 peaks due to the hyperfine structure from the Mn^{4+} nuclear spin of 5/2. The g factor is determined to be 2.02. The average distance between each hyperfine peak is 87 Gauss, which indicates the hyperfine coupling constant A to be 7.97 x 10^{-3} cm^{-1} ($A=\Delta H\hbar\nu/H_0$) [43]. This is similar to Mn^{4+} ion in MgO matrix, which exhibits an A of 7.08 x 10^{-3} cm^{-1} [43].

We also measured 1 mol% Co doped BZT sample. The Q curve of the Co doped sample doesn't show obvious magnetic dependence at room temperature, which is different from that of the Mn doped sample. At lower temperature, the magnetic dependence is readily observed. Measurement at 70 K shows a g factor of 4.35, which is close to g of 4.28 for Co^{2+} in MgO matrix [43]. Since Co nuclear has spin of 7/2, 8 hyperfine peaks are expected around the center. However, the one observed peak is broad without clear evidence of hyperfine peaks, presumably because that peak is broadened by dipolar interactions or the anisotropic properties of g factors in the Co doped polycrystalline sample [43].

In the conventional EPR system, it is operated using a Cu cavity mode which usually has a Q on the order of 5,000. The small change in the cavity Q is measured by a diode detector and the noise is minimized using a narrow bandwidth lock-in amplifier. In this work, we measure the dielectric resonator mode in which the electromagnetic field is essentially completely confined within

the dielectric. Therefore, the improved fill factor and higher Q makes this technique potentially orders of magnitude more sensitive to the energy absorption of the material than a conventional EPR system. Our technique also has the advantage of using a well-defined principle and higher order dielectric resonances results with the corresponding near-unity fill factors and well-understood relatively-uniform electric and magnetic field distributions. This enables accurate loss tangent measurements without the use of standards or other methods of calibration.

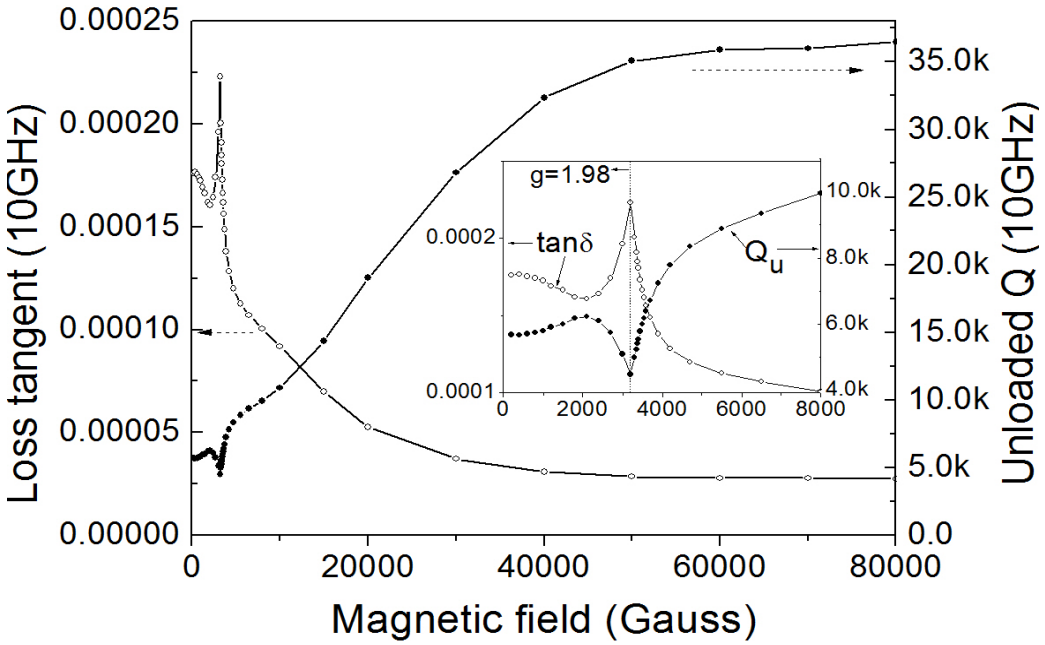

Figure 3.9 Magnetic dependence of Unloaded Q and loss tangent of Ni and Zr doped BZT (D2900, Trans Tech) sample measured using DR at 4.2K.

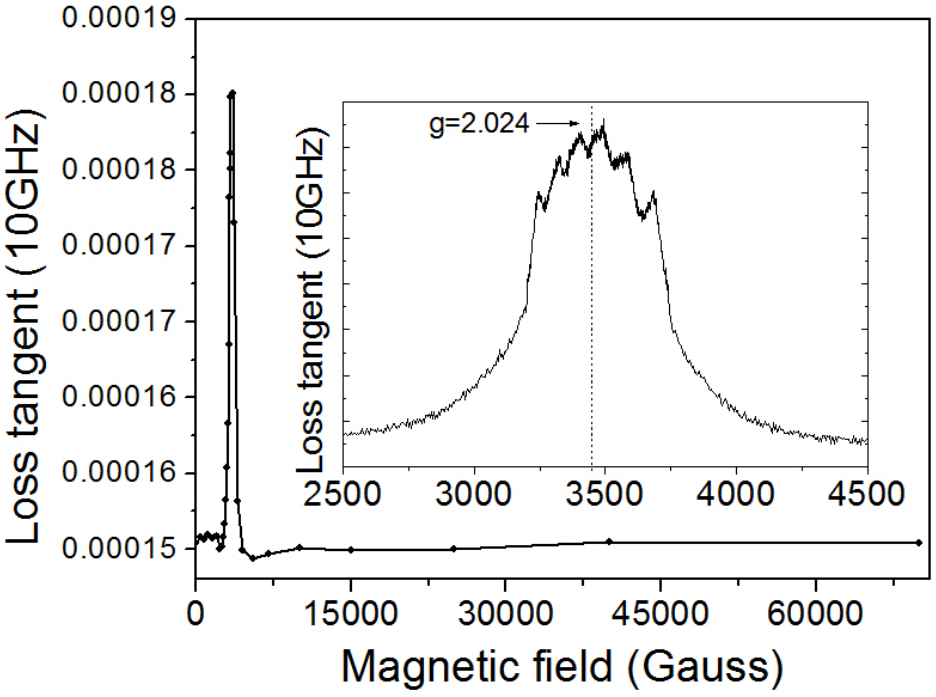

Figure 3.10 Magnetic dependence of microwave loss tangent of 0.25 mol% Mn doped BZT sample measured using DR technique at room temperature.

3.5 Conclusion

We use both parallel plate resonator (PPR) and dielectric resonator (DR) structures to accurately determine the loss tangent of small dielectric samples over a range of temperatures and magnetic fields. This facilitates quantitative Electron Paramagnetic Resonance (EPR) measurements of solid samples. The techniques that we use have a sensitivity of better than 5×10^{-7} at 6.5 GHz for measurement of loss tangent of materials with a dielectric constant, ε_r, of 10 and even achieve higher sensitivity for materials with larger ε_r. The use of well-defined principle and higher order resonances results in well-understood relatively-uniform electric

and magnetic field distributions. The compact nature of the microwave cavity that we use allows measurements to be made in a number of platforms, including the necktube of a liquid helium storage dewar (4-300 K) and PPMS (2-400 K, 0-9 T).

Chapter 4

THE DOMINANCE OF PARAMAGNETIC LOSS IN DIELECTRIC MATERIALS AT CRYOGENIC TEMPERATURES

4.1 Background introduction

Condensed matter theoreticians have developed tools that can accurately predict intrinsic and extrinsic physical properties of solid state materials [46]. This demonstrates that there is a strong understanding of the underlying mechanisms responsible for their electronic, optical, magnetic, chemical, thermal and structural characteristics. However, a fundamental understanding of what determines one of the most important parameters, the loss tangent, has still not been established, especially in practical high performance dielectrics, and warrants further attention by the basic science community.

Researchers to date have identified several processes that can cause microwave loss including absorption by free carriers [47,48], electron paramagnetic resonance [49], anharmonic-phonons [50-54], 2-level systems with precession of electric dipoles in polar molecules [55,56] and non-resonant spin-excitations in exchange coupled transition-metal defect complexes [57,58]. The important question is which of these, if any, is responsible for microwave loss in practical microwave dielectrics.

This work investigates $Ba(Zn_{1/3}Ta_{2/3})O_3$ (BZT), a low loss tangent ($<2 \times 10^{-5}$ scaled to 2GHz) and high dielectric constant (~30) material that can be tuned with ~12% Ni-doping on the Zn-site to achieve a microwave device zero temperature coefficient of resonant frequency [59]. A small fraction of $BaZrO_3$ is often alloyed

with this compound since it improves the manufacturability of the material by allowing shorter annealing times to achieve low loss [59]. Interest in high dielectric-constant low loss dielectrics is of great technological importance. Losses in dielectric resonators and filters limit the performance of most microwave communication and radar systems. One strategy to reduce loss is to operate these dielectrics at reduced temperatures. If optimized for cryogenic temperatures, the use of these materials could potentially also positively impact quantum computing, photonic detector, amplifier and mixer circuitry, as the performance of these advanced electronics is often limited by ac losses and the associated noise [60,61].

Recent reports of the loss tangent of practical microwave materials have found a variety of behavior ranging from a strong increase to a significant drop in the loss tangent at low temperatures [62-66]. An understanding of the dominant loss mechanism under these conditions is lacking and is the focus of this study. Our approach is to quantitatively measure the temperature and magnetic field dependent loss tangent of undoped and doped BZT using microwave resonators whose quality factors (Qs) are limited by dielectric loss. These results, combined with pulsed EPR measurements, show conclusively that the dominant loss process in transition metal doped BZT results from resonant spin excitations of unpaired d-electrons within isolated impurity atoms for small dopant concentrations and within exchange coupled clusters for higher concentrations.

4.2 Brief introduction to Electron paramagnetic resonance (EPR)

Electron paramagnetic resonance is a technique for studying chemical species that have one or more unpaired electrons, such as organic and inorganic free radicals or inorganic complexes possessing a transition metal ion. The basic physical concepts of EPR are analogous to those of nuclear magnetic resonance (NMR), but it is electron spins that are excited instead of spins of atomic nuclei. The Zeeman effect is the basic physical principle. It means when the magnetic field is applied in the spin system, the degenerate energy levels will splits which is proportional to the amount of magnetic field. When the photon energy (usually in the microwave range) matches with the energy splitting, a resonance absorption of photon energy will occur. The Zeeman effect is expressed as

$\Delta E = \mu_B g B$ Equation (4.1)

Where μ_B is Bohr magneton, g is the Lande factor and B is the external magnetic field.

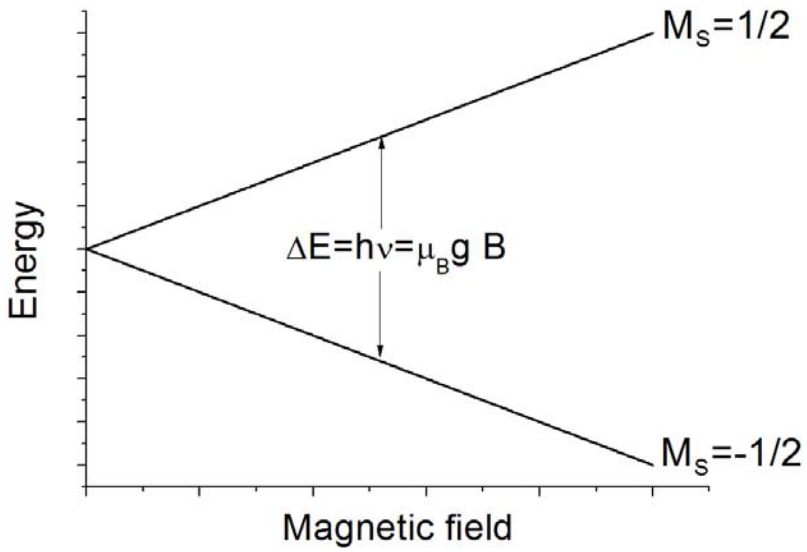

Figure 4.1 Zeeman effect in a spin S=1/2 system

The Hamiltonian of the spin system in the EPR can be written as

$H=\mu_B\ g\ \mathbf{B \cdot S} + 1/2J(S(S+1)-2s(s+1)) + D(S_z^2 - 1/3S^2 + E/D(S_x^2-S_y^2)) + \mathbf{S \cdot A \cdot I}$

Equation (4.2)

The first term is the Zeeman effect, the second term is the exchange interaction, the third term is the Zero field Splitting (ZFS) term and the fourth one is the hyperfine structure term due to the interaction of spins of nuclear and electrons. The exchange term become important when the distance between ions become shorter and then the electron wave function from different ions overlaps more. In this condition, the isolated ions are coupled with each other through exchange interaction and they are treated as a single spin cluster. The ZFS term is considered when D, E parameters are not zero and the spin of the system is larger than 1/2, as is shown in Fig. 4.1. In this S=1 case, there are possibly two resonant peaks corresponding to a certain microwave energy instead of only one peak in S=1/2 system (Fig. 4.2). ZFS term comes from electron spin-orbital or spin-spin interactions in a special crystal field.

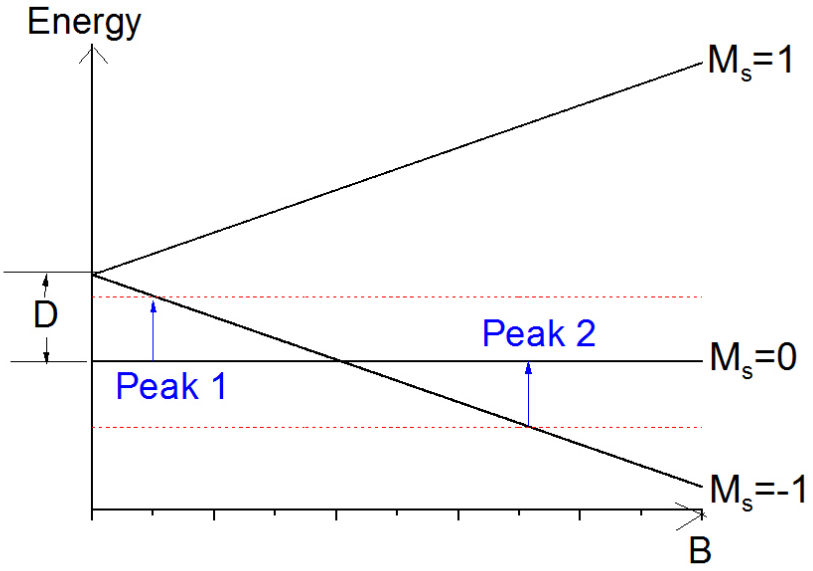

Figure 4.2 EPR energy level chart with S=1 spin system and non-zero ZFS D value.

4.3 Experimental methods

Undoped and Cd, Ga, Mg, Mn, Ni, and Zr-doped BZT ceramic samples were synthesized using conventional solid-state powder processing techniques in our lab. Sintering was performed in air at 1550 °C for 15 hours. A more complete description of the synthesis methods is described elsewhere [67]. Co-alloyed $BaZn_{1/3}Nb_{2/3}O_3$ with 67% of Zn replaced by Co [i.e. $Ba(Zn_{1-0.67}Co_{0.67})_{1/3}Nb_{2/3}O_3$], $ZrTiO_4$-0.1$ZnNb_2O_6$ and $BaTi_4O_9$-0.43$BaZn_2Ti_4O_{11}$ materials were produced in a commercial product line.

Microwave measurements to infer the loss tangent of the dielectric materials are performed in transmission-type quality factor measurement using parallel plate resonator (PPR) [68] and dielectric resonator (DR) techniques. An HP8510C

microwave network analyzer is used to source transverse electromagnetic modes and then measure S21 vector values. These values are fit to a circle in the Smith chart to infer the quality factor. The distance between coupling loops and sample is adjusted to be weakly coupled so that the unloaded Q can be determined to better than a few percent. For each measurement, a PPR or DR is then loaded into a 2.03 cm × 0.61 cm × 1.52 cm gold-plated copper cavity which is affixed to the end of a cryogenic dipping probe. This probe is inserted into either a helium dewar for 4 K measurements without a field or in a cryostat (PPMS, Model 6000, Quantum Design, San Diego, CA) for temperatures as low as 2 K and magnetic fields as high as 9 Tesla.

The PPR technique uses two superconducting films of $YBa_2Cu_3O_{7-\delta}$ on 10 mm × 10 mm buffered sapphire substrates to form the parallel plates with a BZT-based sample as the interlayer dielectric. For our measurements, the interlayer dielectric is made sufficiently thick (i.e. 0.5 mm) so that the dielectric losses dominate. To validate this supposition, we measured the Q of a resonator to be 156,000 at 7 GHz and 4.2 K using ultra-low-loss phosphorous-doped ($4.5\times10^{15}/cm^3$) single-crystal Si as an interlayer. This sets a conservative lower bound for the Q associated with "parasitic" non-dielectric losses, since the near field and radiation losses for the significantly smaller dielectric constant material Si would be larger than those of BZT ($\varepsilon_r\approx30$) and the losses from superconductor surface resistance would be similar in magnitude. From this, we estimate that our Q measurements using the PPR technique are accurate to 10% or better.

DR measurements are made using 8.5 mm × 6.5 mm × 2 mm rectangular resonators, and also gave high Q values indicating that radiation and near field losses for this configuration also do not significantly affect the measurement result.

EPR studies were performed at the EPR Facility of Arizona State University. Continuous wave (CW) EPR spectra were recorded at liquid helium temperatures using a Bruker ELEXSYS E580 continuous wave X-band spectrometer (Bruker, Silberstreifen, Germany) equipped with an Oxford Model 900 EPL liquid helium cryostat (Oxford Instruments, Oxfordshire, UK). The magnetic field modulation frequency was 100 kHz, the amplitude was 1 mT, the microwave power was 1 mW, the microwave frequency was 9.42 GHz and the sweep time was 168 seconds. Pulsed X-band (9.7 GHz) EPR measurements were performed at 4 K using a Bruker ELEXSYS E580 FT−EPR X-band spectrometer equipped with an Oxford flow-cryostat CF 935 and a dielectric ring resonator (ER 4118X-MD5). Field-swept electron-spin-echo (ESE) detected EPR spectra were recorded using the two-pulse echo sequence ($\pi/2-\tau-\pi-\tau-$echo). Microwave pulses of 8 ns ($\pi/2$) and 16 ns (π) and τ = 140 ns were used. The spin-lattice relaxation time (T_1) was obtained from inversion recovery experiments. The phase-memory time (T_2*) was measured by the Hahn echo decay method.

CW EPR spectra were simulated using EasySpin (v 4.0.0), a computational package developed by Stoll and Schweiger [69]. The spectra of lightly to moderately doped samples were modeled considering two different single Ni^{2+} ion (S = 1) species; whereas those of heavily doped samples were modeled

considering only a spin-system with S = 2. The fitting parameters were the following: the three g values, g_x, g_y and g_z, the linewidth, ΔB, and the zero-field splitting parameters, D and E. The fitting procedures used in this work are similar to those previously described by Flores and coworkers [70].

The chemical compositions and trace amounts of impurities are inferred from Secondary Ion Mass Spectroscopy (SIMS) and Particle induced X-ray emission (PIXE). SIMS data collected using a Cameca IMS 6f SIMS system, and analyzed to infer the concentration of impurities using the first ionization potential of elements and their isotope abundance. PIXE was measured using proton beam at both energy levels of 1.72 MeV and 2.7 MeV. GUPIX program was used to simulate the x-ray spectrum to infer the chemical composition.

4.4 Microwave loss mechanism at cryogenic temperatures in $Ba(Zn_{1/3}Ta_{2/3})O_3$

The quality factor (Q), and the corresponding loss tangent, of samples measured at 4 K are found to strongly depend on the concentration of Mn and Ni dopants, i.e. transition metal impurities, as shown in Figure 4.3. Note that BZT with dopants such as Cd, Ga, Mg and Zr without unpaired d-electrons do not exhibit the same degradation in the Q when compared with the other samples. This data clearly shows that the presence of "magnetic" dopants, such as Ni and Mn, play a dominant role in the microwave loss mechanism in these transition-metal containing materials at 4.2 K.

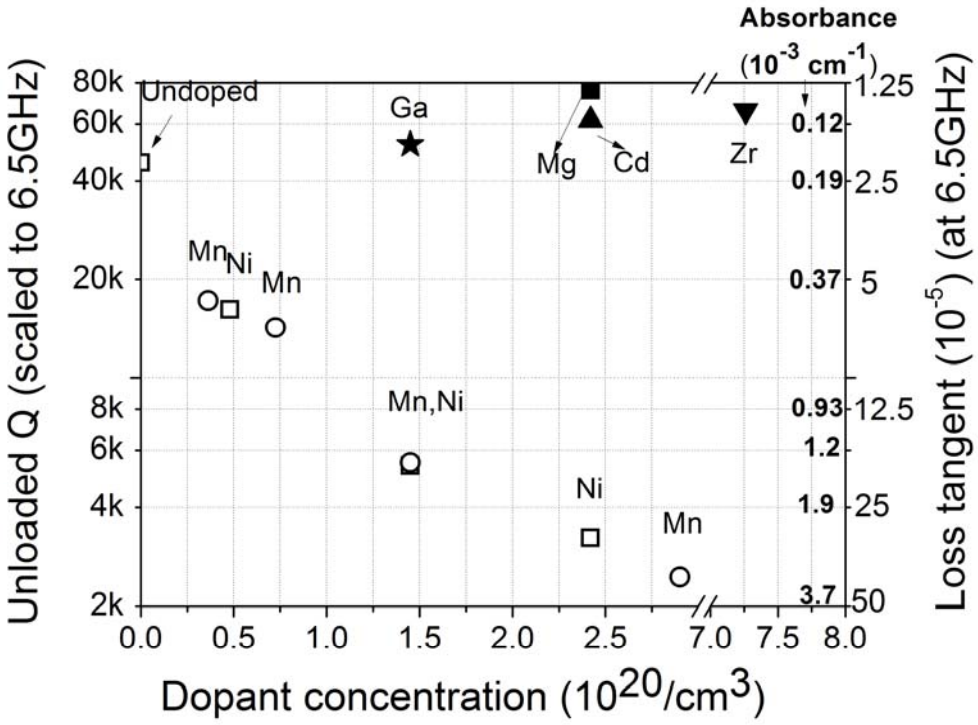

Figure 4.3 Unloaded Q factor and Loss tangent of BZT doped with various impurities measured with the parallel plate resonator configuration at 4.2 K and no applied magnetic field.

Fitting the low-field magnetic susceptibility data to the Curie-Weiss law indicates that all of the Ni-doped samples exhibit antiferromagnetic ordering at different temperatures (Fig. 4.4). It fits the reciprocal of magnetic susceptibility as a function of temperature. The cross point of the curve with x axis gives the Weiss temperature for anti-ferromagnetic transition and Curie temperature for ferromagnetic ordering. Table 4.1 summarizes the inferred Weiss temperature. The Weiss temperature is expected to be a close estimate of the Neel temperature in this work, as the large separation between Ni atoms in this work indicates that the spin interactions between atoms more distant than the nearest neighbors will

be inconsequentially small. A decreasing trend in the effective moment, μ_{eff} [= g_j $\sqrt{J(J+1)}$], in terms of the number of Bohr magnetrons (μ_B) per Ni atom is found for the larger Ni contents, as shown in Table 4.1. This is additional evidence of magnetic interactions between Ni at higher impurity concentrations.

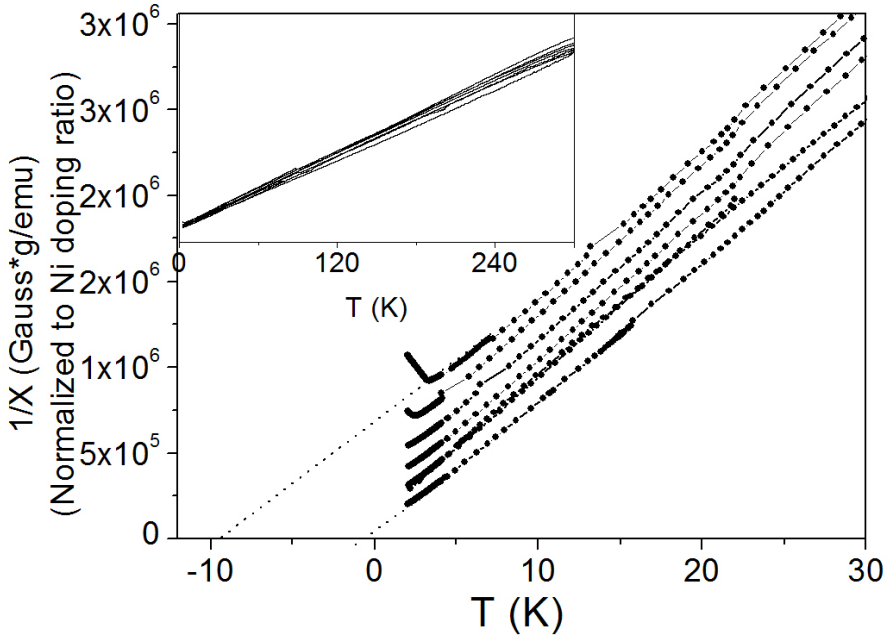

Figure 4.4 The inverse of magnetic susceptibility versus temperature. The Weiss temperature corresponds to the x-axis intercept for each of the curves. The curves from bottom to top correspond to 1%, 8%, 20%, 40%, 60%, 80% Ni doped BZT and BNT, respectively. Also note the upturn in the curves for the higher doped samples, a characteristic of the anti-ferromagnetic character.

Table 4.1. Magnetic properties of BZT doped with different Ni concentrations

			From temperature-dependent low-field magnetic susceptibility measurements (characteristic of all unpaired electrons)		From fitting Brillouin function to magnetic field-dependent susceptibility measurements (characteristic of clusters)	
Ni concentration (cm^{-3})	Fraction of Ni on Zn site	Average Ni separation (Å)	$\mu_{eff} = g_j \sqrt{J(J+1)}$ per Ni atom (μ_B)	Weiss Temperature (K)	J	M_s (emu/cm^3), $\{g_j J\}$
$5.2x10^{19}$	1%	27	3.11	0.5	0.65 (4K)	0.9,{1.9}
$4.1x10^{20}$	8%	13	2.97	1.4	1.5 (4.2K)	7.7, {2.1}
$1.0x10^{21}$	20%	9.9	3.03	1.8	2 (10K)	20, {2.2}
$2.1x10^{21}$	40%	7.9	2.96	3.3	3 (15K)	40, {2.2}
$3.1x10^{21}$	60%	6.9	2.97	4.6	4 (20K)	64, {2.4}
$4.1x10^{21}$	80%	6.2	2.94	6.4	10 (20K)	87, {2.4}

Figure 4.5 presents the quality factor of the resonators and the inferred loss tangent and absorbance for the materials at 4.2 K. As can be readily observed, the loss tangent of the Ni doped samples depends strongly on magnetic field for samples with 8% and greater Ni content. This indicates that loss is related to the spin degree of freedom in these samples. Phonons do not have a net charge or contain a magnetic moment and would thus not be expected to exhibit significant magnetic field dependence [46].

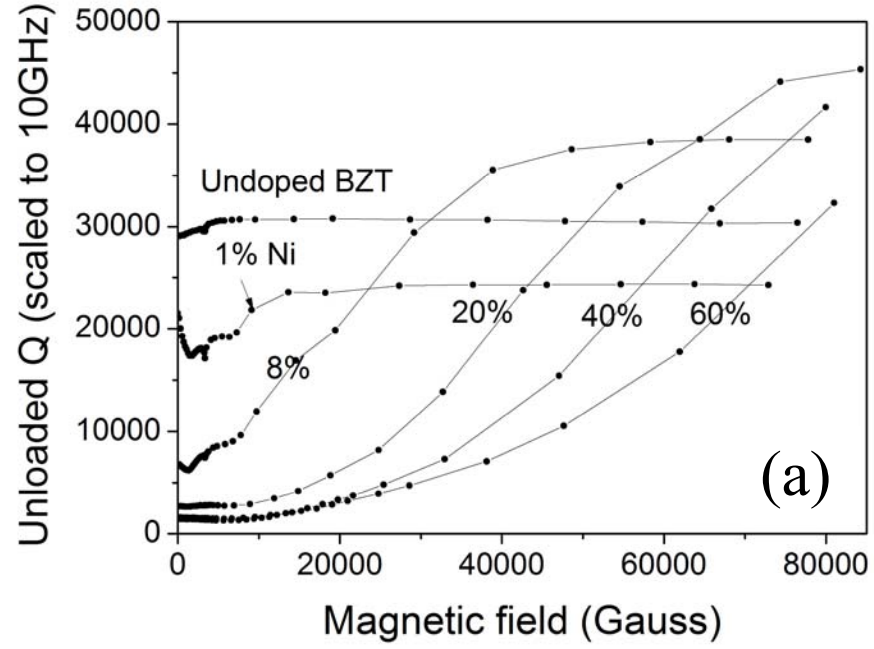
Unloaded Q (scaled to 10GHz)
Magnetic field (Gauss)
Undoped BZT
1% Ni
8%
20%
40%
60%
(a)

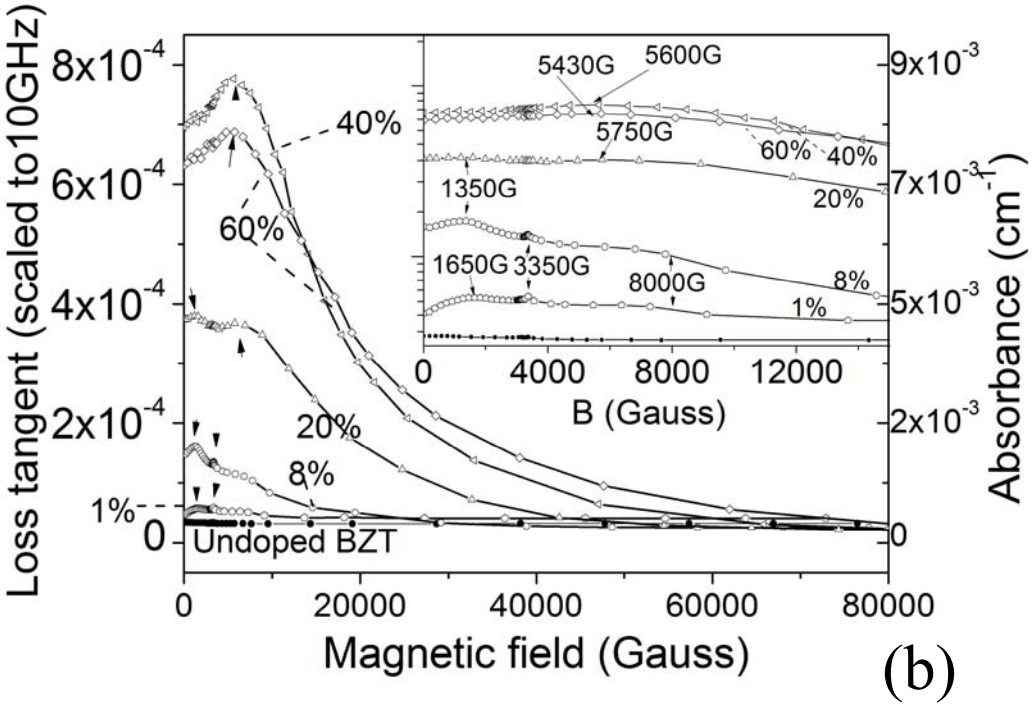
Loss tangent (scaled to10GHz)
Absorbance (cm-1)
Magnetic field (Gauss)
B (Gauss)
Undoped BZT
1%
8%
20%
40%
60%
5430G
5600G
5750G
1350G
1650G
3350G
8000G
(b)

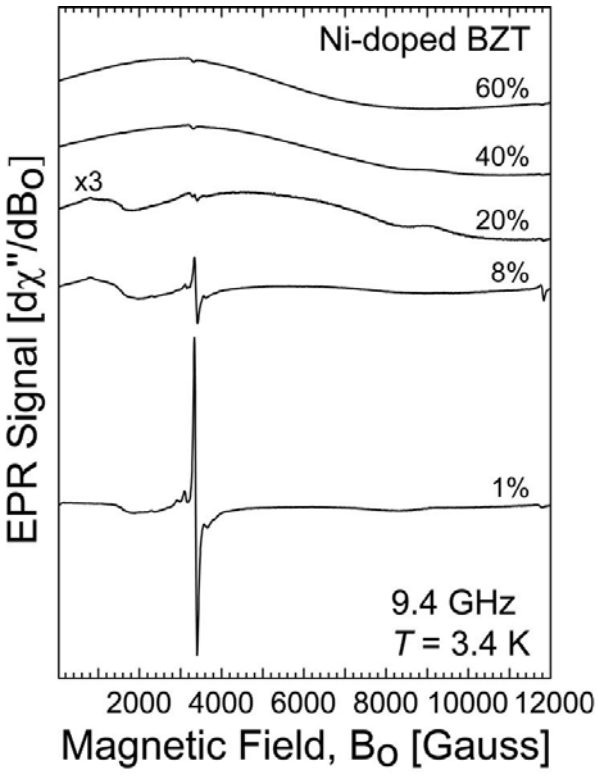

(c)

Figure 4.5. (a) Measured Q and (b) inferred loss tangent and absorbance of Ni-doped ceramic BZT at 4.2 K measured using the dielectric resonator configuration. The inset is an expanded view at low fields. Arrows point at EPR resonant absorption peak maxima. For comparison, (c) illustrates conventional CW EPR spectra (derivative of absorbance) of the ceramic (polycrystalline) samples measured using a Bruker EPR spectrometer.

The high Qs obtained enhance our ability to measure the loss tangent accurately and thus detect trace levels of absorption, including that from EPR [71,72]. EPR signals were detected at several magnetic fields; these can readily be observed as wide dips (peaks) in the Q (loss tangent). For instance, peaks at 1350, 1650, 3350 and 8000 G were observed for the 1% and 8% samples in Figures

4.5(a) and (b). This is substantiated by CW EPR measurements (first-derivative) with smaller steps in magnetic field taken with a conventional EPR spectrometer (see Experimental methods), Figure 4.5(c). Integration of the EPR derivative spectra produces results that are in agreement with the DR loss tangent measurements. The signals present in the EPR spectra were modeled using spectral simulations [73]. Two main Ni^{2+} (d^8, S = 1) species were identified in the 1% and 8% samples (see Supporting Information, Figure A.1). One species, characterized by a broad signal centered at ~8000G, was fit with an isotropic g value of 2.20 and Zero Field Splitting (ZFS) parameters, D and E, of 64.9 and 0 GHz, respectively. The broadening of this signal is due to dipolar spin-spin interactions. The second species presents signals at low magnetic field (~1000 G) that were fit using 1.95, 2.39, 2.16, 12.5 and 4.16 GHz for g_x, g_y, g_z, D and E, respectively. Both species correspond to a substitutional Ni^{2+} in an octahedral crystal/ligand field; with no rhombic distortion (E/D = 0) for the first one and maximum rhombic distortion (E/D = ⅓) for the second one [74]. The EPR spectra of the 1% and 8% samples also show signals centered at 3370 G (g = 2.00). The large intensity sharp feature was simulated using a S = ½ species with g = 2.00 and was tentatively attributed to free carriers presumably in local isolated regions (since the samples do not exhibit a measureable DC conductivity). The nearby features with smaller intensity were simulated considering a S = 1 species with isotropic g = 2.00, D = 1.3 GHz and E = 0 GHz. They were not assigned to Ni^{2+} since the value of g does not match that of Ni^{2+} (typically ~2.20).

Some aspects of the Ni^{2+} EPR signals change markedly as the doping concentration increases, while others do not. The spectral features from the low magnetic field species are not significantly altered, except for the amplitude, with the increase in Ni concentration. Such behavior shows that this species corresponds to isolated Ni^{2+} ions, which are not present in samples with 40% Ni and higher doping. In our lightly doped samples, the low field EPR peak from isolated Ni species with the maximum rhombic distortion ($^{E}/_{D} = ⅓$) extends down to zero applied field and dominates the loss there. Resonant loss from paramagnetic centers has been proposed to play a significant and often dominant role at reduced temperatures in ultra-low loss crystalline materials, including sapphire [49].

In contrast, the features of the broad signal specie change with doping concentration. Its resonance field position decreases and its line width increases with increasing Ni concentration (see Supporting Information, Table A.1). The broad signal completely dominates the EPR spectra of samples with Ni concentration above 20%. Its spectra can be simulated with an S = 2 spin system and an enhanced value of *D*. Although, exchange interactions were not used in the simulations due to the large broadening; they can also be involved in the spectral changes. Thus, the spectral changes induced by the increase in Ni concentration are associated with the formation of clusters, in which the exchange interactions between Ni^{2+} ions are orders of magnitude larger than dipolar interactions. Thus, in our heavily doped samples, the dominant species are clusters of Ni^{2+} ions.

In the following paragraph, we describe the properties of a resonant spin process in which the 3d electron spins of Ni and Mn clusters are coupled through an exchange interaction to produce a "super spin". Then we show that the magnetic field-dependence of our data is consistent with this mechanism. Gesmundo and the group [75] have shown that transition metal clusters act as a single spin when the exchange energy J $s_1 \cdot s_2$ is greater than the Zeeman interaction $g\beta H$. The total spin quantum number is a sum of the spins, $S=s_1+s_2+s_3+\ldots.+s_n$ and can take on integral values from 0 to S. [75] The energy of the levels follows a Lande ladder with magnitude S(S+1)J [i.e. 0, 2J, 6J, 12J, 20J, 30J, 42J, …] and are populated according to Boltzmann statistics. The dipole-dipole interaction between the spins of these clusters results in broadening of the level as a result of the number of neighbors statistically increase as the square of the distance and the interaction decreases as the inverse cube [58].

Gesmundo and Rossi showed that in Ni-alloyed with MgO, the "super spin" clusters were coupled for Ni atoms at distances of ~8 Å and less (i.e. Ni-doping levels of $2 \times 10^{21}/cm^3$). It is interesting that the average Ni separation in our 40% Ni sample is on the order of 8 Å and the 4.2 K loss drops most sharply at large magnetic fields for this and higher Ni concentration samples, presumably from decoupling when the Zeeman energy dominates over the exchange energy. The Qs in moderate to high transition-metal doped BZT exposed to large fields are as high and even higher than obtained otherwise suggests that these materials could potentially be optimized to realize even higher levels of performance under these conditions.

Note that the undoped and 1% doped Ni samples do not show a strong magnetic field dependence. For samples with Ni concentrations below $5\times10^{19}/cm^3$, with average separations of 27 Å, as found in our 1% and 8% samples, Gesmundo and Rossi's work suggests that the Ni present should act as isolated ions. This hypothesis has been confirmed in our EPR experiments (see above). Now, we can attribute the loss in samples with higher concentrations to be dominated by increasing broadened lines resulting from peaks associated with the "super spin" clusters.

To give a more direct estimate of the average number of transition metal impurities involved in the clusters for each Ni-doped sample, field-dependent magnetic susceptibility data were fit to the J of the Brillouin function. The results are summarized in Table 4.1. Fits of our data to the J of the Brillion function are shown below, giving insight into the effective number of centers involved in the clusters. The trend in the fit of the Brillion junction is clear with a value a little less than 1 for the 1% sample , 2 for 20%, 3 for 40%, 4 for 60%, and 10 for 80%. The value inferred for 100% Ni (i.e. $Ba(Ni_{1/3}Ta_{2/3})O_3$) can be fit with the Langevin function, indicating that all of the cluster is completely coupled (i.e. $Z=\infty$). Isolated Ni^{2+} atoms are in the d^8 state and have a spin state equal to 1 and a L of 0.4 because of spin orbit splitting. This data gives a first approximation to the number of ions in a typical cluster, but a more accurate model is needed that can take into account the exchange and dipolar interactions in this random network of Ni ions.

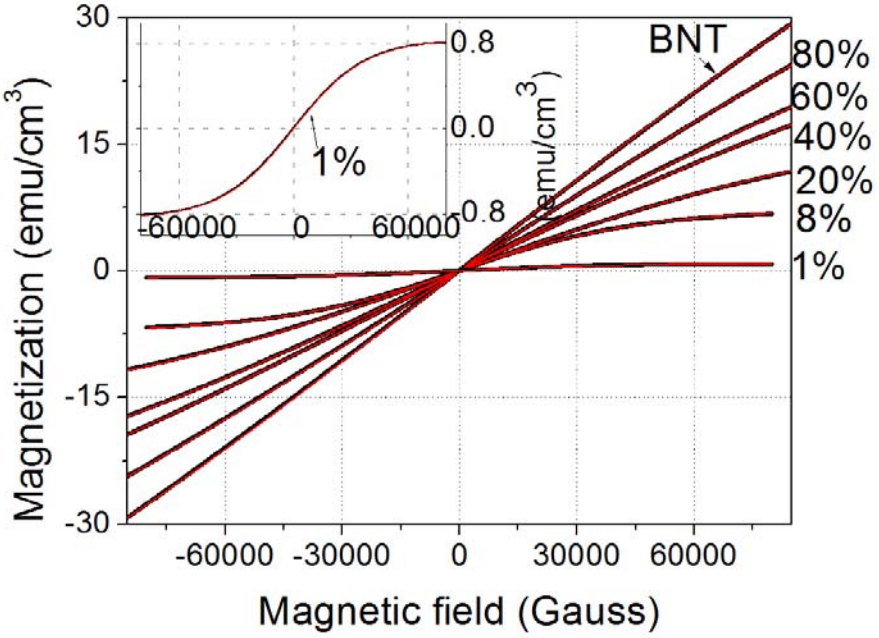

Figure 4.6 Fit of Brillion function (red) to measurements of the magnetic field dependent magnetic moment (black) of Ni-doped $Ba(Zn_{1/3}Ta_{2/3})O_3$

Isolated Ni^{2+} atoms are in the d^8 state and have a spin state equal to 1 and an L typically ~ 0.4 because of spin orbit splitting, resulting in a J of ~1.4. The trend in the fit of the Brillouin junction in Table 4.1 is clear with a J a little less than 1 for the 1% Ni-doped sample, 1.5 for 8%, 2 for 20%, 3 for 40%, 4 for 60%, and 10 for 80%. It is not clear why the 1% Ni sample has such a small value, although the curve fitting results still gives a "good" first approximation to the trend in the number of ions in an "average" cluster. A statistical model that includes the exchange and dipolar interactions in this random network of Ni ions with varying sized clusters is needed to more accurately determine the distribution of Js in coupled clusters. This data suggests that exchange coupling of 3d electrons into

higher spin clusters occurs in samples doped with 8% and larger Ni content- the exact same samples that show the marked increase in Q and corresponding drop in the loss tangent at high magnetic fields.

Furthermore, the field-swept ESE detected EPR spectra showed also a peak in absorption at low magnetic fields, down to near zero applied magnetic field, for the 1%, 8% and 20% Ni doped samples at 4 K (see Supporting Information, Figure A.1). Determinations of the spin-lattice relaxation time (T_1) and the phase-memory time (T_2*) in this broad low-field peak for the respective samples indicated that the peak belongs to a fast-relaxing species and suggests that the pulsed spectra are all inhomogeneously broadened. The times measured at the lowest observed field (20-50 G) range from 1 to 5 μs for T_1 and 90 to 650 ns for T_2*. The observation of an electron spin Hahn echo within the low field peak, which extends from hundreds of Gauss down to zero field unquestionably demonstrates that the absorption process involves localized electron spin flips (i.e. EPR transitions) and rules out the possibility of absorption by spin-polarized transport over an intermediate barrier or by tunneling [as suggested by Reference 46] or by the non-resonant spin excitation process which results in low magnetic field absorption peak over an energy width of J/ħ, as described by Bleaney and Ingram [57,58]. Spin polarized transport, free carriers and electric dipole precessions would also not be expected to exhibit the magnetic field dependence on loss tangent observed in our study.

Pulsed EPR absorption measurements were carried out at low fields using a convention Bruker spectrometer. This instrument is better optimized to measure

the absorption spectrum with finer resolution as a function of fields and can deliver pulsed excitations while monitoring the time dependence, although it is much more challenging to obtain accurate quantitative numbers for the loss tangent. A large, wide peak in absorption at low fields was also observed with these measurements, as shown below. Measurements of the spin-spin lifetime (T2) and spin-lattice (T1) in this broad low-field peak indicated that the lifetime is longest at low temperature and its linewidth is inhomogeneously broadened. The lifetimes are presented in a table below. The observation of a spin echo for both 90^o T2 and 180^o T1 measurement pulses unquestionably proves that the absorption process involves localized EPR spin flips and rules out the possibility of absorption by spin-polarized transport over an intermediate barrier or by tunneling [48] or by the non-resonant spin excitation process which results in low magnetic field absorption peak over an energy width of J/ħ, as described by Bleaney and Ingram.[43]

Table 4.2 Spin-lattice and Spin-Spin relaxation life time of BZT with different dopants

	T1 (μs)		T2 (ns)	
0.75% Mn 4K	4.641 (B=50G)	1.400 (B=3670G)	622 (B=50G)	160 (B=3670G)
0.75% Mn 10K	No signal	1.436 (B=3670G)	514 (B=50G)	147 (B=3670G)
0.75% Mn 20K	1.916 (B=50G)	1.401 (B=3670G)	249 (B=50G)	143 (B=3670G)
1%Ni BZT 4K	5.131 (B=50G)	3.503 (B=3452G)	653 (B=50G)	280 (B=3452G)

BZT 2900 4K	1.507 (B=250G)	2.147 (B=3460G)	89 (B=250G)	468 (B=3460G)
BZT 2900 8K	1.156 (B=250G)	2.598 (B=3460G)	65 (B=250G)	306 (B=3460G)
8733A 4K	2.496 (B=60G)	2.972 (B=3328G)	459 (B=60G)	244 (B=3328G)
8733C 4K	No	3.397 (B=3326G)	No	566 (B=3326G)
8733C 4K	No	3.325 (B=3964G)	No	512 (B=3964G)
8733D 4K	1.156 (B=60G)	1.816 (B=3328G)	72 (B=60G)	346 (B=3328G)
BNT 4K	No	2.912 (B=3349G)	No	517 (B=3349G)
BNT 4K		2.387 (B=3707G)		379 (B=3707G)

4.5 Microwave loss mechanism at cryogenic temperatures in commercial dielectric materials

In the last few decades, there has been a very successful effort to develop inexpensive temperature-compensated low-loss and high-dielectric-constant microwave ceramics for advanced communication and radar systems [76]. Higher dielectric constant, ε, facilitates smaller device sizes. Lower loss tangents ($\tan\delta$) produce devices with high quality factors (Q) in resonators and oscillators and lower insertion loss and sharper skirts in filters. Zero or near-zero temperature coefficients of resonance frequency (τ_F), allow the designer to produce systems whose frequency does not drift with temperature.

This work investigates several microwave dielectric materials which are widely used by industry, including

- Ni-and Zr-alloyed $Ba(Zn_{1/3}Ta_{2/3})O_3$ ($\tan\delta \approx 2\times10^{-5}$ scaled to 2GHz,

ε_r~30),

- Co-alloyed $Ba(Zn_{1/3}Nb_{2/3})O_3$ ($\tan\delta \approx 3\times10^{-5}$ scaled to 2GHz, ε_r ~35),
- $ZrTiO_4$–$ZnNb_2O_6$ ($\tan\delta \approx 5\times10^{-5}$ scaled to 2GHz, ε_r ~43), and
- $BaTi_4O_9$-$BaZn_2Ti_4O_{11}$ ($\tan\delta \approx 4\times10^{-5}$ scaled to 2GHz, ε_r ~36).

The properties of commercial materials are optimized by adding certain dopants or solid solution alloy agents, including Ni, Zr, Co, Mn, Cu, etc [77,78,79,80]. These impurity elements can serve as sintering aids to enhance the manufacturability, crystal quality, density and ultimately the Q [77,78]. They can also act to increase the dielectric constant or adjust the τ_f to zero or near-zero [77,80].

Despite the widespread application of these materials, the physical mechanism of the loss mechanism is not fully understood and warrants further investigation. Optimized materials are insulating with minimal free carrier conduction [81,82]. The loss that is present in such materials has most often been attributed to anharmonic-phonons [83-87]. Impurity [88], extended defects [89] and surface states in pores [90] been experimentally-been correlated to an increase in the loss tangent and this has been attributed to the production of softer phonon modes with increased anharmonicity.

One strategy to investigate the fundamental mechanism of loss is to vary the temperature [91]. Recent reports have found a variety of behavior ranging from a strong increase to a significant drop in the loss tangent at low temperatures [92-96], although the mechanism for this has not been unambiguously identified. It is also appealing to consider using materials with very low loss at cryogenic

temperatures in practical communication and radar systems [97]. If these materials could be optimized for low temperature operation, they could potentially also positively impact quantum computing, photonic detector, amplifier and mixer circuitry, as the performance of these advanced electronics is often limited by ac losses and the associated noise [98,99].

In this work, we measure the loss tangent as a function of temperature using microwave resonators whose quality factors (Qs) are limited by dielectric loss. In order to investigate the role of electron paramagnetic resonance loss, we have also carried out magnetic field-dependent measurements. These results show conclusively that the dominant loss process at cryogenic temperatures is from resonant spin excitations of unpaired d-electrons within isolated transition metal atoms for small dopant concentrations and within exchange coupled transition-metal clusters for higher concentrations. We demonstrate that the microwave loss can be effectively reduced by operating at cryogenic temperature in materials which have no transition metal ions or both reducing temperature and applying a strong static magnetic field for those which contain paramagnetic ions. Our measurements also show that this mechanism does significantly contribute to room temperature loss, although it no longer dominates.

The temperature dependence of the microwave loss tangent from 4.2K to 300K is shown in Fig. 4.7 for $Ba(Zn_{1/3}Ta_{2/3})O_3$ samples made in our lab and in Fig. 4.8 for $Ba(Zn_{1/3}Ta_{2/3})O_3$ and a number of other commercial dielectric materials. In our earlier work [104], we quantitatively showed that the microwave

loss at 4.2 K scaled linearly with the concentration of Mn and Ni dopants, i.e. transition metal impurities with unpaired d-electrons. In contrast, $Ba(Zn_{1/3}Ta_{2/3})O_3$ with dopants such as Cd, Ga, Mg and Zr without unpaired d-electrons do not exhibit the loss when compared with the other samples. It is noteworthy that even a Group III element such as Ga in $Ba(Zn_{1/3}Ta_{2/3})O_3$ does not result in paramagnetic loss, presumably as a result of charge compensation.

In Fig. 4.7, we show the data in the whole temperature range for Ni doped $Ba(Zn_{1/3}Ta_{2/3})O_3$. As the temperature cools down from 300K to 4.2K, the microwave loss decreases at the beginning for all doping levels, presumably from a decrease in the phonon population and a very small (most likely an insignificant change) reduction in band conduction or hopping transport [81,82,83-87]. As the temperature cools down further, however, a significant increase of loss is observed in Ni doped samples, and the loss scales with Ni-doping concentration. The "turning point" (the temperature where loss tangent starts to increase) in the loss tangent curves varies with doping levels. They are ~20K, 60K and 160K for 8%, 20% and 40% Ni doped samples, respectively. Fig. 4.8 shows the temperature dependence of microwave loss in other commercial dielectric materials. A significant increase in loss is found in these materials as well, e.g. in Ni and Co doped $Ba(Zn_{1/3}Ta_{2/3})O_3$ and $Ba(Zn_{1/3}Nb_{2/3})O_3$. In $BaTi_4O_9$-$BaZn_2Ti_4O_{11}$ material, there is a small increase at very low temperatures. The "turning points" of loss are around 10K, 50K and 200K for $BaTi_4O_9$-$BaZn_2Ti_4O_{11}$, $Ba(Zn_{1/3}Ta_{2/3})O_3$ and $Ba(Zn_{1/3}Nb_{2/3})O_3$, respectively.

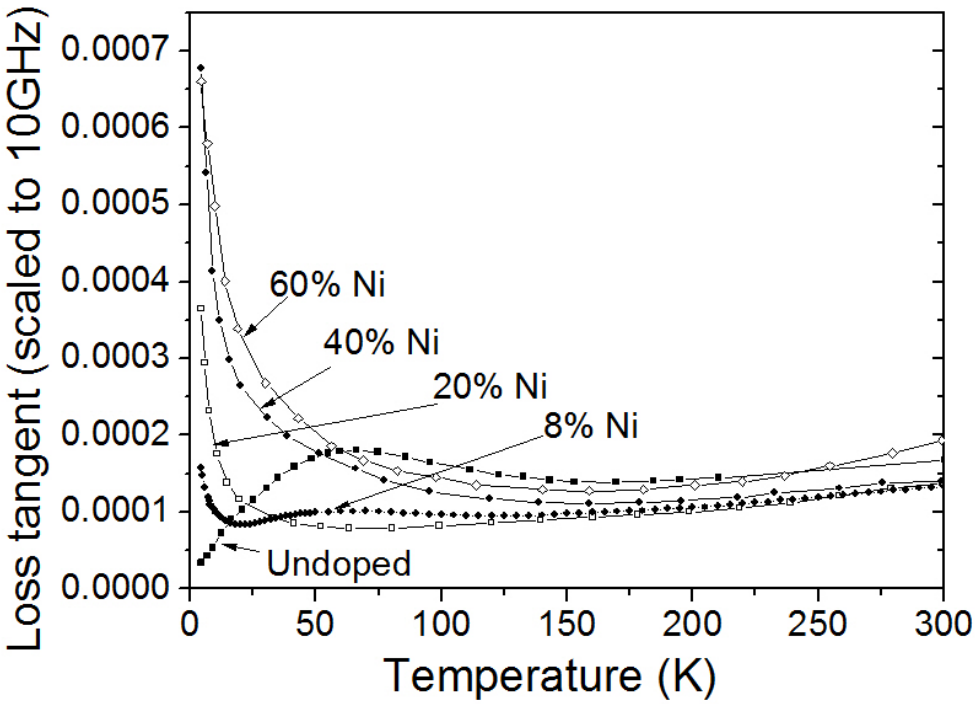

Figure 4.7. Microwave loss tangent of Ni doped $Ba(Zn_{1/3}Ta_{2/3})O_3$ as a function of temperature. The denoted Ni percentage refers to the fraction of Ni on the Zn site and ranges from 0 to 60% [i.e. $Ba(Zn_{1-x}Ni_x)_{1/3}Ta_{2/3})O_3$ where $0<x<0.6$].

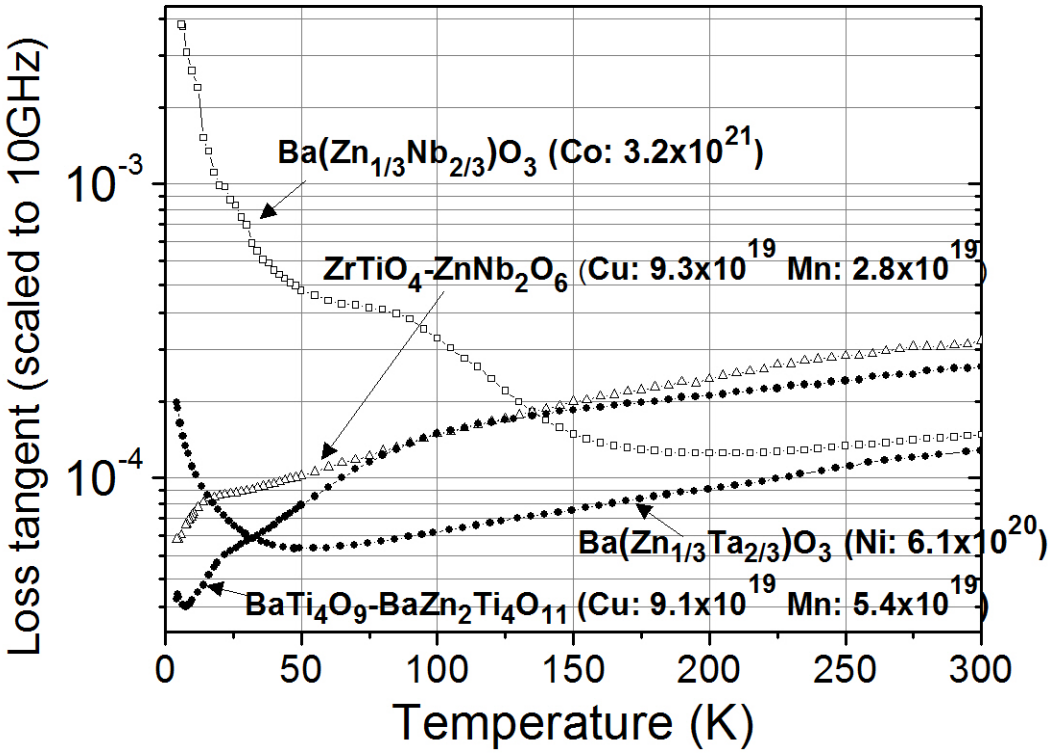

Figure 4.8. Temperature-dependence of microwave loss tangent of commercial dielectric materials containing different transition metal ions of various concentrations (in cm^{-3})

PIXE and SIMS measurements indicate that all samples have transition metal ions, although with a wide range of concentrations, as summarized in Table 4.3. Commercial $Ba(Zn_{1/3}Nb_{2/3})O_3$ and $Ba(Zn_{1/3}Ta_{2/3})O_3$ with relatively high concentration of transition metal Ni and Co ions have large microwave loss at cryogenic temperature, while $BaTi_4O_9$-$BaZn_2Ti_4O_{11}$ and $ZrTiO_4$-$ZnNb_2O_6$ which contain only trace amount of transition metal ions (i.e. Cu^{2+} and Mn^{4+}, etc.) have small microwave loss. This data shows that the presence of "magnetic" dopants, such as Ni, Co, Cu, Mn, and Fe, play a dominant role in the microwave loss

mechanism in these transition-metal containing materials at cryogenic temperatures.

Table 4.3 Concentration of transition metal elements in commercial dielectric materials

$ZrTiO_4$-$ZnNb_2O_6$		$BaTi_4O_9$-$BaZn_2Ti_4O_{11}$		$Ba(Zn_{1/3}Nb_{2/3})O_3$		$Ba(Zn_{1/3}Ta_{2/3})O_3$	
Impurity	cm^{-3}	Impurity	cm^{-3}	Impurity	cm^{-3}	Impurity	cm^{-3}
Cu	9.3×10^{19}	Cu	9.1×10^{19}	Co	3.2×10^{21}	Ni	6.1×10^{20}
Mn	2.8×10^{19}	Mn	5.4×10^{19}	Mn	4.2×10^{19}		
Fe	9.6×10^{18}	Fe	3.8×10^{18}	Fe	4.6×10^{18}		
Co	7.3×10^{17}	Co	6.5×10^{17}				
Cr	3.2×10^{17}	Cr	2.7×10^{17}				

Figure 4.9 presents the measured microwave loss (Fig.4.9 (a)) and unloaded Q factor (Fig.4.9 (b)) of commercial materials at 4.2 K as a function of a magnetic field up to 8 T. As can be readily observed, the microwave loss of all samples depends strongly on magnetic field. This indicates that loss is related to the spin degree of freedom in these samples. Phonons do not have a net charge or magnetic moment and would thus not be expected to exhibit significant magnetic field dependence [81].

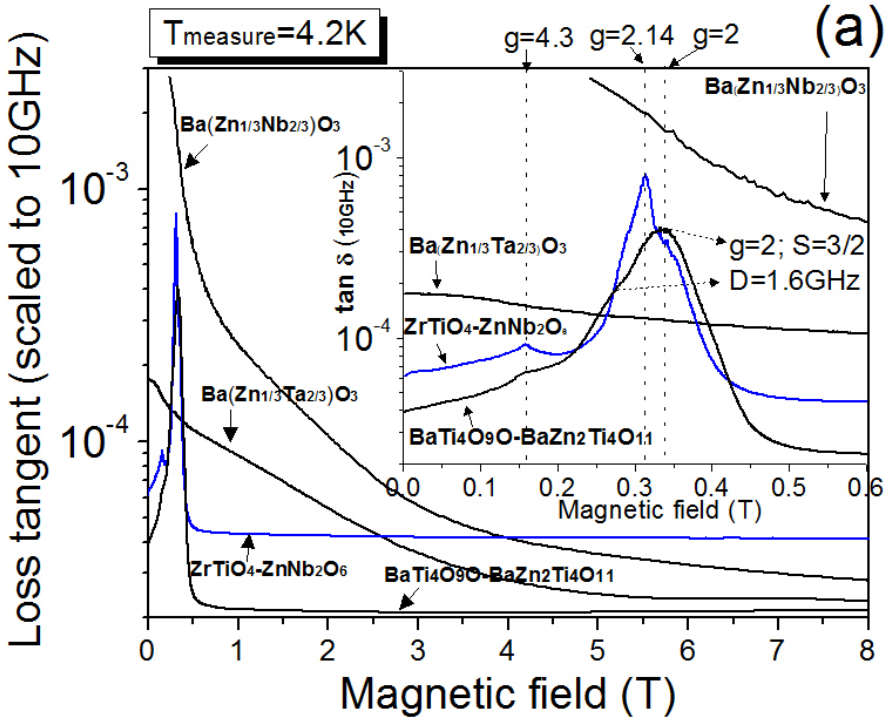
Tmeasure=4.2K
(a)
g=4.3
g=2.14
g=2
Ba(Zn1/3Nb2/3)O3
Ba(Zn1/3Ta2/3)O3
ZrTiO4-ZnNb2O6
BaTi4O9O-BaZn2Ti4O11
g=2; S=3/2
D=1.6GHz
tan δ (10GHz)
Loss tangent (scaled to 10GHz)
Magnetic field (T)

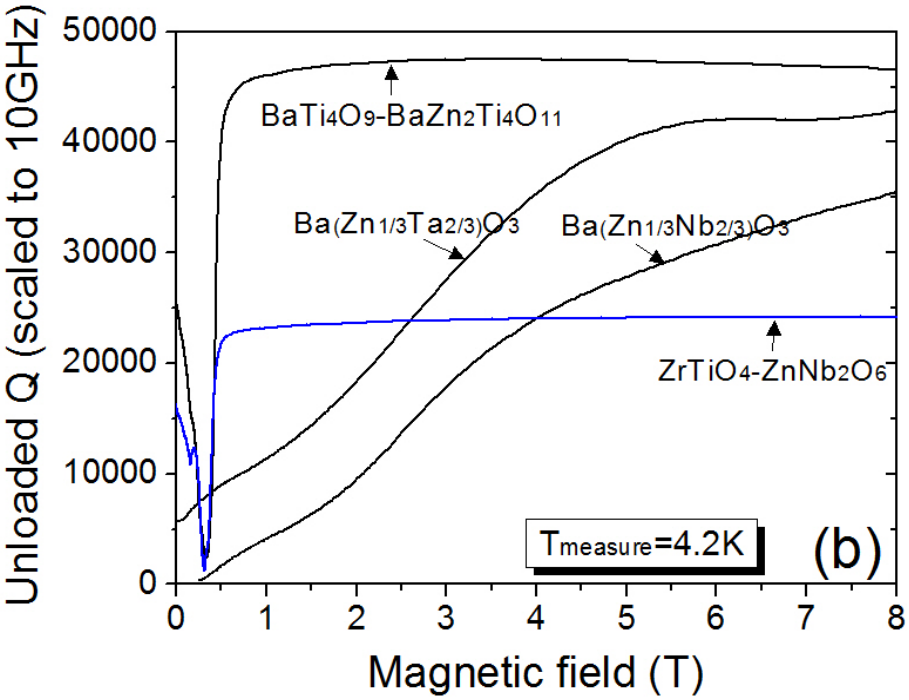
BaTi4O9-BaZn2Ti4O11
Ba(Zn1/3Ta2/3)O3
Ba(Zn1/3Nb2/3)O3
ZrTiO4-ZnNb2O6
Tmeasure=4.2K
(b)
Unloaded Q (scaled to 10GHz)
Magnetic field (T)

Figure 4.9. (a) Microwave loss tangent and (b) unloaded Q factor of commercial dielectric materials at 4.2K as a function of magnetic field. The insets are the same data in the low magnetic field range. The resonant frequencies, f_0, of the $ZrTiO_4$-$ZnNb_2O_6$, $BaTi_4O_9$-$BaZn_2Ti_4O_{11}$, $Ba(Zn_{1/3}Nb_{2/3})O_3$, and $Ba(Zn_{1/3}Ta_{2/3})O_3$ dielectric resonators are 8.09, 8.82, 8.61 and 9.25 GHz, respectively. In order to plot the data on the same scale, the applied magnetic fields have been scaled to 9.4 GHz by multiplying by 9.4 GHz/f_0. 9.4 GHz was chosen because it is the most commonly used frequency in commercial X-band EPR systems.

The high Qs obtained enhance our ability to measure the loss tangent accurately and thus detect trace levels of absorption, including that from Electron Paramagentic Resonance (EPR) [105,106]. EPR signals were detected at several magnetic fields; these can readily be observed as peaks (dips) in the loss tangent (Q) curves. For instance, commercial $ZrTiO_4$-$ZnNb_2O_6$ shows the species at g=2, g=2.14, g=2.3 and g=4.26. Illustrations of the fit of the experimental data containing electron paramagnetic resonances are provided in the supplemental materials. The resonance at g=2.14 is associated with the Cu^{2+} impurity and the one at g=2 is associated with Mn^{4+}. The physical nature of the g=2.3 peak is not clear, and could potentially also arise from Cu ions. The weak absorption at g=4.26 can be from some high spin species like Fe^{3+} or Co^{2+} ions. The $BaTi_4O_9$-$BaZn_2Ti_4O_{11}$ measurements show peaks at g=2 and g=4.3 which is similar to $ZrTiO_4$-$ZnNb_2O_6$. However, in that case the peaks are broader than those of $ZrTiO_4$-$ZnNb_2O_6$. The origin of this enhanced broadening in $BaTi_4O_9$-

$BaZn_2Ti_4O_{11}$ is presumably from the inhomogeneous dipolar interactions of the higher Mn concentration (in Table 4.3). Note that for $BaTi_4O_9$-$BaZn_2Ti_4O_{11}$, the left shoulder of the g=2 peak around 0.25 T is associated with zero field splitting (ZFS) constant D of 1.6 GHz with S=3/2 spin system, i.e. Mn^{4+} ions. The ZFS effect shifts its broader peak towards zero magnetic field, which dominates the increase of microwave loss for $BaTi_4O_9$-$BaZn_2Ti_4O_{11}$ below 10K without an applied field.

In contrast, the broader tangent peak that extends to zero applied field in heavily doped samples $Ba(Zn_{1/3}Nb_{2/3})O_3$ (Co) and $Ba(Zn_{1/3}Ta_{2/3})O_3$ (Ni) can be attributed to the formation of spin clusters, in which the exchange interactions between transition metal ions are orders of magnitude larger than dipolar interactions. These clusters can be treated as a single "super" spin, and have large ZFS D-values. In these clusters, the d-electrons are coupled through an exchange interaction to produce a "super spin" [107] with a total spin quantum number that is the sum of the spins, S=s1+s2+s3+…. +sn. The spin can take on integral values from 0 to S [107] with a Lande ladder energy S(S+1)J that follows Boltzmann statistics. The dipole-dipole interaction between the spins of these clusters dominates the broadening of the level as a result of the number of neighbors statistically increases as the square of the distance and the interaction decreases as the inverse cube [108].

The commercial $Ba(Zn_{1/3}Ta_{2/3})O_3$ material in this study has 12% Ni doping (relative to Zn concentration), which is similar to 8% Ni doped $Ba(Zn_{1/3}Ta_{2/3})O_3$ in our early study [104]. According to Gesmundo's work [107], the Ni ions form

exchange coupled clusters when their distance is less than ~8 Å. The average distance of Ni ions in the commercial $Ba(Zn_{1/3}Ta_{2/3})O_3$ is 12 Å. The commercial $Ba(Zn_{1/3}Ta_{2/3})O_3$ show a different peak position at near zero magnetic field compared to 8% Ni doped $Ba(Zn_{1/3}Ta_{2/3})O_3$. In 8% Ni doped $Ba(Zn_{1/3}Ta_{2/3})O_3$, it's around 0.1 T due to a D of 12.5 GHz and rhombic distortion for the S=1 species [104]. In contrast, the peak maxima is at zero field for the commercial $Ba(Zn_{1/3}Ta_{2/3})O_3$. This results from a higher D value associated with an expanded lattice constant as a result of the Zr-doping.

The magnetic field dependence of loss tangent for Co contained $Ba(Zn_{1/3}Nb_{2/3})O_3$ is similar to that of $Ba(Zn_{1/3}Ta_{2/3})O_3$. It also shows a strong and broadened absorption peak maximized at zero magnetic field. The average distance between Co^{2+} ions in the $Ba(Zn_{1/3}Nb_{2/3})O_3$ is 6.7 Å. According to ref. [109], Co^{2+} ions form exchange-coupled spin clusters when they are separated by less than 7 Å. Thus, in the $Ba(Zn_{1/3}Nb_{2/3})O_3$ material, the large microwave loss at 4.2K can be attributed to the effect of spin excitations in theses clusters. It is also worth noting that at 4.2K, the microwave loss at 8 T is about two orders of magnitude lower than that at zero applied fields. This shows that the microwave loss can be largely suppressed by aligning the spin by applying a static magnetic field.

The ability to tune and/or boost the performance with magnetic fields may have practical applications. The availability of high field rare earth permanent magnets and high field superconductor coils enable this possibility now. However, if materials can be developed that show similarly large changes at higher

temperatures and/or smaller magnetic fields, this could be used in a wide range of practical applications to tune the device and/or increase the performance.

The magnetic field dependence of the loss tangent has also been measured at room temperature (T=300K) and is shown in Fig. 4.10. At room temperature, the microwave loss has much weaker magnetic field dependence than that at 4.2 K, but it's still detectable. This indicates that spin excitations play a small, but measurable role, at room temperature. They all show the EPR peak around g=2.0 with the exception of the $Ba(Zn_{1/3}Ta_{2/3})O_3$ material which shows a near zero field peak. This is very similar to the observations at low temperature. The change of microwave loss with magnetic field in the $Ba(Zn_{1/3}Ta_{2/3})O_3$ and $Ba(Zn_{1/3}Nb_{2/3})O_3$ is larger and more gradual than that in $ZrTiO_4$-$ZnNb_2O_6$ and $BaTi_4O_9$-$BaZn_2Ti_4O_{11}$, which is consistent with the trends observed for isolated ions and spin clusters.

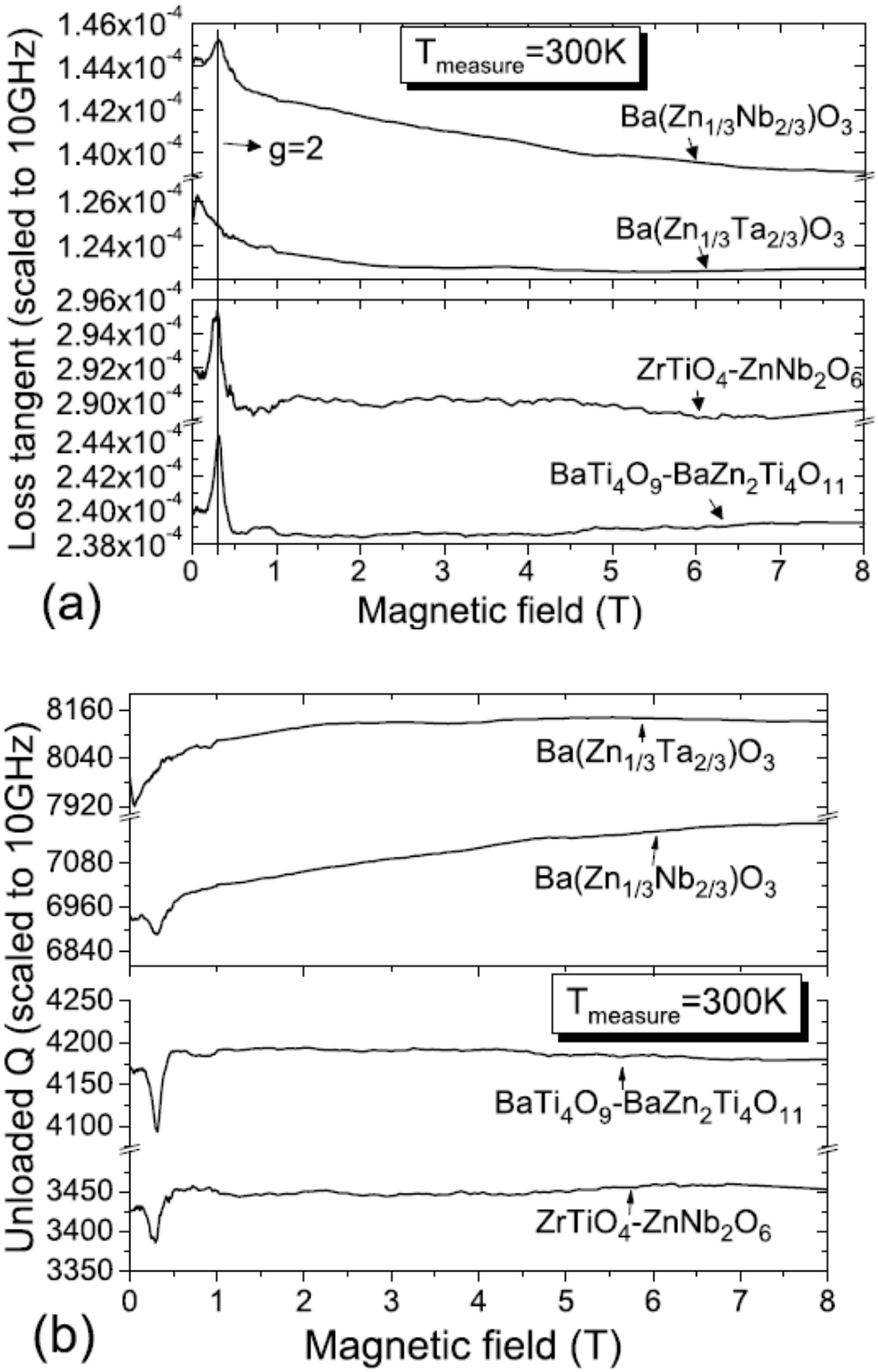

Figure 4.10 Magnetic-field dependence of (a) the microwave loss tangent and (b) Q factor for commercial dielectric materials at room temperature (300K)

We can infer the loss tangent from spin excitations by taking the difference of loss tangent between zero magnetic field and very high magnetic field (8 T) using the following relationship: $\tan\delta_{EPR} = \tan\delta(B= 0\ T) - \tan\delta(B= 8\ T)$. Table 4.4 lists the microwave loss due to EPR at both 4.2K and 300K. We can see that all the loss at 4.2K is larger than those at 300K. This can be attributed to the higher magnetic susceptibility and longer spin-spin, spin-lattice relaxation lifetime at lower temperatures.

Table 4.4 Microwave loss tangent scaled to 10 GHz that can be attributed to unpaired d-electron spin excitation in commercial dielectric ceramics

	$\tan\delta_{EPR}$ (4.2K)	$\tan\delta_{EPR}$ (300K)
$ZrTiO_4$-$ZnNb_2O_6$	2.04×10^{-5}	2.28×10^{-6}
$BaTi_4O_9$-$BaZn_2Ti_4O_{11}$	1.75×10^{-5}	5.16×10^{-7}
$Ba(Zn_{1/3}Nb_{2/3})O_3$	3.50×10^{-3}	5.01×10^{-6}
$Ba(Zn_{1/3}Ta_{2/3})O_3$	1.54×10^{-4}	2.17×10^{-6}

4.6 Conclusion

In conclusion, we measured the temperature and magnetic dependence of microwave loss in several lab-made and commercial dielectric materials. we have shown that microwave loss in transition-metal doped BZT at low temperature is

due to resonant spin excitations of unpaired d-electrons within isolated impurity atoms for small dopant concentrations and within exchange coupled clusters for higher concentrations. This low-temperature loss can be significantly reduced by applying static magnetic fields that preferentially align the spin system. Although this mechanism also contributes to room temperature loss, it no longer dominates. We hope that this work will motivate additional theoretical efforts to model the exchange and dipole interactions in such transition-metal doped compounds in order to gain an improved microscopic understanding of the relation between electron spin excitations and microwave loss.

Chapter 5

THE ROLE OF DEFECTS IN MICROWAVE LOSS PROCESS AT ROOM TEMPERATURE

5.1 Compositional, electrical, FTIR and Raman characterization of microwave dielectric

The detailed mechanism responsible for the influence of dopants on the tan δ at room temperature has not been completely resolved. We carried out a measurement of ceramic dielectric materials produced in a commercial production line with a range of quality factors, depending on the origin of the starting batch of powder materials. We compare these materials with undoped BZT made in our lab. The Ni and Zr doped BZT are quoted as 8733 series as an earlier publication of our lab group [9]. Four batches of 8733 series materials have a wide range of Q factors. They are then quoted as 8733A, B, C and D in order of descending Qs. The Qs for them are 43000, 31000, 16600 and 9930 scaled to 2GHz, respectively.

We found that the total concentration of contaminants scale with the loss tangent for these samples, as shown in Table 5.1. The total concentration increases from 0.405 mol% for good material 8733A to 2.636 mol% for bad material 8733D. Among the impurities, B^{3+}, Na^{+}, and Fe^{3+} can act as acceptors, which would be expected to be compensated by oxygen vacancies. The presence of these defects could be involved in the degradation of the Q factors.

Table 5.1 Impurities in commercial BZT 8733 materials with a wide rage of Qs induced from SIMS data

mol %	8733A Q=43000 @2GHz	8733B Q=31000 @2GHz	8733C Q=16600@2G	8733D Q=9930@2G
B	0	0	0.143	0.094
Na	0.032	0.018	0.109	0.134
Si	0.132	0.214	0.526	1.598
Ca	0.158	0.183	0.277	0.745
Ti	0.083	0.074	0.035	0.041
Fe	0	0.036	0.019	0.024
Total	0.405	0.525	1.109	2.636

Fig. 5.1 shows the measured DC conductivity of 8733A, B, C and D samples measured at elevated temperatures. Thermally activated carrier conduction was observed with an activation energy of ~0.6eV. The conductivity is found to systematically increase with increasing loss tangents. The carriers presumably result from doping by the point defects which also act as color centers in the lattice. Our earlier research [9] found that from 8733A to D, the color of the samples change from light yellow to dark brown. Point defect color centers were found to be responsible for the continuous background of absorption the visible range whose concentration increased systematically from A, to B, to C, to D. Further work is needed to identify the physical nature of the point defects or point defect compexes responsible for the electrical and optical data.

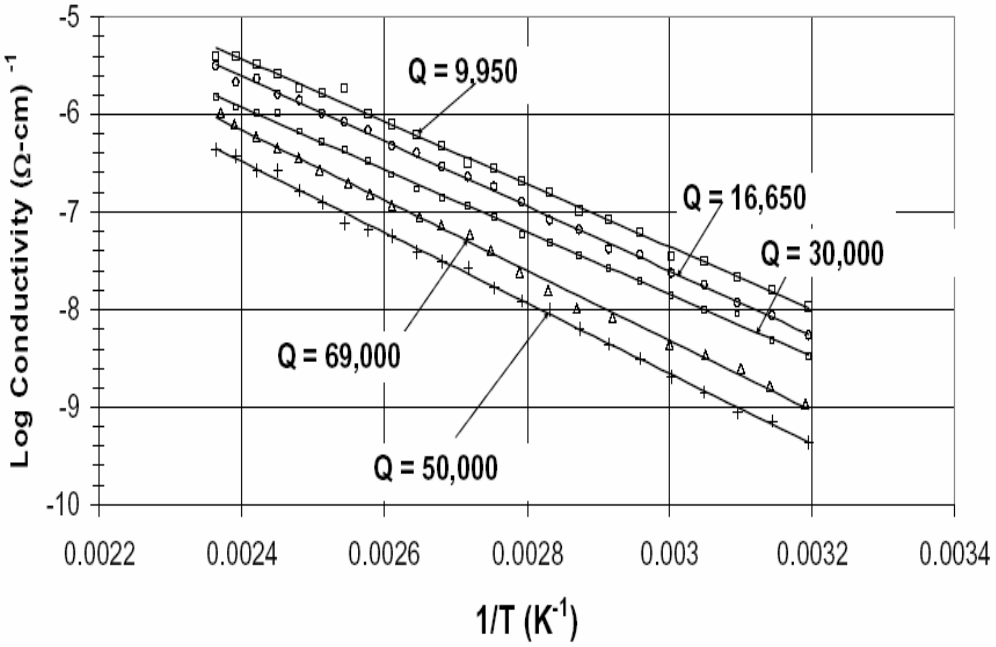

Figure 5.1 Temperature dependence of conductivity of undoped and Ni and Zr-doped $Ba(Zn_{1/3}Ta_{2/3})O_3$ bulk samples at 500 V/cm.

The harmonic and anharmonic phonon properties can be directly measured using Fourier transform infrared (FTIR) and Raman spectroscopy in the far-IR spectral range. The ordered hexagonal BZT system totally has 4 A1g vibration modes, 5 Eg modes, 1 A2g mode, 7 A2u modes, 9 Eu modes. Among them, A2g and A1u modes are infrared silent modes. Eg and A1g modes are Raman active and silent in IR spectra. The A2u and Eu modes are IR active and Raman silent. The heavy Ba atoms contribute their spectral weight in the lower band and the light Oxygen atoms in the high energy band. Figure 5.2 shows the Raman spectra for undoped BZT and 8733 ABCD materials. Fig. 5.3 (a) and (b) shows the FTIR results. Fig. 5.3 (a) shows the reflectance of ceramic samples in the Far-IR range,

and (b) shows the induced imaginary part (ε") of dielectric constant calculated by Kramer-Kronig transformation (KKT). ε" gives direct information about optical absorption and loss tangent. The peak width of ε" is the dampening constant which related the anharmonicity of phonons. From the Raman and Far-IR data, we can see a systematic trend that high loss materials have higher far IR absorption spectra peak widths at 138 cm^{-1} and Raman spectra at 135, 400 and 450 cm^{-1} (Figure 5.2, 5.3). This wider width is associated with higher optical phonon mode nanharmonicity .

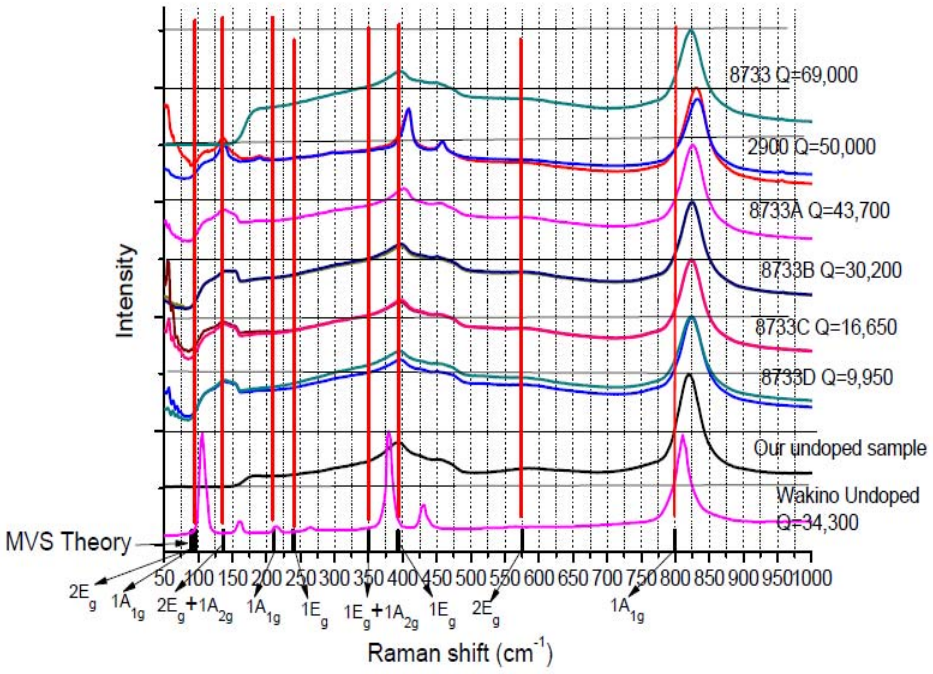

Figure 5.2 Raman spectroscopy of the series of BZT samples. Also included are the published measurements on BZT samples by Wakino and ab-initio density functional predictions that we have performed at ASU, in collaboration with Mark van Schilfgaarde. Plots are aligned by the order of quality factors scaled to 2 GHz.

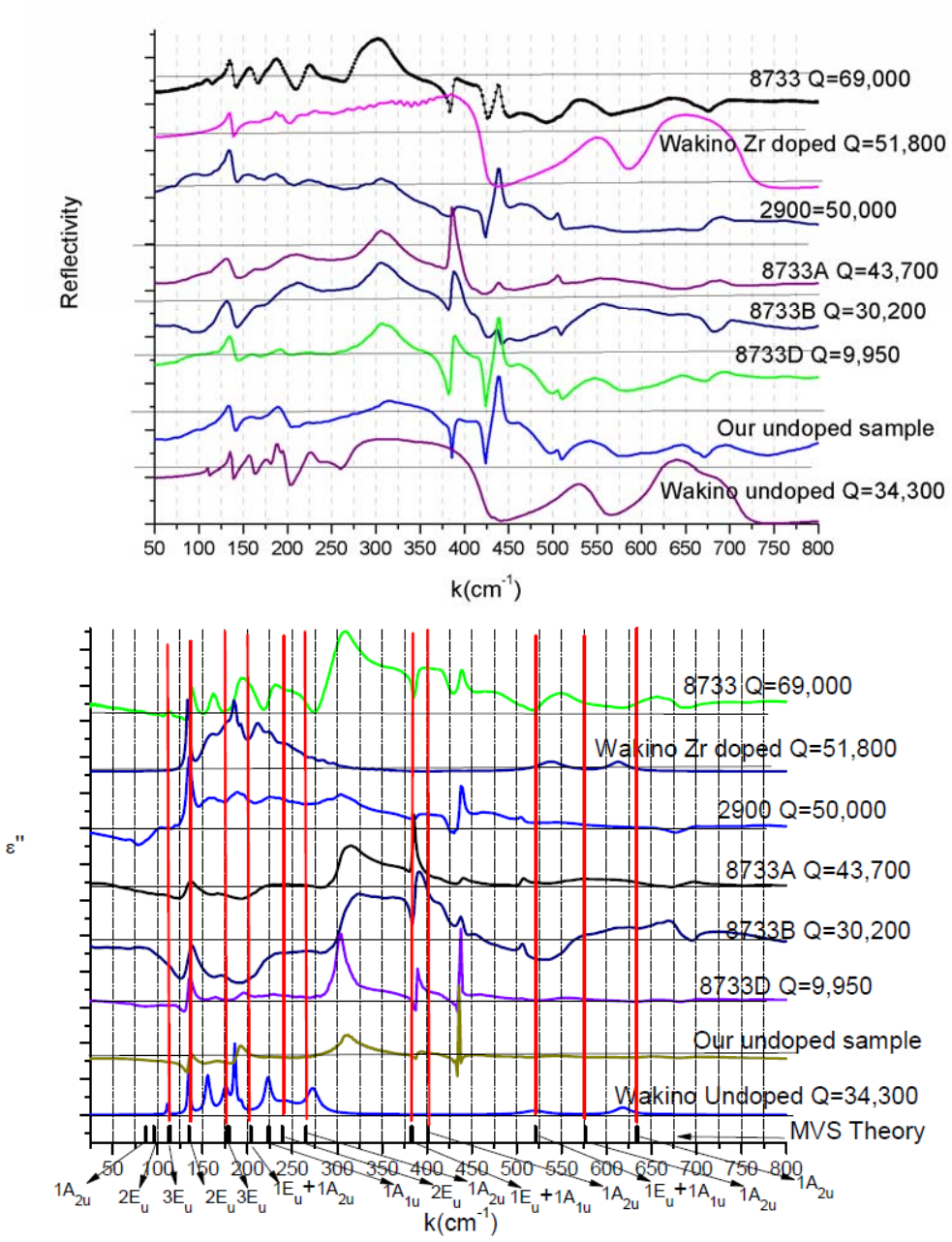

Figure 5.3 (a) Far Infrared reflectance and (b) induced imaginary part of dielectric constant of the series of BZT samples. Samples are listed in descending quality factors that was scaled to 2 GHz.

Chapter 6

SUMMARY AND FUTURE WORK

In this thesis, we studied the properties of high performance microwave dielectric ceramics.

We use both parallel plate resonator (PPR) and dielectric resonator (DR) structures to accurately determine the loss tangent of small dielectric samples over a range of temperatures and magnetic fields. This facilitates quantitative Electron Paramagnetic Resonance (EPR) measurements of solid samples. The techniques that we use have a sensitivity of better than 5×10^{-7} at 6.5 GHz for measurement of loss tangent of materials with a dielectric constant, ε_r, of 10 and even achieve higher sensitivity for materials with larger ε_r. The use of well-defined principle and higher order resonances results in well-understood relatively-uniform electric and magnetic field distributions. The compact nature of the microwave cavity that we use allows measurements to be made in a number of platforms, including the necktube of a liquid helium storage dewar (4-300 K) and PPMS (2-400 K, 0-9 T).

The dominant mechanism of loss in temperature-compensated microwave ceramics at cryogenic temperature was identified as resonant spin excitations of unpaired transition metal d-electrons in isolated atoms (light doping) or exchange coupled clusters (moderate to high doping).. We hope that this work will motivate additional theoretical efforts to model the exchange and dipole interactions in such transition-metal doped compounds in order to gain an

improved microscopic understanding of the relation between electron spin excitations and microwave loss.

Characterization of the electrical, chemical, optical and microwave properties have been made in order to explain the correlation between microwave loss and imperfections in a series of materials with a wide range of Q factors.

The intrinsic mechanism of loss tangent is strongly correlated to the phonon anharmonicity which is due to their unique electronic structure of lattice. In order to map the band structure of the material, angular resolved photoemission spectroscopy (ARPES) or other advanced spectroscopic techniques need to be performed. For this, we need to grow single crystal form of material. $Ba(Cd_{1/3}Ta_{2/3})O_3$ (BCT) dielectric thin films were grown on MgO (100) single crystal substrates by PLD. The use of enhanced oxygen pressures (53 Pa), Cd-enriched targets (1 mol BCT: 1.5 mol CdO) and elevated substrate temperatures (635 °C) are needed to synthesize stoichiometric films with over 99% of the film growing epitallially [BCT (100) || MgO (100) and BCT (010) || MgO (010)]. We observed that the higher the Cd enrichment in the target, the higher the substrate temperature at which stoichiometric films could be made and the better the epitaxy. The refractive index of BCT was measured to be 2.1 in the visible range. The dielectric constant of the BCT thin film is 32 at room temperature and low frequency. BCT has a bandgap of ~4.9 eV, as determined by optical absorption methods. Temperature-dependent electrical measurements have determined a room temperature conductivity of 3×10^{-12} $\Omega^{-1}cm^{-1}$ with a thermal activation energy of ~0.7 eV. The mean particle size is ~100 nm and root mean square

(RMS) surface roughness is ~ 5 to 6 nm according to atomic force microscopy (AFM) measurements. The excellent structural, optical and electrical properties of the BCT thin films make this system a promising candidate for use in a number of microelectronic and microwave communication applications.

There are a few topics in this area of study that should be pursued in the future. Firstly, in this study, the dominant loss mechanism at cryogenic temperatures has been identified.

The next step will be to determine what causes this loss at room temperature. Our group's and many others have found that the presence of defects in these materials correlate to the loss tangent. Our studies found that high loss BZT samples show higher electrical conductivity at high temperature and higher optical absorption background. The next step is to pinpoint which defects exist in these samples and what effect they have on the dielectric properties.

Secondly, in order to systematically study the effect of defects on the dielectric loss tangent, we need to introduce them controllably into the samples. We have used both neutron irradiation and reducing gas annealing. After the damage, we can study their dielectric, structural, optical and electrical properties and look for the correlation between the nature and concentration of defects and loss tangent.

Thirdly, we hope to use our advances in preparing epitaxial dielectric thin films to experimentally map out the electronic band structure and electron bonding using ARPES. These results can then be directly compared to density functional band structure calculations. This will allow us to improve our

understanding of fundamental physical properties, like d electron bonding, of these high performance materials. It will also help us to identify the intrinsic loss mechanism in these crystals. To overcome issues of charging in such experiments, the very thin films of less than 5 nm can be grown on a conductive buffer layer, such as YBCO, or substrate. Ideally, the substrate or buffer layer should be lattice matching with the material under investigation, otherwise the epitaxial quality of the thin films can be degraded. Coplanar structures also could be designed and fabricated to measure the loss tangent of thin films at microwave range.

Last but not least, we anticipate that high performance and compact planar RF devices could be produced with these microwave dielectric thin films. This will reduce the device size compared to conventional techniques which use bulk ceramic materials. These materials have a much lower loss than any other material.

REFERENCES

1. I. M. Reaney, D. Iddles, J. Am. Ceram. Soc., **89** (2006) 2063-2072

2. S.J. Liu, Ph.D Dissertation, Arizona State University, 2005

3. D. Kajfez and P. Guillon, Dielectric Resonators, (SciTech Publishing, Raleigh, NC, 1998).

4. I. M. Reaney, D. Iddles, J. Am. Ceram. Soc., **89** (2006) 2063-2072

5. T. Negas, in: H. Ling (Ed.), Ceramic Transactions: Materials and Processes for Wireless Communication, Vol. 53, American Ceramic Society Publications, Westerville, OH, 1995

6. T. Negas, G. Yeager, S. Bell, and R. Amren, Chemistry of Electronic Ceramic Materials, Proceedings of the International Conference, Jackson, WY, July 17-20, 1990 (National Institute of Standards and Technology Special Publications, Gaithersburg, MD, 804, 1991), p. 21

7. S.J. Liu, R. Taylor, N.S. Petrovic, L. Budd, M. Van Schilfgaarde, and N. Newman, J. Appl. Phys. **97** (2005) 014105-1 to 014105-8

8. H.X. Liu, S.J. Liu, V.Y. Zenou, C. Beach, and N. Newman, Jpn. J. Appl. Phys. **45** (2006) 9140-9142

9. G. Rong, N. Newman, B. Shaw, and D. Cronin, J. Mater. Res. **14** (1999) 4011-4019

10. F. Galasso and J. Pyle, Inorg. Chem. **2** (1963) 482-484

11. C.B. Eom, A.F. Marshall, S.S. Laderman, R.D. Jacowitz, and T.H. Geballe, Science **249** (1990) 1549-1552

12. Z.Z. Tang, S.J. Liu, R.K. Singh, S. Bandyopadhyay, I. Sus, T. Kotani, M. Van Schilfgaarde, and N. Newman N, Acta Mater. **57** (2009) 432-440

13. I. Qazi, I.M. Reaney, W.E. Lee, J. Eur. Ceram. Soc. **21** (2001) 2613-2616

14. D. Pamu D, P.D. Raju, A.K. Bhatnagar, Solid State Commun. **149** (2009) 1932-1935

15. J. Y. Tsao, Materials Fundamentals of Molecular Beam Epitaxy, Academic Press, New York NY, 1993

16. N. Newman, Vacuum & Coating Technology, **March 2012**, p.44

17. N. Newman, J. Cryst. Growth, **178** (1997) 102-112

18. INCHEM, Chemical Safety Information from Intergovernmental Organizations, ICSC:0117

19. CRC handbook of Chemistry and physics, 86 th edition, CRC press, Taylor & Francis

20. A.L. Patterson, Phys. Rev. **56** (1939) 978–982

21. J. Tauc, Mater. Res. Bull. **3** (1968) 37-46

22. A.M. Goodman, Appl. Optics. **17** (1978) 2779-2787

23. R. Swanpoel, J. Phys. E: Sci. Instrum. **16** (1983) 1214

24. N.M. Ravindra, P. Ganapathy, and J. Choi, Infrared. Phys. Techn. **50** (2007) 21-29

25. K Iijima, T. Terashima, K. Yamamoto, K. Hirata, and Y. Bando, Appl. Phys. Lett. **56** (1990) 527-529

26. B.S. Kwak, K. Zhang, E.P. Boyd, A. Erbil, and B.J. Wilkens, J. Appl. Phys. **69** (1991) 767-772

27. G.W. Farnell, I.A. Cermak, P. Silvester, and S.K. Wong, IEEE T Son. Ultrason. **SU-17** (1970) 188

28. D. Dimos, M.V. Raymond, R.W. Schwartz, H.N. Al-Shareef, and C.H. Mueller, J. Electroceram. **1** (1997) 145-153

29. S. Gevorgian, E. Carlsson, S. Rudner, L.D. Wernlund, X. Wang, U. Helmersson, IEE Proc.-Microw. Antennas Propag. **143** (1996) 397

30. R.C. Taber, Rev. Sci. Instrum. **61**, 2200 (1990)

31. R.C. Taber, J. N. Hollenhorst, L.S. Cutler, T.L. Bagwell, N. Newman and B.F. Cole, IEEE T. Ultrason. Ferr. **39**, 398 (1992).

32. N. Newman, K. Char, S.M. Garrison, R.W. Barton, and R.C. Taber et al., Appl. Phys. Lett. **57**, 520 1990

33. B.F. Cole, G.C. Liang, N. Newman, K. Char, G. Zaharchuk et al., Appl. Phys. Lett, **61**, 1727 (1992)

34. B.H. Moeckly, K.E. Kihlstrom, A.T. Findikoglu, and D.E. Oates, IEEE T. Appl. Supercond., **15**, 3308 (2005).

35. F. Gao, M.V. Klein, J. Kruse, and M. Feng, IEEE T. Microw. Theory, **44**, 944 (1996); F. Gao, Z. Zhou, M. Feng, M. Scharen, A. Cardona, and R. Forse, Appl. Phys. Lett., vol. 67, p.2229 , 1995.

36. D. Kajfez and P. Guillon, Dielectric Resonators, (SciTech Publishing, Raleigh, NC, 1998).

37. D. Kajfez and E.J. Hwan, IEEE T. Microw. Theory, **32**, 666 (1984)

38. L.F. Chen, C.K. Ong, C.P. Neo, and V.V. Varadan, Microwave Electronics: Measurement and Materials Characterization, (John Wiley & Sons Ltd, The Atrium, Southern Gate, Chichester, West Sussex, England, 2004).

39. M.T. Sebastian, Dielectric Materials for Wireless Communication, (Elsevier Ltd, 2008)

40. L. Liu, M. Flores, and N. Newman, "Microwave loss in the high performance dielectric $Ba(Zn_{1/3}Ta_{2/3})O_3$ at 4.2K", Phys. Rev. Lett. (to be published).

41. D. Kajfez, Q factor measurements using Matlab, (Artech House, Norwood, MA, 2011).

42. F. Abbas, L.E. Davis, and J.C. Gallop, Supercond. Sci. Technol., **7**, 495 (1994).

43. A. Abragam and B. Bleaney, Electron Paramagnetic Resonance of Transition Ions (Oxford University Press, New York, 1970), pp.28, 200, 432, 447

44. M.T. Sebastian, Dielectric Materials for Wireless Communication (Elsevier, 2008)

45. D. Kajfez, Q Factor. Oxford, MS: Vector Fields, 1994

46. The reader is referred to the last few decades of the modern solid-state literature including Physical Review B, Condensed Matter Physics, Advances in Physics, Journal of Physics: Condensed Matter, Physical Review Letters and Physics Today.

47. N.W. Ashcroft, and N.D. Merman, Solid State Physics (Holt, Rinehart, and Winston, Philadelphia, PA, 1976) pp. 2-27, 416-450, 626 and references therein.

48. R.R. Rakhimov, E.M. Jackson, D.E. Jones, and G.B. Loutts, J. Appl. Phys. **95**, 5653-5660 (2004).

49. V.B. Braginsky, V.P. Mitrofanov, and V.I. Panov, *Systems with Small Dissipation* (University of Chicago Press, Chicago, IL, 1985).

50. H. Tamura, D.A. Sagala, and K. Wakino, Jpn. J. Appl. Phys. **25**, 787-791 (1986).

51. H. Tamura, Am. Ceram. Soc. Bull. **73**, 92-95 (1994).

52. K. Wakino, M. Murata, and H. Tamura, J. Am. Ceram. Soc. **69**, 34-38 (1986).

53. V.L. Gurevich, and A.K. Tagantsev, Adv. Phys., **40**, 719-767 (1991).

54. K.R. Subbaswamy, and D.L. Mills, Phys. Rev. B. **33,** 4213-4220 (1986).

55. M. von Schickfus, and S. Hunklinger, J. Phys. C: Solid State Phys. **9**, L439 – L442 (1976)

56. D.P. Pappas, M.R. Vissers, D.S. Wisbey, J.S. Kline, and J. Gao, IEEE Trans. Appl. Supercond. **21**, 871-874 (2011).

57. B. Bleaney, and J.E. Ingram, Proc. R. Soc. Lond. A. **208**, 143-158 (1953).

58. A. Abragam, and B. Bleaney, *Electron Paramagnetic Resonance of Transition Ions* (Oxford University Press, New York, 1970), p. 514-518.

59. P.K. Davies, J. Tong, and T. Negas, J. Am. Ceram. Soc. **80**, 1727-1740 (1997)

60. J.M. Martinis, K.B. Cooper, R. McDermott, M. Steffen, M. Ansmann, K.D. Osborn, K. Cicak, S. Oh, D.P. Pappas, R.W. Simmonds, and C.C. Yu, Phys. Rev. Lett. **95**, 210503 (2005).

61. M.P. Weides, J.S. Kline, M.R. Vissers, M.O. Sandberg, and D.S. Wisbey, et al. Appl. Phys. Lett. **99**, 262502 (2011).

62. J. Konopka, I. Wolff, and S.J. Lewandowksi, J. Appl. Phys. **72**, 218-223 (1992).

63. M.R. Varma, and N.D. Kataria, J. Mater. Sci: Mater. Electron. **18**, 441-446 (2007).

64. H. Tamaura, H. Matsumoto, and K. Wakino, Jpn. J. Appl. Phys. **28**, Suppl. **28–2**, 21–23 (1989).

65. J. Kanopka, and I. Wolff, IEEE Trans. Microw. Theory Tech. **40**, 2418-2423 (1992).

66. J. Krurpka, R.G. Geyer, M. Kuhn, and J.H. Hinken, IEEE Trans. Microw. Theory Tech. **42**, 1886-1890 (1994)

67. S. Liu, R. Taylor, N.S. Petrovic, L. Budd, M. Van Schilfgaarde, and N. Newman, J. Appl. Phys. **97**, 014105 (2005).

68. R.C. Taber, Rev. Sci. Instrum. **61**, 2200-2206 (1990).

69. S. Stoll, and A. Schweiger, J. Magn. Reson. **178**, 42-55 (2006).

70. M. Flores, R. Isaacson, E. Abresch, R. Calvo, W. Lubitz, and G. Feher, Biophys. J., **92**, 671-682 (2007).

71. F.J. Rosenbaum, Rev. Sci. Instrum. **35**, 1550-1554 (1964).

72. W.M. Walsh, and L.R. Rupp, Rev. Sci. Instrum. **57**, 2278-2279 (1986).

73. B. Kirste, in *Handbook of Electron Spin Resonance. Data Sources, Computer Technology, Relaxation, and ENDOR* (eds Poole, C.P., Farach, H.A.) (American Institute of Physics Press, New York, 1994) Chapter 2, p. 33.

74. J. Krzystek, A. Ozarowski, and J. Telser, *Coord. Chem. Rev.* **250**, 2308-2324 (2006).

75. F. Gesmundo, and P.F. Rossi, J. Solid State Chem. **8**, 287-296 (1973).

76. I.M. Reaney, D. Iddles, J. Am. Ceram. Soc. **89**, 2063-2072 (2006).

77. P.K. Davies, J. Tong, and T. Negas, J. Am. Ceram. Soc. **80**, 1727-1740 (1997).

78. D.W. Kim, K.H. Ko, and K.S. Hong, J. Am. Ceram. Soc. **84**, 1286-1290 (2001).

79. M.R. Varma, R. Raghunandan, and M.T. Sebastian, Jpn. J. Appl. Phys. **44**, 298-303 (2005).

80. P. RiaziKhoei, F. Azough, and R. Freer, J. Am. Ceram. Soc. **89**, 216-223 (2006).

81. N.W. Ashcroft, and N.D. Merman, Solid State Physics (Holt, Rinehart, and Winston, Philadelphia, PA, 1976) pp. 2-27, 416-450, 626 and references therein.

82. R.R. Rakhimov, E.M. Jackson, D.E. Jones, and G.B. Loutts, J. Appl. Phys. **95**, 5653-5660 (2004).

83. H. Tamura, D.A. Sagala, and K. Wakino, Jpn. J. Appl. Phys. **25**, 787-791 (1986).

84. H. Tamura, Am. Ceram. Soc. Bull. **73**, 92-95 (1994).

85. K. Wakino, M. Murata, and H. Tamura, J. Am. Ceram. Soc. **69**, 34-38 (1986)

86. V.L. Gurevich, and A.K. Tagantsev, Adv. Phys. **40**, 719-767 (1991)

87. K.R. Subbaswamy, and D.L. Mills, Phys. Rev. B. **33**, 4213-4220 (1986)

88. H. Tamura, J. Eur. Ceram. Soc. **26**, 1775-1780 (2006)

89. J.D. Breeze, J.M. Perkins, D.W. McComb, and N. McN. Alford, J. Am. Ceram. Soc. **92**, 671-674 (2009)

90. S.J. Penn, N. McN. Alford, A. Templeton, X. Wang, M. Xu, M. Reece, and K. Schrapel, J. Am. Ceram. Soc. **80**, 1885-1888 (1997)

91. V.B. Braginsky, V.P. Mitrofanov, and V.I. Panov, Systems with Small Dissipation (University of Chicago Press, Chicago, IL, 1985)

92. J. Konopka, I. Wolff, and S.J. Lewandowksi, J. Appl. Phys. **72**, 218-223 (1992).

93. M.R. Varma, and N.D. Kataria, J. Mater. Sci: Mater. Electron. **18**, 441-446 (2007).

94. H. Tamaura, H. Matsumoto, and K. Wakino, Jpn. J. Appl. Phys. Suppl. **28–2**, 21–23 (1989).

95. J. Kanopka, and I. Wolff, IEEE Trans. Microw. Theory Tech. **40**, 2418-2423 (1992)

96. J. Krurpka, R.G. Geyer, M. Kuhn, and J.H. Hinken, IEEE Trans. Microw. Theory Tech. **42**, 1886-1890 (1994)

97. N Klein, M. Schuster, S. Vitusevich, M. Winter, and H.R. Yi, J. Eur. Ceram. Soc. **21**, 2687–2691 (2001)

98. J.M. Martinis, K.B. Cooper, R. McDermott, M. Steffen, M. Ansmann, K.D. Osborn, K. Cicak, S. Oh, D.P. Pappas, R.W. Simmonds, and C.C. Yu, Phys. Rev. Lett. **95**, 210503 (2005).

99. M.P. Weides, J.S. Kline, M.R. Vissers, M.O. Sandberg, and D.S. Wisbey, et al. Appl. Phys. Lett. **99**, 262502 (2011).

100. S. Kawashima, M. Nishida, I. Ueda, and H. Ouchi, J. Am. Ceram. Soc. **66**, 421-423 (1983)

101. L. Liu, C. Garg, A. Matusevich, M. Qader, R.M. Hanley and N. Newman, "Resonance techniques to accurately measure the loss tangent and EPR spectrum of small dielectric samples", submitted to Rev. Sci. Instrum. 2012

102. D. Kajfez, Q factor measurements using Matlab, (Artech House, Norwood, MA, 2011).

103. S. Stoll, and A. Schweiger, J. Magn. Reson. **178**, 42-55 (2006).

104. L. Liu, M. Flores and N. Newman, "Microwave loss in the high performance dielectric $Ba(Zn_{1/3}Ta_{2/3})O_3$ at 4.2K", submitted to Phys. Rev. Lett. 2012

105. F.J. Rosenbaum, Rev. Sci. Instrum. **35**, 1550-1554 (1964).

106. W.M. Walsh, and L.R. Rupp, Rev. Sci. Instrum. **57**, 2278-2279 (1986).

107. F. Gesmundo, and P.F. Rossi, J. Solid State Chem. **8**, 287-296 (1973).

108. A. Abragam, and B. Bleaney, Electron Paramagnetic Resonance of Transition Ions (Oxford University Press, New York, 1970), p. 514-518.

109. M. Che, G. Djéga-Mariadassou, K. Dyrek and Z. Olech, Zeitschrift für Physikalische Chemie, **152**, 131-138 (1987).

APPENDIX A

SUPPLEMENTAL MATERIALS FOR EPR SIMULATION IN BZT SYSTEM AROUND 4K

A.1 EPR Simulation of Ni doped BZT

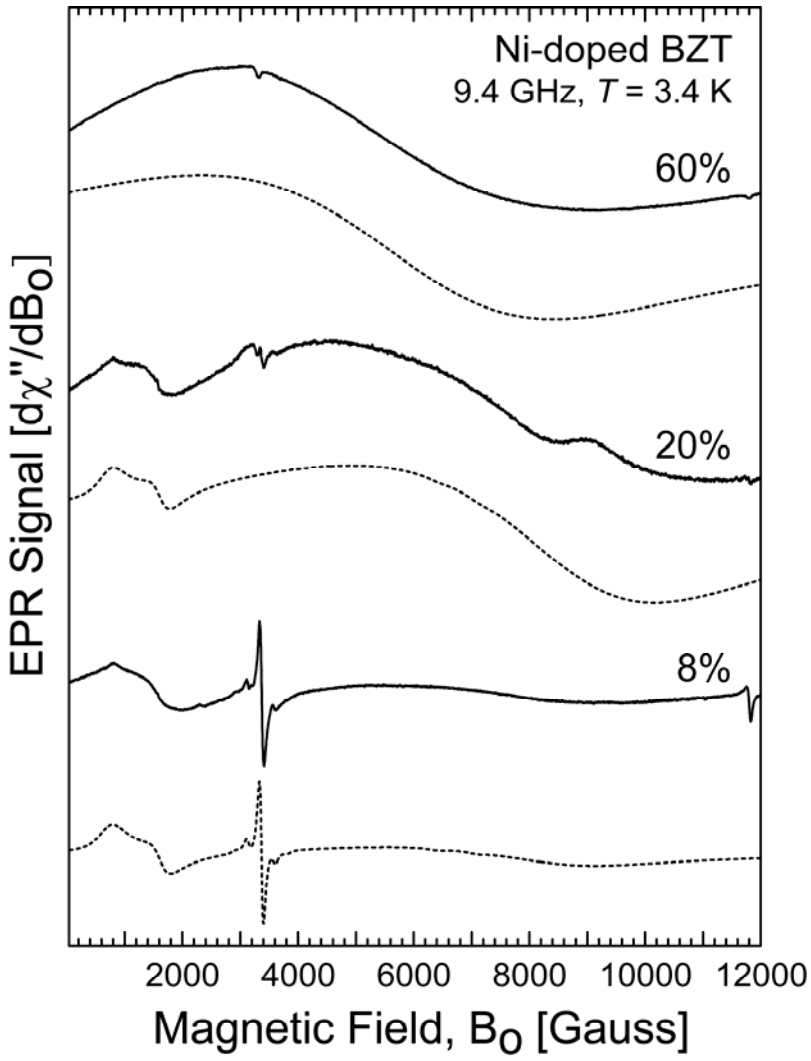

Figure A.1 Experimental (solid line) and simulated (dotted line) CW powder EPR spectra of the 8%, 20% and 60% Ni doped BZT samples at 3.4 K. The models used for the simulations are described in the Experimental methods section. The parameters obtained from the fits are shown in Table A.1.

Table A.1. Parameters used in the fittings of the CW EPR spectra of the 8%, 20% and 60% Ni-doped BZT samples. Two different Ni^{2+} paramagnetic species were observed.

Parameters[a]	8% Ni		20% Ni		60% Ni
	Species 1[b] (S = 1)	Species 2[c] (S = 1)	Species 1[b] (S = 1)	Species 2[c] (S = 1)	Species 2[c] (S = 2)
g_x	1.95	2.20	1.95	2.20	2.20
g_y	2.39	2.20	2.39	2.20	2.20
g_z	2.16	2.20	2.16	2.20	2.20
B (mT)	27	260	27	400	540
D (GHz)	12.5	64.9	12.5	71.0	114
E/D	1/3	0	1/3	0	0

[a] The fitting parameters were the following: the three g values, g_x, g_y, and g_z, the line width, B, and the zero-field splitting parameters, D and E.

[b] The electronic structure of this species does not change with the increase of Ni^{2+} concentration. However, it is not present in all spectra.

[c] The electronic structure of this species changes with the increase of Ni^{2+} concentration.

A.2 EPR Simulation of commercial microwave dielectric materials

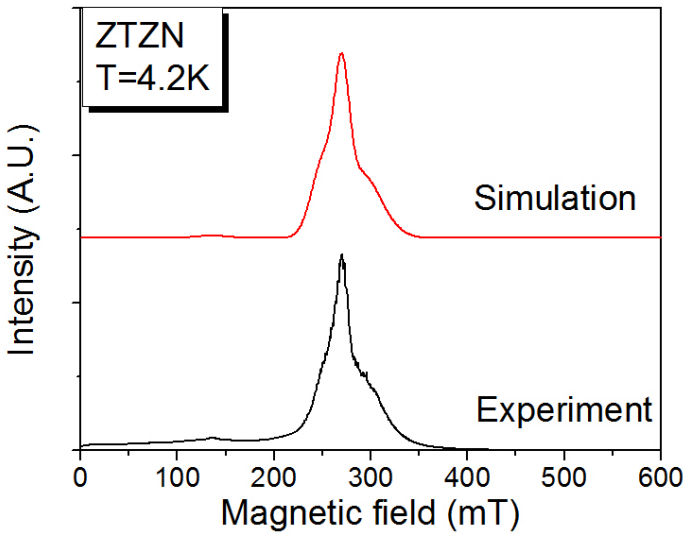

Figure A.2. Experimental magnetic dependence of microwave loss (black) and simulated (red) CW powder EPR spectra of the commercial $ZrTiO_4$-$ZnNb_2O_6$ (ZTZN) at 4.2 K. The parameters obtained from the fits are shown in Table A.2.

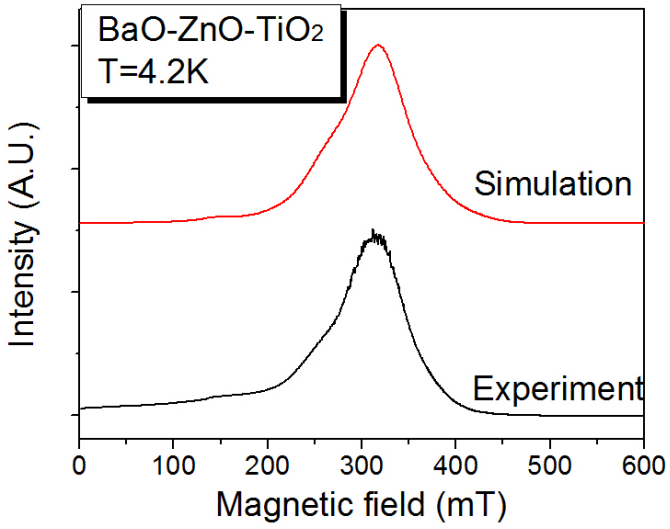

Figure A.3. Experimental magnetic dependence of microwave loss (black) and simulated (red) CW powder EPR spectra of the commercial $BaTi_4O_9$-$BaZn_2Ti_4O_{11}$ at 4.2 K. The parameters obtained from the fits are shown in Table A.2.

Table A.2. Parameters used in the simulation of the commercial $ZrTiO_4$-$ZnNb_2O_6$ and $BaTi_4O_9$-$BaZn_2Ti_4O_{11}$ samples.

Parameters[a]	$ZrTiO_4$-$ZnNb_2O_6$				$BaTi_4O_9$-$BaZn_2Ti_4O_{11}$	
	Species 1 (S = 1/2)	Species 1 (S = 3/2)	Species 1 (S = 3/2)	Species 2 (S = 3/2)	Species 1 (S = 3/2)	Species 2 (S = 3/2)
g	2.14	2.00	2.30	4.28	2.00	4.30
ΔB (mT)	17	50	30	40	50	40
D (GHz)	0	0	0	0	1.6	0
Weight	1	0.35	0.2	0.005	1	0.002

[a] The fitting parameters were the following: the g values, the line width, ΔB, the zero-field splitting parameters, D, and the relative weight ratio of each specie in the multi-component system.

APPENDIX B

MICROWAVE LOSS MEASUREMENT INSTRUMENTS AND OPERATION PROCEDURES

B.1 Equipment list

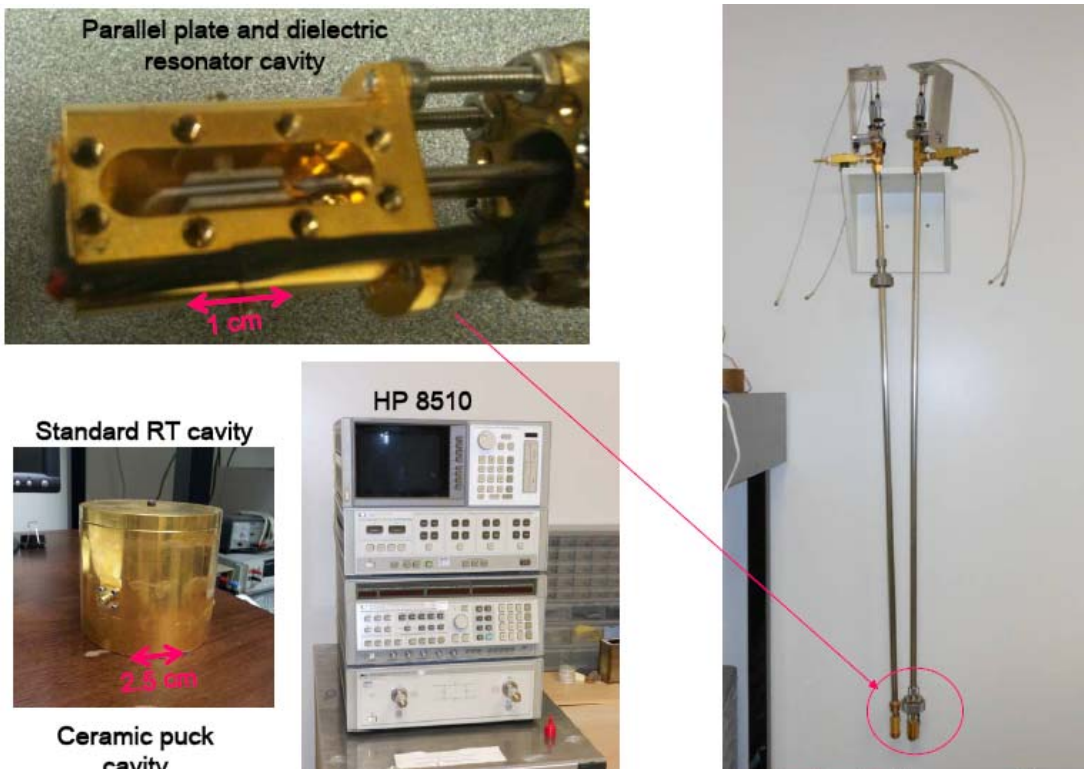

Figure B.1 Microwave measurement equipments

Figure B.2 Cryogenic systems: Necktube liquid helium dewar (left) and PPMS system (right)

B.2 Sample loading procedures

1. Parallel plate resonator (PPR) measurement (A thin dielectric spacer between two superconducting films, and then put into a small gold plated copper cavity)

- ✧ Load the ceramics thin chip and superconductor films on the small aluminum square sample holder and align them to make a “sandwich” structure. The thin film surface should be inside to touch with the dielectric interlayer spacer.

Figure B.3 loading the dielectric and superconducting films using the Aluminum square sample holder

- ✧ Remove the top plates on the copper cavity, replace it with the L-shaped gold plated sample aligner. Using screws to tighten it.
- ✧ Using the tweezers to put the "sandwich" between the G-10 fiber glass clamps and on top of the L-shaped aligner. Then adjust its position to be well located in the center of the cavity.
- ✧ Tighten screws on the side walls of the cavity using a small Allen wrench to fasten the "sandwich" structure.

Figure B.4 loading the sample between fiber glass clamps and on top of the L-

shaped aligner (left) and tighten the screws on the side walls (right)

- ✧ Remove the L-shaped aligner and replace it with the top cover. Make sure the sample is fastened and will not drop.
- ✧ Play with the micrometers on the other side of the dipping probe to change the distance between the coupling loop and the sample. The coax probe should barely touch the sample. Record the readings on the micrometers.
- ✧ Put the other top cover on and tighten the screws.

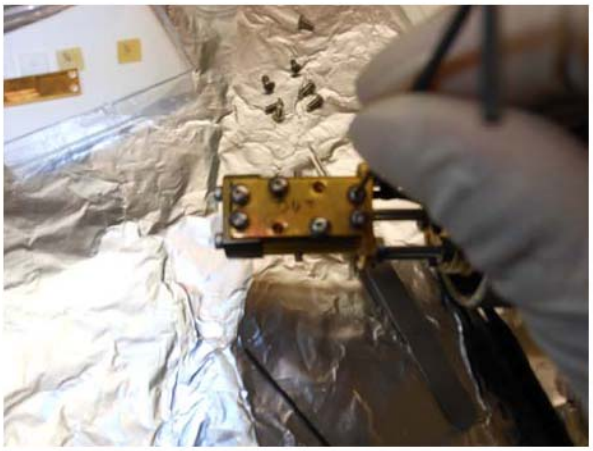

Figure B.5 putting on the top plates and tighten the screws

- ✧ Put on the copper protection cap outside of the cavity.

2. Dielectric resonator (DR) measurement

- ✧ Every is the same with the PPR sample loading, but one should notice that the sample should be wrapped using clean Teflon tape onto one Teflon clamp because the large thermal expansion coefficient of the Teflon with leads to dropping of the samples when cooling down.

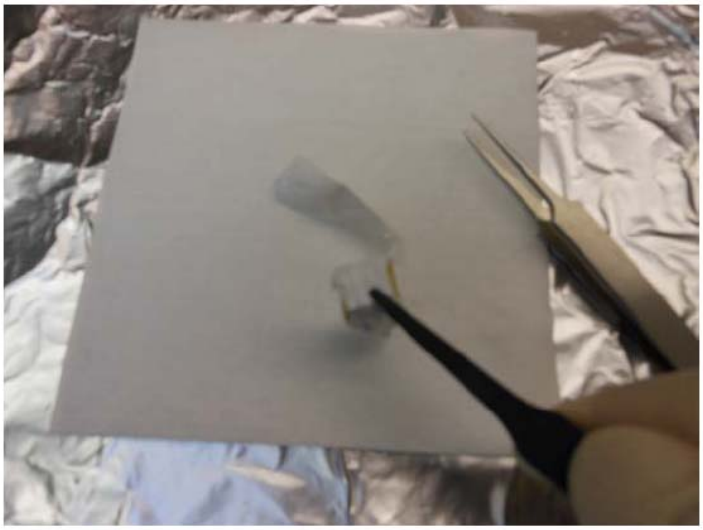

Figure B.6 Wrap the dielectric resonator sample with Teflon tape onto one Teflon clam